MODELING AN ANODE LAYER HALL THRUSTER AND ITS PLUME

by

Yongjun Choi

A dissertation submitted in partial fulfillment
of the requirements for the degree of
Doctor of Philosophy
(Aerospace Engineering)
in The University of Michigan
2008

Doctoral Committee:

Professor Iain D. Boyd, Chair
Professor Alec D. Gallimore
Professor Brian E. Gilchrist
Assistant Professor Michael Keidar, George Washington University

To my sister Jinsuk

ACKNOWLEDGEMENTS

There are so many of people to thank. First of all, I would like to thank my advisor, Professor Iain D. Boyd, for his valuable guidance, advice, and generous support and constant encouragement throughout these years. For his balanced efforts, I am a far more complete scientist than I ever expected. I'd also like to thank Michael Keidar, for his continued support in my research.

My special thanks go to Dr. Chunpei Cai for his help and collaboration throughout this research. I also appreciate the help from Dr. John Yim for providing the hydrodynamic code and helping me around tricky issues with plasma modeling.

I would like also to thank all of my friends - Rick Kamminga , Chad Creighton, Jia Liu, Jiwon Mok, Jaehun Sim, Woosuk Ji, Youngchang Cho, Chang-kwon Kang, Eunji Jun, Minkwan Kim, Insung Kim, Taeyoung Lee and Heejun Choi. Thanks for making my stay at the University of Michigan a memorable and enjoyable one, and for much help.

My sincere appreciation goes to my other friends, research group members, both past and present, for their intellectual and social contributions.

I owe special thanks to my sister Jinsuk for her support for me throughout my time in graduate school.

I am greatly indebted to my wife MinHye. You have always been there for me from the very beginning, and I can't even begin to express how much your love and support have meant to me. Thank you.

TABLE OF CONTENTS

LIST OF FIGURES

LIST OF TABLES

LIST OF APPENDICES

CHAPTER 1

INTRODUCTION

1.1 Objective

Electric propulsion (EP) devices are propulsion systems that primarily use electric power to produce thrust, as opposed to chemical, or nuclear power. EP is currently more commonly relegated to secondary propulsion duties requiring lower thrust such as satellite station-keeping and orbit raising, but it is increasingly being considered as a viable means of primary propulsion, especially for travel within the solar system where its specific impulse range is optimal. For example, the SMART-1 probe, developed by the European Space Agency, utilized a Hall thruster as its primary propulsion source to travel to and enter orbit around the Earth's moon. EP devices, first seriously studied in the 1950s, have a 40 year operational history in the Soviet/Russian space program and are presently entering use in Western space programs [1] [2].

Hall thrusters are an efficient form of EP devices. Early work on the Hall thruster yielded more efficient and more powerful Hall thrusters. However, almost all this early work was based on experiments and was costly in terms of time and money [3]. Fortunately, progress in computer technology during the last decades has enabled the development of sophisticated computational models of Hall thrusters at a lower cost.

A variety of different approaches and numerical schemes for computational modeling of Hall thrusters has been developed in the last ten years. Of these various models, hybrid modeling, i.e. the use of a particle approach to simulate heavy particles and a

fluid model to simulate the electrons, provides physical accuracy and computational efficiency [1] [3].

Plume impingement is a major concern regarding the integration of Hall thrusters onto spacecraft. The exhausted plume may have interaction with spacecraft surfaces. The plasma plume may impinge on external surfaces. This impingement occurs due to either high-energy ions with a relatively large divergence angle as they exit the thruster or from back-flowing charge-exchange ions. Sputtered material from internal or external surfaces may also become deposited on other spacecraft components. Either case would reduce the effectiveness or even completely impair the use of solar panels, scientific instrumentation, and other sensitive devices. Though EP can offer specific impulses that are orders of magnitude higher than chemical rockets, the associated thrust is often orders of magnitude lower. Figure 1.1 shows various propulsion methods and their range of specific impulse and thrust. With a lower thrust, EP devices need to operate for a long period of time to achieve the necessary velocity of the mission. Therefore, the accumulated impingement effect onto a spacecraft may become significant, and eventually result in the failure of devices or even the failure of an entire mission.

Therefore, modeling of the plume fields of Hall thrusters yields important information. It provides understanding of the plume impingement that involves fluxes of high-energy ions and charge-exchanged particles onto sensitive spacecraft devices such as solar cell arrays. Moreover, plume modeling helps to clarify the complex plasma processes inside the thruster with the aim of improving propulsion performance. The near field plume of a Hall thruster is a very important region because its relatively high plasma density facilitates the use of a variety of experimental diagnostic techniques. Such diagnostics are much more difficult to apply either in the internal thruster flow or in the plume far field. Therefore, understanding the behavior of the thruster plume is critical to the design of thrusters and spacecraft.

In the Hall thruster, the magnetic field in the acceleration channel provides closed azimuthal electron drift and enhances the impact ionization of the propellant. Experimental measurements of the near-field plasma plume from Hall thrusters show that the magnetic field leaks into the plume and is strong enough to affect the electron motion in the near-field plume region [4] [5]. However, very few researchers considered magnetic field effects on the plasma plume.

Therefore, the goal of the work presented in this thesis is to analyze the possible influence of the magnetic field on the plasma plume and improve the understanding of the plasma plume through the development of computational modeling.

The following sections present the rocket equation, a brief introduction to electric propulsion, an overview of types of Hall thrusters, a review of existing computational modeling approaches, and an outline of the main body of the dissertation.

1.2 The Rocket Equation

Electric propulsion and chemical spacecraft propulsion are based on Newton's Third Law as follows:

$$m\frac{dV}{dt} = \dot{m}U_e, \tag{1.1}$$

where the left hand side of Eqn. (1.1) represents the spacecraft acceleration and the right hand side represents the propellant thrust. Replacing $\dot{m}$ by $-\frac{dm}{dt}$ and integrating Eqn. (1.1) provides the classical rocket equation

$$\frac{m_f}{m_i} = e^{-\frac{\Delta V}{U_e}}, \tag{1.2}$$

where the left hand side is the final non-propellant mass fraction of the spacecraft and ΔV represents the mission velocity requirement. The rocket equation describes the relationship between the mission velocity requirement, the amount of propellant mass required to achieve this velocity, and the performance of the propulsion system which is characterized by the propellant exit velocity U_e. In particular, for a given mission

velocity requirement, the higher the propellant exit velocity, the less propellant mass is required.

Specific impulse, I_{sp} is a way to describe the efficiency of rocket and jet engines. It represents the ratio of the thrust (the force produced by the rocket) to the propellant weight flow rate,

$$I_{sp} = \frac{U_e}{\dot{m} g_o}, \tag{1.3}$$

where g_o is the sea-level gravitational acceleration, 9.81 m/sec^2. From this definition, it is clear that I_{sp} is a direct measure of the propellant exit velocity of a given spacecraft propulsion system.

1.3 Historical Background of Electric Propulsion

The idea of electric propulsion can be traced back to Robert Goddard [6]. He noticed an important fact that in several of his experiments, a high exhaust velocity was achieved with a still cool tube. He pointed out that electrostatic propulsion does not have a limitation of speed by the specific heat of combustion in several papers in the 1920s [7]. The principles of electric propulsion also go back to the concepts developed by the German/Austrian physicist Hermann Oberth which were published in his famous 1929 work "Wege zur Raumschiffahrt" (Ways to Spaceflight). A whole chapter was devoted to power and electric propulsion. There he explained his thoughts on the mass savings of electric propulsion, predicted its use in spacecraft propulsion and attitude control, and advocated electrostatic acceleration of charged gases.

While Oberth and Goddard recognized the potential payoff electric propulsion could have to interplanetary flight, it was Wernher von Braun who sanctioned the first serious study on EP. In 1947, at Fort Bliss, von Braun assigned a young engineer named Ernst Stuhlinger the task of giving Professor Oberth's early concepts of electric spacecraft propulsion "some further study". Fifteen years later, Stuhlinger published a book entitled *Ion Propulsion for Space Flight* and directed NASA Marshall Space

Flight Center's work on arcjet and ion propulsion systems.

One drawback cited by people who had doubts about EP was the low inherent thrust-to-weight ratios of electric engines. EP systems are expected to have thrust-to-weight values thousands of times smaller than chemical propulsion systems. In 1953, H.S. Tsien [8] designed trajectories and thrust alignment procedures for low-thrust, EP-propelled spacecraft. In his work, it was shown that thrust-to-weight ratios as low as 1×10^{-5} are sufficient to change the trajectory of a space vehicle over a realistic period of time.

With the beginning of the "Space Race" in the late 1950's between the U.S.S.R and the U.S.A, experimental work on EP began to flourish. In the United States, RocketDyne (1958), NACA Lewis Flight Laboratory (1959, now NASA Glenn Research Center), and Princeton University (1961) began their EP experimental programs.

In the early 1990's, the advent of new, high-power spacecraft architectures made EP more attractive to mission planners. At the same time, there was an influx of Russian Hall thruster technology to the west and an aggressive new technology push at NASA began to advocate the use of ion engines in interplanetary probes.

As of today, EP devices are widely used as primary interplanetary propulsion and for on-obit applications such as station keeping, attitude control and orbit transfer [9].

1.4 Types of Electric Propulsion

EP devices can be categorized into three principal types: electrothermal, electrostatic, and electromagnetic [10]. These divisions are based on the mechanism through which electric power is utilized to accelerate the exhaust flow.

1. Electrothermal EP devices use electrical current or electromagnetic radiation to heat the propellant. The resulting thermal energy is converted to directed kinetic energy by expansion through a nozzle. Resistojets, arcjets and cyclotron resonance thrusters are examples of electrothermal devices.

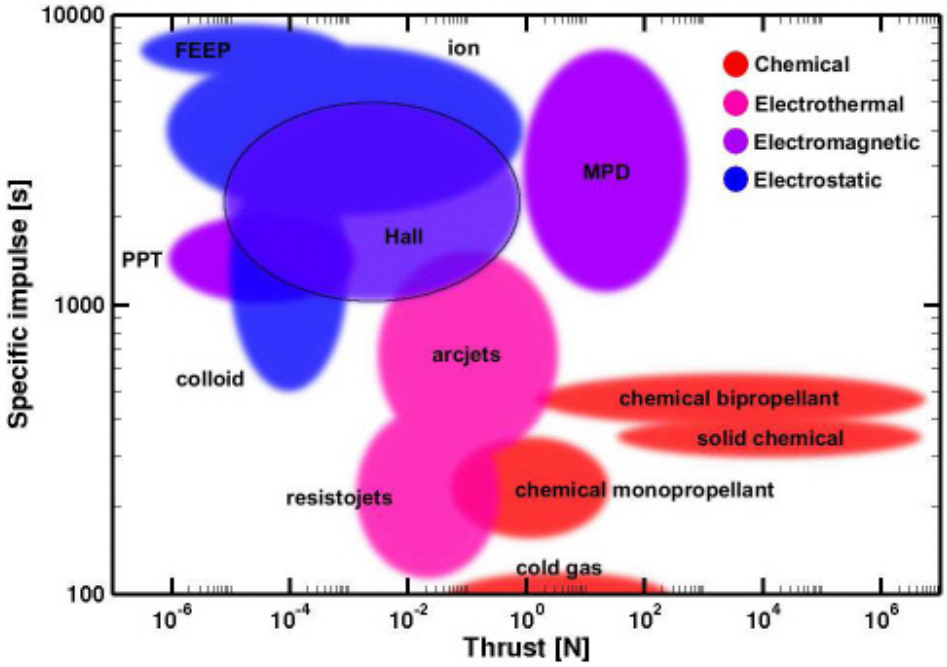

Figure 1.1: Thrust and specific impulse ranges for various forms of propulsion

2. Electrostatic EP devices accelerate charge-carrying propellant particles in a static electric field. These devices typically use a static magnetic field that is strong enough to magnetize the electrons while sufficiently weak to not magnetize the ions. Ion engines and Hall thrusters are examples of electrostatic thrusters.

3. Electromagnetic devices accelerate charge-carrying propellant particles in interacting electric and magnetic fields. The magnetic field strength in these devices is typically high enough to significantly affect both ion and electron trajectories. Examples include pulsed plasma thrusters (PPT), Magnetohydrodynamic (MPD) thrusters, Hall thrusters and traveling-wave accelerators.

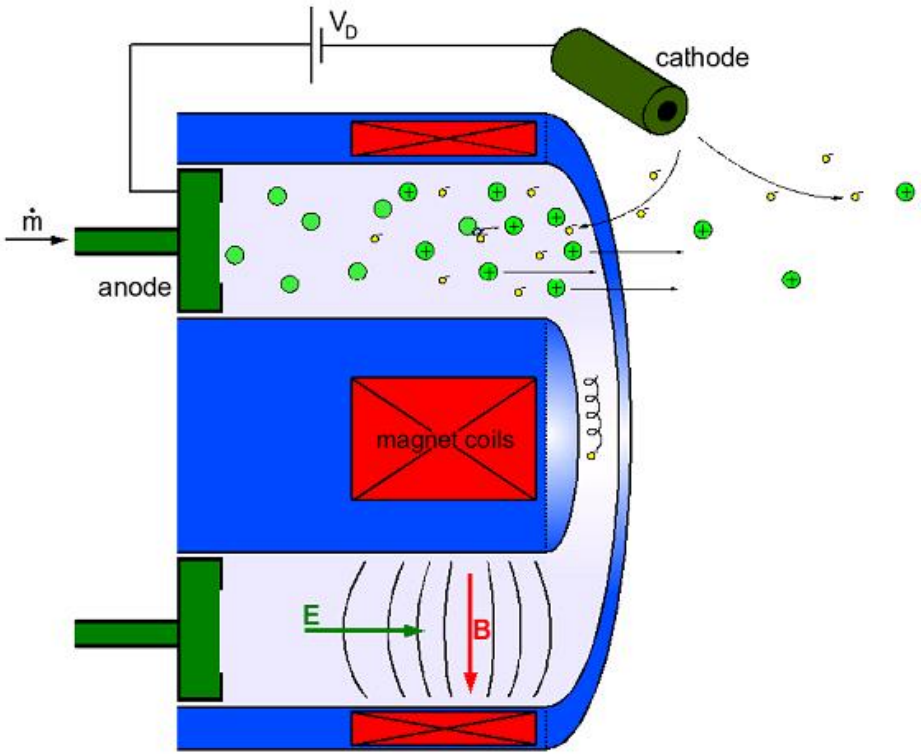

Figure 1.2: A schematic of a Hall thruster

1.5 Hall Thrusters

Hall thrusters, classified as either electrostatic or electromagnetic thrusters, originated in the 1950s and 1960s in both the United States and the former USSR. During the 1970s and 1980s, the US lost interest in Hall thrusters, but Russia continued to advance the development of these devices. After the first operational use of a Hall thruster in space by the USSR, over 100 thrusters have been flown on satellites [11]. A basic schematic of a Hall thruster is shown in Fig. 1.2. Typically, the acceleration channel has an annular shape. At the end of the channel is the anode through which the neutral propellant is injected. Usually xenon is used for the propellant because of its high molecular weight and low ionization potential. Outside of the channel, a cathode is located. The cathode emits electrons, a portion of which neutralizes the ion flow, and the rest travels upstream towards the anode. In the thruster channel, a magnetic field traps the electrons and impedes their axial drift. The magnetic

field circuit is designed to provide a relatively strong (a few hundred gauss) radial magnetic field near the exit of the acceleration channel. The electrons are caught in the magnetic fields and move azimuthally. This azimuthal movement of electrons forms a Hall current, from which the thruster obtains its name. Most of the ionization of the neutral propellant occurs in this high Hall current region of the channel. The ions are accelerated by the axial electric field. One of the characteristics of a Hall thruster is that the magnetic field is strong enough to magnetize the electrons while sufficiently weak to not magnetize the ions.

Due to this characteristic of Hall thrusters, analyzing the possible influence of the magnetic field on the plasma plume is an important part of studying plumes.

1.6 Hall Thruster Types

There are two types of Hall thrusters, the stationary plasma thruster (SPT) and the thruster with anode layer (TAL) [12]. In the SPT, the walls of the acceleration channel are made of insulating material, such as boron nitride or silicon carbide. Since the dielectric walls are not conductive, charge builds up along the length of the acceleration channel walls. The acceleration channel is relatively long (a few centimeters). Figure 1.3 shows an example of an SPT type thruster, the SPT-100.

A TAL is similar in construction, but the walls of the acceleration channel are made of metallic materials such as stainless steel or molybdenum. Since the walls are conductive, a constant potential is observed along the entire wall. High electron temperatures ($>$ 20 eV) are typically observed in TAL thrusters. In the TAL, the length of the acceleration channel is smaller (a few millimeters). Figure 1.4 shows an example of a TAL type thruster, the D55. This is the thruster investigated in this thesis.

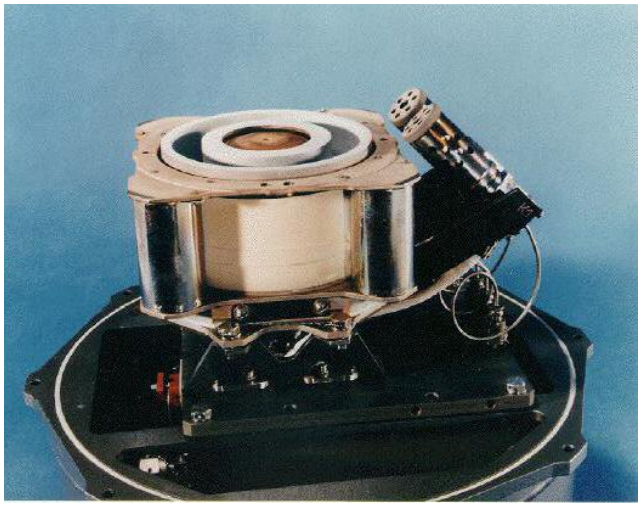

Figure 1.3: SPT-100 Hall thruster (Courtesy of Plasmadynamics and Electric Propulsion Laboratory (PEPL) at the University of Michigan)

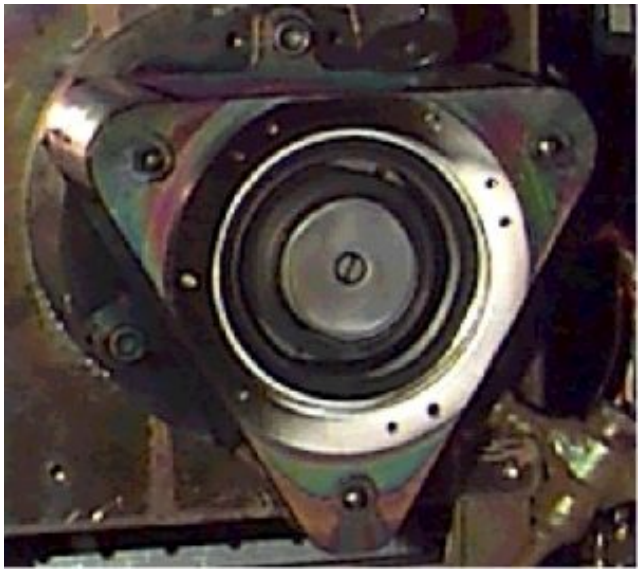

Figure 1.4: D55 Hall thruster (Courtesy of PEPL)

1.7 Computational Modeling of Hall Thrusters

Computational modeling of Hall thrusters offers possibilities for improving thruster-spacecraft integration and operation testing with relatively low cost. In addition, simulation enables the effects of facility backpressure to be investigated in a very isolated fashion, thus avoiding one of the primary pitfalls (finite facility backpressure) of vacuum chamber based thruster testing. This role is even more crucial with the development of new, high power Hall thrusters which operate at very high mass flow rates that can swamp the ability of the vacuum pumps to maintain sufficiently high vacuum in test chambers. Finally, computational modeling can be developed to track wall-erosion characteristics of thrusters in order to verify thruster lifetime limitations from the erosion of the dielectric walls. As a research tool, computational simulation offers the ability to isolate physical effects such as channel wall materials and anode pre-sheath formation, resulting in a clearer understanding of the physics of these devices. Eventually, when Hall thruster physics are better understood, these computational codes will also become useful design tools for future generations of Hall thrusters.

There are three kinds of computational modeling of Hall thrusters - (1) fluid, (2) kinetic, and (3) hybrid models.

1. *Fluid modeling* of Hall thrusters considers both electrons and heavy species (ions and neutral atoms) to be fluids. This approach is very fast (measured in minutes) and can be adapted to both 1-D and 2-D axisymmetric geometries and to both steady state and time-dependent solvers.

2. *Kinetic (particle-based) modeling* of Hall thrusters uses particles to simulate both electrons and heavy species. Since the electrons are several orders of magnitude lighter than the ions, they move on a much smaller timescale. This requirement forces the use of timesteps which are about 500 times smaller than

timesteps consistent with ion dynamics alone. Kinetic models give physically correct results but computational expense is very high, with typical simulations lasting from days to weeks.

3. *Hybrid modeling* offers a compromise between fluid modeling and kinetic modeling. By considering heavy species as particles and electrons as a fluid, hybrid codes can capture non-Maxwellian features for the heavy species without incurring the severe timestep penalty associated with fluid electron modeling.

1.7.1 Modeling of Hall thruster channels

Several one-dimensional Hall thruster models have been successfully developed to explore fundamental properties of Hall thrusters. For example, Fruchtman et al. [13] used a fully fluid description to investigate the idea of controlling the electric field within the acceleration channel using absorbing electrodes. Ahedo et al. [14] employed a three-fluid description (electrons, ions, neutrals) to investigate the effects of electron pressure and back-flow of ions to the anode.

A variety of two-dimensional Hall thruster models has also been developed. A two-dimensional, steady, multi-fluid formulation with a detailed wall presheath treatment has been developed for Hall thrusters by Keider et al. [15]. Fife and and Martínez-Sánchez [16] used a self-consistent PIC model for ions and a fluid model for electrons. A similar two-dimensional model was reported by Koo and Boyd [3].

A fully kinetic 2-D code for a Hall thruster channel plasma is developed by Szabo [17].

1.7.2 Modeling of Hall thruster plumes

The plasma plume of Hall thrusters is a rarefied gas. Therefore, fluid approaches are rarely used for the plasma plume simulations. Keidar and Boyd [18] used a quasi-one-dimensional plasma hydrodynamic model to investigate a magnetic field effect on

the plasma plume.

A variety of hybrid thruster models has been developed. Boyd and Yim [19] developed a detailed electron fluid model with the PIC technique for heavy species. This model is expanded to 3D by Cai [1]. Roy et al. [20] employed the hybrid method to ion thruster plumes. Taccogna et al. [21] developed a hybrid model without assuming quasi-neutrality. Cheng et al. [22] reported 3D hybrid model results.

As of now, there is no full kinetic model which simulates Hall thrusters' far-field plumes, because the required number of particles and timesteps are too large to use this method. However, this is clearly the direction for future research, as computer power continues to increase.

1.8 Thesis Outline

The main topic of this thesis is the development of electron fluid models for analyzing and predicting the effects on the plume of magnetic field leakage from a Hall thruster channel. Chapter 2 reviews the background of rarefied gas and simulation methods, including two specific particle simulation techniques that are used in the plasma plume simulations. Chapter 3 discusses a hydrodynamic model which describes the plasma flow and ion flux in the thruster channel. The hydrodynamic model is used to calculate the exit boundary conditions for the plasma plume simulations. Chapter 4 presents the application of the hydrodynamic simulation to analyze the discharge voltage-current characteristics of the D55 Hall thruster, thruster channel plasma simulations in the D55 Hall thruster, and estimation of the boundary conditions at the nozzle exit of the D55 Hall thruster. Chapter 5 discusses 2D axisymmetric hybrid simulations of plasma plume flows from a D55 Hall thruster. Chapter 5 also presents a comparison of the Boltzmann electron model and the detailed electron model. This work is the only known application of a hybrid plasma plume model with consideration of the magnetic field. For all of these studies, the computational results are compared to

available experimental data. Chapter 6 summarizes these findings and ends with recommendations for future work.

CHAPTER 2

REVIEW OF NUMERICAL METHODS

This study uses the hybrid model for heavy particles and electrons to simulate two-dimensional axisymmetric plasma plume flows from a D55 TAL thruster. For heavy particles, the hybrid model uses two methods: the direct simulation Monte Carlo (DSMC) and Particle-In-Cell(PIC) methods. For electrons, the hybrid model uses fluid models. Plasma plumes are rarefied gases; therefore this chapter defines a rarefied gas, describes the methodology for the simulations, and explains the algorithms and code developed or adapted for the simulations.

2.1 Rarefied Gases

A gas flow can be modeled at either the macroscopic or microscopic level. The macroscopic model regards the gas as a continuous medium and provides information on the flow properties such as the velocity, density, pressure, and temperature. The Navier-Stokes equations offer the conventional mathematical model of a gas as a continuum. The microscopic or molecular model recognizes the gas as a myriad of discrete particles with inner structure, and provides information on the position, velocity, and state of every particle. The mathematical model at this level is the Boltzmann equation.

In this thesis, we use the molecular model to analyze the plasma properties of ions in plumes. Therefore, it is important to describe the circumstances under which the continuum model loses its validity and must be replaced by the molecular model.

The macroscopic properties can be identified with average values of the molecular quantities. These properties can be defined as long as there are a sufficient number of molecules within the smallest significant volume of a flow. Generally, this condition is satisfied and the results from the molecular model can be expressed in terms of the familiar continuum flow properties.

However, the transport terms in the Navier-Stokes equations of continuum gas dynamics fail when a gas is rarefied. In a rarefied gas, the gradients of the macroscopic variables become so steep that the scale length is of the same order as the average distance traveled by the molecules between collisions, or the *mean free path*.

The degree of rarefaction of a gas is generally expressed through the *Knudsen number*

$$K_n = \lambda / L, \tag{2.1}$$

where λ is the mean free path of the gas, defined as the average distance traveled by gas particles between successive collisions, and L is the characteristic dimension. The traditional requirement for the Navier-Stokes equations to be valid is that the *Knudsen number* should be less than 0.01. The error in the Navier-Stokes results is significant in the regions of the flow where the *Knudsen number* exceeds 0.01. When $0.01 < K_n < 1$, the gas flow is rarefied. If $K_n > 1$, the gas flow is free molecular. In a free molecular gas flow, intermolecular effects are insignificant because essentially no collisions occur.

Particle methods, a subtype of kinetic simulation methods, are used to study rarefied gas flows, such as plasma plume flows. The Molecular Dynamics (MD) method, the DSMC method, and the PIC method are examples of particle methods, a subtype of kinetic simulation methods.

2.2 The Molecular Dynamics Method

The MD method is a form of computer simulation that allows atoms and molecules to interact for a period of time under known laws of physics. This method provides a detailed view of the motion of the atoms. Because molecular systems generally consist of a vast number of particles, it is impossible to find the properties of such complex systems analytically; MD simulation circumvents this problem by using numerical methods. The MD method was proposed by Alder and Wainwright in the late 1950s [23] [24] to study the interactions of hard spheres. This method is considered to be the first particle method ever developed. It is related to the DSMC method. A detailed introduction to this method is provided by Haile [25].

An MD simulation involves simultaneous tracking of a large number of simulated molecules within a region of simulated physical space. A potential energy function is generally used to determine the force on a molecule due to the presence of other molecules. This potential energy function is modeled with two-body or many-body potentials or by empirical means. The time evolution of a set of interacting molecules is followed by integrating Newton's classical equations of motion. Macroscopic flow properties are obtained by averaging the molecule information over a space volume. This space volume should be larger than the mean molecular spacing and much smaller than the characteristic dimensions.

The major disadvantage of the MD method is that it is highly inefficient for most practical applications. There are two reasons for this: 1) a large number of molecules must be simulated, and 2) the computation of an element of trajectory for any molecule requires consideration of all other molecules as potential collision partners. The numerical cost therefore scales as N^2 where N is the number of particles. Therefore, molecular dynamics is limited to flows where the continuum and statistical approaches are inadequate.

2.3 The Direct Simulation Monte Carlo Method

The most commonly used particle method for simulating a rarefied gas flow is the DSMC method [26]. This method was first introduced by Bird in the 1960s [27] and has been developed further to be reliable and accurate, and, therefore, has gained wide acceptance in the scientific community. Each particle in the DSMC simulation represents a large number of real molecules. This makes the DSMC method much more efficient than the molecular dynamics simulation. The DSMC method has been widely described in the literature [28] [29], [30], [31], [32]. One of its most successful results was the accurate prediction of the inner structure for normal shock waves [1].

The DSMC method emulates the nonlinear Boltzmann equation by simulating the real molecule collisions with collision frequencies and scattering velocity distributions determined from the kinetic theory of a rarefied gas. With a sufficiently large number of simulated particles, Bird [33] has shown that the Boltzmann equation can be derived through the DSMC procedures.

2.3.1 Algorithm of the DSMC Method

In the DSMC method, the computational domain is divided into a network of cells, where each cell serves as a separate region for molecular interaction and as a space element for sampling flow information. To calculate the movement of particles and the interaction between particles, the DSMC method employs a time step that is smaller than the mean collision time of gas molecules. The method describes the state of the system through the positions and velocities of particles. After an initial setup of cells is completed, the following computational tasks are performed within each time step:

1. Select collision pairs: Particle pairs are randomly selected to collide. Random selection is governed by kinetic theory to replicate the actual collision frequency.

2. Perform binary collisions; redistribute all types of energies and chemical reactions: Momentum and energy are conserved in the collision process.

3. Inject new particles at inlet boundaries: The number of particles is decided based on kinetic theory.

4. Move particles and compute interactions with other boundaries: The particles are first allowed to translate at constant velocities and they do not interact with each other. This means that they are moved according to their own trajectories, and their positions are updated deterministically. Some particles may travel from cell to cell: Some particles may escape from the computational domain or hit a solid wall and bounce back.

5. Sample flow properties.

For a steady rarefied flow simulation, the above steps are repeated until a prescribed time is reached.

2.3.2 Collisions

To evaluate the collisions in a DSMC simulation, pairs of particles in a cell are randomly selected, regardless of their relative positions and velocities. In Bird's "No Time Counter" (NTC) scheme [26], a total number of

$$\frac{1}{2}n\bar{N}(\sigma g)_{\max}\Delta t$$

pairs are sampled from the cell at each time step, and a collision actually takes place if a candidate pair satisfies

$$(\sigma g)/(\sigma g)_{max} > R$$

where R is a random number uniformly distributed in $[0, 1]$. The average number of particles in a cell is denoted by $\bar{N}$. For each cell, the parameter $(\sigma g)_{\max}$ is stored.

This parameter $(\sigma g)_{\max}$ is set to an initial appropriate value and is automatically updated if a larger value is encountered during the simulation.

All DSMC simulations described in this thesis use the NTC scheme.

2.3.3 Variable Hard Sphere Model

After a collision, conservation of momentum and energy provide four out of the six equations required to determine the post-collision velocities. The remaining two conditions are found using the assumption of isotropic scattering.

In determining the collision frequency of a gas molecule, the use of the typical inverse power law potential model is inadequate because the model gives an infinite total cross-section. To overcome this difficulty, Bird [34] introduced the Variable Hard Sphere (VHS) model as a practical approximation to the inverse power law potential model. In the VHS model, isotropic scattering is also assumed and its total cross-section σ is allowed to vary with the relative speed of the two colliding molecules g as follows

$$\sigma/\sigma_r = g^{1-2\omega}/\overline{g_r^{1-2\omega}}. \tag{2.2}$$

Here, g_r is the relative collision speed at the reference temperature T_r. In Equation (2.2), σ_r is the reference cross section and is written as $\sigma_r = \pi d_{\text{ref}}^2$, where d_{ref} denotes the reference molecular diameter. For several major species, data for ω and d_{ref} at $T_r = 273$ K can be found in [26].

The VHS model is used throughout this thesis for all flow simulations involving neutral atom-atom collisions.

2.3.4 Boundary Conditions

The velocity distribution for simulated particles reflecting from a solid wall varies with the type of wall they hit. Specular and diffuse walls are the two most common types considered in DSMC. When a particle collides with a specular wall, its component of

velocity tangential to the wall remains the same, and the component normal to the wall changes its sign. When a particle bounces back from a diffuse wall at temperature T_w, its velocity components tangential to the wall are sampled from the standard Maxwellian distribution

$$f(c_t)\,dc_t = \frac{1}{\sqrt{2\pi RT_w}} \exp\left(\frac{-c_t^2}{2RT_w}\right) dc_t, \tag{2.3}$$

while its normal component is sampled from the biased-Maxwellian distribution

$$f(c_n)\,dc_n = \frac{1}{RT_w} c_n \exp\left(\frac{-c_n^2}{2RT_w}\right) dc_n. \tag{2.4}$$

A wall with accommodation coefficient ν assumes that a fraction ν of all the particles colliding with the wall are thermalized by the wall and the remaining fraction $(1-\nu)$ of the particles are specularly reflected by the wall. In this thesis, a full accommodation coefficient $\nu = 1$ is used in all simulations.

The internal energy of a reflecting particle can be handled in the same manner. However, for atomic xenon, which is exclusively used in all simulations in the thesis, no internal energy is considered.

2.3.5 Limitations of DSMC

Two principal limitations of the DSMC method are: the assumption of molecular chaos and the requirement of a dilute gas. The molecular chaos assumption means that particles undergoing a collision will not meet again until they having collided with other particles many times. The velocities of a collision pair are, therefore, totally uncorrelated. The dilute gas assumption excludes the DSMC method from being used for dense gases or for highly ionized plasmas that are dominated by long-range interactions and many-body interactions [26].

Another assumption for DSMC is that particle motion and particle collisions can be decoupled. This assumption requires that the simulation time-step Δt should

be smaller than the local mean collision time τ. The cell size should be small in comparison with the local mean free path. Therefore, the ratio of mean collisional separation to the local mean free path should be much smaller than unity.

For these reasons, all particle methods, including the DSMC method, are quite expensive compared with continuum Computational Fluid Dynamics(CFD) methods.

2.4 The Particle In Cell Method

The PIC method is a kinetic particle method that tracks the motion of collections of charged particles. The PIC method is well developed, and a detailed description can be found in Birdsall and Langdon [35]. This method has been applied to inertial confined fusion plasmas, electron and ion guns, microwave devices, and plasma propulsion [1]. Work by Roy [20] [36] and VanGilder [37] employed the PIC method to model ion thruster plumes. Similar to the DSMC method, the PIC method moves particles which represent neutral atoms, ions and electrons through space.

The basic idea behind the PIC method of plasma simulation is extremely simple: It closely follows the intuitive picture of a plasma. The plasma is a collection of charged particles which interact with each other and with external fields. The fields obey Maxwell's equations and the particles follow trajectories determined by Newton's 2^{nd} Law with the force given by the Lorentz equation.

The electromagnetic fields in the simulation are not continuous in space or in time. This is a consequence of the discretization of the spatial dimensions of the system. The physical volume is divided into cells by lines. The intersections of these lines define a set of points called mesh points or grid points.

Each mesh point specifies a location to which the fields and charge densities are assigned after solving the discretized field equations and the discretized equation of motion; the cell itself specifies a volume through the boundaries of which the current densities are calculated. That is why this method is referred to as the Particle-in-

Cell Method. The particles, whose coordinates are continuous, may occupy positions anywhere within the mesh. The forces acting on them are calculated in terms of the fields at the neighboring mesh points. The particles move through the mesh in finite time steps. During a time step, the fields are kept constant, and at the end of the step, the discretized field equations are solved again to update the field distribution.

In plasma simulations, the cell size, time scale, and number of particles per cell must be carefully chosen to represent the essence of the plasma physics. To properly update the particles' properties according to the physics, the time scale must correspond to the inverse of the plasma frequency

$$\omega_p = \sqrt{\frac{ne^2}{\epsilon_0 m}} \tag{2.5}$$

If inter-particle effects are significant in the plasma flow, the cell size should be the order of or less than the Deybe length, which is the shielding distance around a test charge and the scale length inside which inter-particle effects are most significant

$$\lambda_d = \sqrt{\omega_p} v_{th} \tag{2.6}$$

Generally, in quasi-neutral plasmas where collective behavior is more significant, larger cells can be used.

2.4.1 Major Steps in the PIC Method for Plasma Plume Simulations

For particle simulations of plasma plume flow, which consist of neutral atoms, ions and electrons, heavy neutral atoms and ion particles are simulated with the DSMC and the PIC methods. The electrons are modeled as a fluid because the electron collision frequency is almost a hundred times higher than the ion collision frequency for the usual thruster plasma plume conditions. In that case, we can assume that the electrons adjust themselves more quickly, so a fluid approximation is appropriate.

The major difference in the PIC method from the DSMC method is, due to the

presence of the electric field, accelerations on charged particles must be considered. Hence, there are a few extra steps in the PIC method:

1. Calculate electric potential field ϕ, and magnetic field if it is included. Usually the process needs to obtain the charge density distribution, which requires a process to allocate ion particle charges onto the mesh.

2. Calculate the electric field from $\overrightarrow{E} = - \bigtriangledown \phi$.

3. Determine the ion acceleration in a cell from the coordinates of the ion particle according to the electric field on the nodes.

4. Accelerate ion particles over a small time step Δt.

5. Perform collisions. Besides Momentum Exchange (MEX) between neutral particles, there are two other groups of collisions that must be considered in plasma plume flows: MEX between a neutral particle and an ion particle, and Charge Exchange (CEX) between a neutral particle and an ion particle. The latter type of collision happens when an ion particle passes a neutral atom. With an electron transferred from a slow neutral atom to a fast ion, a CEX collision will result in a fast neutral atom and a slow ion.

A complete list of steps for the DSMC-PIC methods can be found in Chapter 5 for particle simulations of plasma plume flows from a D55 TAL thruster.

2.5 Electron Fluid Models

In the hybrid model, electrons are assumed as a fluid because electrons adjust their velocities more quickly since the electrons are several orders of magnitude lighter than the ions, they move on a much smaller timescale. Two types of fluid models are used in this thesis: the *Boltzmann model* and the *Detailed model*. This section discusses these two models.

2.5.1 Boltzmann Model

In the first PIC step to compute the plasma potential, the most widely used and the simplest electron fluid model is the *Boltzmann model*, which is obtained from the electron momentum equation:

$$\phi = \phi_{ref} + \frac{kT_{ref}}{e} \log\left(\frac{n_e}{n_{ref}}\right) \tag{2.7}$$

This equation is derived from the electron momentum equation using several strong assumptions. These assumptions include that the fluid electron flow is isothermal, collisionless, the electron pressure obeys the ideal gas law and the magnetic field is neglected. However, in plasma plumes, especially in the near field, there are significant gradients in the electron number density and electron velocity, therefore the approximation may be inappropriate. Moreover, experimental measurements of the near-field plasma plume from Hall thrusters show that the magnetic field leaks into the plume and is strong enough to affect the electron motion in the near-field plume region [4] [5]. In chapter 5, we will show that this neglect of the magnetic field leakage gives incorrect results with the *Boltzmann model*.

2.5.2 The Detailed Model

Recently, a detailed electron fluid model was proposed [19]. This model represents a significantly increased level of physics compared to the *Boltzmann model*. In the *Detailed model*, the electron continuity equation is transformed into a Poisson equation by assuming steady flow and introducing a stream function;

$$\nabla^2\psi = n_e n_a C_i \tag{2.8}$$

where $n_e\overrightarrow{v_e} = \nabla\psi$ and the ionization rate coefficient C_i is expressed as a function of electron temperature using a simple relation proposed by Ahedo et al. [14]:

$$C_i = \sigma_i c_e \left(1 + \frac{T_e \epsilon_i}{(T_e + \epsilon_e)^2}\right) \exp\left(-\frac{\epsilon_i}{T_e}\right) \tag{2.9}$$

In the presence of a magnetic field, assuming a steady state, and neglecting the inertial term, the electron momentum equation is written [38]

$$0 = -en_e(\overrightarrow{E} + \overrightarrow{V_e} \times \overrightarrow{B}) - \nabla p_e + n_e \nu_e m_e(\overrightarrow{V_e} - \overrightarrow{V_i}) \tag{2.10}$$

Experimental investigation of the magnetic field distribution near a Hall thruster shows that the magnetic field has both radial and axial components of which the radial component is much larger [4]. Thus, the axial component of the magnetic field can be ignored. In this case, the plasma plume flow is across the magnetic field and the radial component of the magnetic field B varies along the axis. With another assumption that electrons behave as an ideal gas, Eq. (2.10) can be written in component form as:

$$0 = -en_e(E_z - V_{e\phi}B_r) - kT\frac{dn_e}{dz} - n_e\nu_e m_e(V_{ez} - V_{iz}) \tag{2.11}$$

$$0 = -en_e V_{ez} B_r - n_e \nu_e m_e(V_{e\phi} - V_{i\phi}) \tag{2.12}$$

From Eq. (2.12) the azimuthal component of electron velocity can be expressed as

$$V_{e\phi} = -\frac{e}{m_e\nu_e} + V_{i\phi} \simeq -\frac{e}{m_e\nu_e} V_{ez} B_r \tag{2.13}$$

However, $V_{e\phi}$ from Eq. (2.12) is derived for the case where the density is high enough to produce a significant collision rate. If the density is low, then collisions are very rare, and $V_{e\phi}$ becomes just a drift velocity, $V_{drift} = E_z/B_r$. Here we use a combination of these two limiting results:

$$V_{e\phi} = (1 - w)V_{drift} + w\left(-\frac{e}{m_e\nu_e V_{ez} B_r}\right) \tag{2.14}$$

where the weight function is $w = (\frac{n}{n_{max}})$ and n_{max} is a local maximum which is chosen as the neutral particle density at the thruster exit.

By introducing the plasma potential $\nabla\phi = -\overrightarrow{E}$, a generalized Ohm's law is obtained

$$\overrightarrow{j} = \sigma[-\nabla\phi + \overrightarrow{V_e} \times \overrightarrow{B} + \frac{1}{en_e}\nabla(n_e k T_e)] \tag{2.15}$$

For given n_e, $\overrightarrow{v_e}$, T_e, the charge continuity condition

$$\nabla \cdot \overrightarrow{j} = 0 \tag{2.16}$$

is then solved to obtain the plasma potential.

From Eq. (2.16), a generalized Poisson's equation describing the electron potential is obtained

$$\begin{aligned} \nabla \cdot (\sigma\nabla\phi) = \; & \tfrac{k}{e}(\sigma\nabla^2 T_e + \sigma T_e \nabla^2(\ln(n_e)) + \sigma\nabla(\ln n_e)\cdot\nabla T_e \\ & + T_e\nabla\sigma\cdot\nabla(\ln(n_e)) + \nabla\sigma\cdot\nabla T_e) \\ & - \tfrac{\partial\sigma}{\partial z}V_\phi B_r - \sigma(V_\phi\tfrac{\partial B_r}{\partial z} + B_r\tfrac{\partial V_\phi}{\partial z}) \end{aligned} \tag{2.17}$$

The electron temperature equation is obtained from the steady-state electron energy equation [39]

$$\begin{aligned} \nabla^2 T_e \; = & -\nabla\ln(\kappa_e)\cdot\nabla T_e + \tfrac{1}{\kappa_e}(-\overrightarrow{j}\cdot\overrightarrow{E} + \tfrac{3}{2}n_e(\overrightarrow{v_e}\cdot\nabla)kT_e + p_e\nabla\cdot\overrightarrow{v_e} \\ & + 3\tfrac{m_e}{m_i}\nu_e n_e k(T_e - T_h) + n_e n_a C_i \epsilon_i) \end{aligned} \tag{2.18}$$

The electron number density n_e is set equal to the ion number density n_i based on the plasma quasi-neutral assumption. The electron conductivity σ, the electron thermal conductivity κ_e, the ion-electron collision frequency ν_{ei}, and the neutral electron collision frequency ν_{en} can be found in [39] [40] and its references:

$$\sigma = \frac{e^2 n_e}{m_e \nu_e} \tag{2.19}$$

$$\kappa_e = \frac{2.4}{1 + \frac{\nu_{ei}}{\sqrt{2}\nu_e}}\frac{k^2 n_e T_e}{m_e \nu_e}\left(\frac{1}{\omega_c^2/\nu_e^2 + 1}\right) \tag{2.20}$$

where $\nu_e = \nu_{ei} + \nu_{en}$, ν_{ei} is the ion-electron collision frequency, ν_{en} is the neutral atom-electron collision frequency, and $\omega_c = eB/m_e$ is the cyclotron frequency. These frequencies are evaluated for the xenon system using cross sections provided in ref. [39]. Equation (2.20) shows that in the region of finite magnetic field in which $\omega_c \gg \nu$ the resulting thermal conductivity coefficient is very small. As the magnetic field vanishes κ_e becomes larger.

By treating the right hand side terms as known sources and solving Equations (2.8), (2.17), and (2.18), three fundamental electron properties are obtained, i.e., electron velocity, plasma potential, and electron temperature.

2.6 Simulation Methods and Numerical Implementation Issues

For particle simulations of plasma plume flow, heavy neutral atoms and ion particles are simulated with the DSMC [26] and the PIC [35] methods, while the electrons are modeled as a fluid. Therefore, this section discusses the simulation steps of the hybrid code, the finite element solver of the Poisson equations of the electron fluid model, derivative calculation on unstructured meshes, weight scheme, and collision dynamics.

2.6.1 General Steps for the DSMC-PIC Methods

For particle simulations of plasma plume flow, heavy neutral atoms and ion particles are simulated with the DSMC [26] and the PIC [35] methods, while the electrons are modeled as a fluid. The hybrid DSMC-PIC simulation can be summarized as follows:

1. (PIC): Allocate the charge of each ion inside a cell onto the cell nodes.

2. (Fluid): Calculate plasma potential ϕ using a fluid electron model.

3. (PIC): Calculate ionization in all cells. A fraction of neutral atoms will be

changed to ions:

$$\Delta n_i = C_i n_a n_i \Delta t \tag{2.21}$$

4. (PIC): Calculate the electric field on each node with the relation:

$$\overrightarrow{E} = - \bigtriangledown \phi \tag{2.22}$$

5. (DSMC, PIC): Sample quantities inside each cell.

6. (DSMC): Perform momentum exchange and CEX collisions inside each cell.

7. (DSMC, PIC): Introduce new particles (ions and neutral atoms) into the simulation domain from inlet boundaries.

8. (PIC): Calculate the ion acceleration based on the electric field at the nodes.

9. (DSMC, PIC): Advance all particles one time step based on the position, velocity, and acceleration.

When particles move across an outer boundary, they are removed from the simulation. When a neutral particle collides with a thruster wall, it rebounds back into the simulation domain with a thermal velocity characterized by the wall temperature. When an ion collides with a wall, it loses its charge and rebounds as a neutral atom.

2.6.2 General Finite Element Solver for Poisson Equations

Equations (2.8), (2.17), and (2.18) can be expressed as a general Poisson equation [41]

$$-\bigtriangledown(P(x,y,z) \cdot \bigtriangledown Q(x,y,z)) = S(x,y,z), \tag{2.23}$$

where $P(x,y,z)$ is a distribution of coefficients, $Q(x,y,z)$ is a distribution of the primary variable to be solved, and $S(x,y,z)$ is a known distribution of source terms.

For a two-dimensional or axisymmetric simulation on a structured mesh, an Alternative Direction Implicit(ADI) iterative solver [42] is usually adopted because the

ADI scheme is easy to implement [43] [44] [45]. However, there are several drawbacks to the ADI method [1]. First, the method is not applicable, or very difficult to implement on unstructured meshes. Second, if the ADI method is used for structured meshes with a certain geometry, it must be applied on each sub-domain separately and artificial inner boundaries must be created. Therefore, the simulation results may be inaccurate. This precludes the application of ADI to complex geometries, even with structured meshes.

However, to simulate flows in a complex geometry, an unstructured mesh must be adopted, which precludes using the ADI method. To solve the two problems mentioned above, Cai [1] developed a general purpose finite element solver that is applicable to two- and three-dimensional structured and unstructured meshes. Cai's solver can be used for structured and unstructured meshes, complex geometries, and can integrate the boundary conditions more naturally and accurately. For a more detailed discussion of the finite elementary solver, see Cai [1]. We use Cai's finite element solver to solve Equations (2.8), (2.17), and (2.18).

2.6.3 Derivative Calculation on an Unstructured Mesh

The calculation of derivatives is required on a node for each time step. Aside from being accurate, the optimal calculation scheme must also be applicable on both serial and parallel machines.

In this thesis, the least squares method [46] is adopted for finding derivatives such as calculating the electric field. The following example will illustrate the least squares method. To calculate the electric field from a potential field, we assume the unknown gradients on one node to be $\overrightarrow{E}(r,z) = (E_r, E_z)$. If N nodes with differences of plasma potential $d(\phi)_i$ and distance vectors dX_i connected to this node, then the N nodes form $N \times 2$ relations which are overdetermined

$$ME = d\phi, \tag{2.24}$$

where M is an $N \times 2$ matrix, E is a 2×1 vector, and $d\phi$ is an $N \times 1$ vector. By multiplying by a transposed matrix M^T on both sides, this overdetermined matrix is transformed to a 2×2 matrix and the equations can be solved.

Because the least squares method approach includes the effects from all nodes connected to a specific node, it yields accurate results. It is, however, necessary to gather a table of node connection relations at the start of each simulation and maintain it throughout the simulation. Gathering this table will create additional computational cost. The least squares method is also applicable on parallel machines.

2.6.4 Weighting Schemes

A weighting scheme is a crucial step for a successful DSMC-PIC simulation using the detailed fluid electron model. The ion number density at a specific node must be accurately estimated by weighting the charge of ions in all cells connected with this node. The acceleration for a particle must be interpolated from the electric field values on the same nodes. A correct ionization source term also requires a valid plasma density and a valid neutral density which are calculated from each particle's position for each cell node.

Two kinds of weighting schemes are used for charge allocation. The first category of weighting schemes is based on areas or volumes. In these methods, a particle's charge is allocated to cell nodes weighted by the areas or volumes formed by the particle's position in the cell nodes. The particle's position in a cell has an important influence on the weight of the charge that will be assigned on different cell nodes. Schemes of this category are expected to yield a higher accuracy and are widely used in PIC simulations. Ruyten [47], for example, presented a widely-used scheme for structured axisymmetric meshes (Figure 2.1). Ruyten calculated the weight of each node as follows

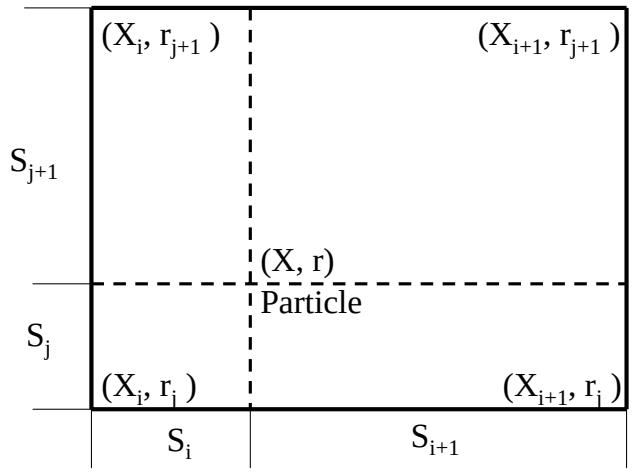

Figure 2.1: Particle positions and weighting factors in Ruyten's density conservation scheme

$$S_j = \frac{(r_{j+1} - r)(2r_{j+1} + 3r_j - r)}{2(r_{j+1}^2 - r_j^2)} \tag{2.25}$$

$$S_{j+1} = \frac{(r - r_j)(2r_{j+1} + 3r_j - r)}{2(r_{j+1}^2 - r_j^2)} \tag{2.26}$$

$$S_i = \frac{x_{i+1} - x}{x_{i+1} - x_i} \tag{2.27}$$

$$S_{i+1} = \frac{x - x_i}{x_{i+1} - x_i} \tag{2.28}$$

$$W(i, j) = S_i S_j \tag{2.29}$$

$$W(i, j+1) = S_i S_{j+1} \tag{2.30}$$

$$W(i+1, j) = S_{i+1} S_j \tag{2.31}$$

$$W(i+1, j+1) = S_{i+1} S_{j+1} \tag{2.32}$$

This scheme works accurately on cylindrical coordinates with structured rectangular cells by satisfying both charge and charge density conservation. However, this scheme is only applicable to structured meshes based on volumes and areas. Because of this

limitation to Ruyten's weighting scheme, we use another scheme. In this weighting scheme, the charge density on a specific node is calculated by summing up all particles' charges inside a closed area around the nodes, and then dividing by the area. This closed area can include all cells connected to these nodes, or, only a fraction of these cells. This scheme can be used for a DSMC-PIC simulation with unstructured meshes.

The cell average values are calculated and then these values are averaged onto the nodes in the current processor. If we assume that there are N cells connected to a node in one computer processor, and the jth cell has an average charge density n_j, then the charge density n on the node can be expressed as

$$n = \sum_{j=0}^{N} n_j / N \tag{2.33}$$

This scheme does not require a complete list of cell average values for all cells physically connected to a node, but only cells in the same computer processor. Therefore, the scheme is efficient on a parallel machine without significant loss of accuracy.

To effectively suppress statistical scatter in the charge density, this study further uses a relaxation in charge and neutral density on a node

$$n_{new} = 0.1 n_{alloc} + 0.9 n_{old}, \tag{2.34}$$

where n_{new} is the current charge or neutral number density, n_{alloc} is the density obtained from the above mentioned allocation scheme, and n_{old} is the charge or neutral number density used in the last time step. For steady flow simulations, this treatment is effective in reducing statistical scatter.

2.6.5 Collision Dynamics

The DSMC method uses particles to simulate collision effects in rarefied gas flow by collecting groups of particles into cells that are smaller than the order of a mean free path. In Step 6 of section 2.6.1, pairs of particles inside a cell are selected at

random and a collision probability is evaluated that is proportional to the product of the relative velocity and the collision cross section for each pair. The probability is compared with a random number to determine if that collision occurs. If so, some form of collision dynamics is performed to alter the properties of the colliding particles. The No Time Counter (NTC) method [26] is adopted to determine if a collision occurs in this study. A special treatment to handle collisions between particles of different weights will be presented later.

There are two types of collisions that are important in Hall thruster plumes: elastic, or momentum exchange (MEX) collisions and charge exchange (CEX) collisions. There are two kinds of elastic collisions: atom-atom and atom-ion collision. For atom-atom collision, the Variable Hard Sphere [26] model is used and the collision cross section for xenon is

$$\sigma_{el}(Xe, Xe) = \frac{2.12 \times 10^{-18}}{g^{2\omega}} m^2 \tag{2.35}$$

where g is the relative velocity and ω=0.12 is related to the viscosity temperature exponent for xenon. For atom-ion elastic interactions, one common choice is to use the following cross section of Dalgarno et al. [48]:

$$\sigma_{el}(Xe, Xe^+) = \frac{2.12 \times 10^{-18}}{g} m^2 \tag{2.36}$$

Another choice, which is adopted in this study, is to set the MEX cross section equal to the CEX cross section.

In all elastic interactions, the collision dynamics is modeled using isotropic scattering together with conservation of linear momentum and energy to determine the post-collision velocities of the colliding particles. Charge exchange concerns the transfer of one or more electrons between an atom and an ion. For singly charged ions, the following cross sections measured by Pullins et al. [49] and Miller et al. [50] are used

$$\sigma_{el}(Xe, Xe^+) = 1.0 \times 10^{-20} \left(87.3 - 13.6 \log(\frac{m_c g^2}{2e})\right) m^2 \tag{2.37}$$

where m_c is the reduced mass. Also, Refs. [49] and [50] reported that the CEX cross section for double charged ion is approximately half as large as for single charged ions at corresponding energies. Therefore, we use half of the cross section of a single charged ion for that of a double charged ion. When a charge exchange collision occurs, an ion with the neutral bulk velocity is created at the original ion's location. The original ion loses its charge, is removed from the list of ions, and is added to the list of neutral atoms. In the present model, it is assumed that there is no transfer of momentum accompanying the transfer of electron(s). This assumption is based on the premise that charge exchange interactions are primarily at long range.

2.6.6 Backpressure Treatment

Hall thrusters are designed for use in space but are tested in ground vacuum chambers. In space, an almost perfect vacuum exists. However, on the ground a finite background chamber pressure always exists which may affect simulation results. Therefore, the background pressure should be considered for accurate simulations. In particle simulations, the most convenient treatment of background pressure is to adopt static background particles. Each cell contains a few particles with velocities sampled from a zero-centered Maxwellian velocity distribution function. These particles participate in collisions with plume particles and change the velocities of other particles, but their positions and velocities do not change. In this thesis, we adopt this method to represent the background pressure.

2.6.7 Particle Weight

Particle weighting is enabled in MONACO-PIC. Each particle introduced into the simulation domain is assigned with a relative weight ratio W_p. The overall particle weight is determined by multiplying W_p by the local cell weight ratio W_c. When particles travel from one cell into another, a clone or destroy process is performed based on the ratio of the two cell weights; this particle's relative ratio does not change.

Weight ratios are assigned to background static particles as well.

One issue for our approach is how to handle collisions, for which we use the following procedure: When two particles collide, the particle of larger weight is split into two. One of these two new particles has the same weight ratio as the lighter original particle and a collision is performed between these two particles with the same weight. The second new particle keeps the rest of the weight and does not participate in the collision. This treatment is quite similar to [51], which reported a simulation of flows with trace species.

In axisymmetric simulations cell volumes change dramatically. Therefore, we must handle a cell volume calculation with care. Cells located at a large radius have a large volume while cells around the axis have rather small volumes. Relative particle weights for the background static particles are different from those of normal particles, and can also be much smaller. When a background static particle with a small weight ratio collides with a normal particle, the normal particle will split into two. This split must be processed to calculate the correct velocity change for the normal particle.

This splitting scheme is quite useful for solving the issues with the neutral number density and fluxes of ions and neutral atoms. However, one side-effect of this scheme is that after the split process an increasing number of low-weight particles exists due to collisions. Therefore, to reduce the number of neutral particles, we implement the following process: If a neutral particle's relative weight W_p is larger than a threshold value W_{thresh}, it is kept in the simulation with its original weight; otherwise, the particle is either discarded from the simulation or kept in the simulation statistically by changing its relative weight ratio to the threshold value. Ion particles are essential to the simulations, and are, therefore, kept in the simulation without any change of their weights.

2.7 MONACO-PIC

The particular DSMC-PIC code, named MONACO-PIC, employed in this study was first developed by Dietrich and Boyd [52] in 1996. Since then, MONACO-PIC has been further modified and expanded by Cai [1], and applied to a wide variety of rarefied gas problems [1] [19] [53]. MONACO-PIC-V3.0 is a general-purpose DSMC simulation package written in C++ for simulating two-dimensional, axisymmetric, or three-dimensional rarefied gas flows. It contains object-oriented features and different functionalities are separated for easy maintenance and update.

Its major structure is a double pointer for cell data, which enables an excellent performance on parallel machines. Inside each cell, the major data structures are two linked lists for particles, and these linked lists toggle as a current list and a backup list. When particles move, they move from the current list to the backup list. This linked list treatment achieves great efficiency. Besides the two linked lists of particles, neighboring cell information and boundary information are saved in the cell structure as well. These data structures make MONACO-PIC capable of simulating problems with complex geometry.

MONACO-PIC employs the VHS or Variable Soft Sphere [54] (VSS) collision models, the variable rotational energy exchange probability model of Boyd [55] [56], and the variable vibrational energy exchange probability model of Vijayakumar *et al.* [57] although these models are turned off in all simulations of this thesis due to the fact that xenon is monatomic. Cell weighting factors and time-steps may be set uniquely for each cell in the grid. A sub-cell scheme is implemented for selection of collision pairs where the number of sub-cells is scaled by the local mean free path.

CHAPTER 3

HYDRODYNAMIC PLASMA MODEL

3.1 Introduction

In plasma plume simulations, boundary conditions are very important because they determine the plasma plume characteristics. MONACO-PIC needs boundary conditions at the thruster exit, the cathode exit, and at boundary edges. Among these boundary conditions, flow conditions at the thruster exit are most important because the plasma plume characteristics, such as ion velocity, ion number density, and plasma potential, are very sensitive to these conditions. Therefore, the determination of the boundary conditions at the thruster exit is an essential prerequisite to accurate plasma plume simulation.

As mentioned in Section 1.7, hydrodynamic modeling is a faster method to simulate plasma flows than particle-based methods. Therefore, we use this method to represent the plasma flow within the thruster channel of the D55 thruster and to determine the initial boundary conditions at the thruster exit.

A wide array of hydrodynamic plasma codes for Hall thrusters has been developed [58] [59] [60] [61] [15] [62]. Hydrodynamic models can range from one-dimensional to quasi one-dimensional–incorporating sheath and wall effects–to axisymmetric in terms of their simulation domains. These models can converge to a steady-state solution or can produce time-dependent flowfields. For all of these models, various solution methods are employed to solve the discretized governing

equations, including finite-difference, finite-element, and finite-volume.

Given the annular shape of the acceleration channel for the D55 thruster, a cylindrical coordinate frame is useful for simulation. For our purpose, a hydrodynamic model of the quasi-neutral plasma flow within the thruster is used [63]. The model employs a two-dimensional axisymmetric finite-volume method, and thus assumes symmetry of the flow about the thruster centerline. This chapter provides a review of the hydrodynamic model. A more detailed description of the model can be found in Yim [63].

3.2 Governing Equations

The hydrodynamic model uses a multi-fluid description to model each species in a plasma flow. In a fluid description, mass, momentum, and energy conservation equations are used to characterize the properties of the flow. Ions, neutral atoms and electrons are modeled in the hydrodynamic model. Each of the three species are governed by their own set of conservation equations. Hence, this section describes these conservation equations for each species.

3.2.1 Ion Conservation Equations

The ions are modeled using a finite-volume flux-splitting method on an axisymmetric Cartesian mesh [64]. The steady state axisymmetric ion continuity equation is

$$\frac{\partial(\rho v_z)}{\partial z} + \frac{\partial(\rho v_r)}{\partial r} = \beta n_a \rho \tag{3.1}$$

The right hand side of Eq. (3.1) is a source term that describes the creation of ions due to ionization. The ionization rate β is defined in Section 3.3 of this work.

The axial and the radial components of the steady ion momentum equation are

$$\frac{\partial(\rho a^2 + \rho v_z^2)}{\partial z} + \frac{\partial(\rho v_z v_r)}{\partial r} = enE_z + \beta n_a v_a \rho \tag{3.2}$$

$$\frac{\partial(\rho v_z v_r)}{\partial z} + \frac{\partial(\rho a^2 + \rho v_r^2)}{\partial r} = enE_r + \frac{\rho a^2}{r} \tag{3.3}$$

For isothermal ions, the equation of state is $p = \rho a^2$, where a is the local acoustic speed. The first source term on the right hand side of Eq. (3.2) represents the force resulting from the axial component of the electric field E_z. The second source term is a frictional drag force arising from ionization collisions of the neutral atoms. The force due to the radial component of the electric field is represented in the source terms as well as a term that arises due to the axisymmetric nature of the formulation.

The energy conservation equation is ignored for the ions. In Hall thruster channels, the ion temperature is much lower than the electron temperature and can, therefore, be considered negligible [65]. Since we assume cold ions, the ion energy equation can be eliminated, which simplifies the set of governing equations.

It should be mentioned that the hydrodynamic model considers only three species: singly-charged ions, neutral atoms, and bulk plasma electrons. The model does not represent doubly and other higher charged ions. However, it is reported [66] that some portion of the plasma plume of a D55 thruster consists of doubly charged ions. Therefore, we need to consider these double charged ions for our simulations. Hence, we introduce the mixed charge ions and mixed ion velocity as follows

$$ion\ charge = (n^+ e + 2 \times n^{2+} e)/(n^+ + n^{2+}) \tag{3.4}$$

$$u = (n^+ u^+ + n^{2+} u^{2+})/(n^+ + n^{2+}) \tag{3.5}$$

Then, in the hydrodynamic model, ion charge and velocity represent mixed values of a single charge ion and a double charged ion, respectively.

3.2.2 Neutral Atom Conservation Equations

Neutral atoms are modeled as a one-dimensional flow through the acceleration channel. Therefore, only the continuity and axial momentum equations are considered. The steady continuity and momentum equations are given as

$$\frac{\partial(n_a v_a)}{\partial z} = -\beta n n_a \tag{3.6}$$

$$\frac{\partial(n_a a^2 + n_a v_a^2)}{\partial z} = 0 \tag{3.7}$$

The source term for the continuity equation is negative because neutral atoms are depleted by ionization. The creation of neutral atoms due to ion recombination at the walls is ignored because its rate is approximately an order of magnitude lower compared to the bulk flow rate. No source terms are considered for the momentum equation.

3.2.3 Electron Conservation Equations

The plasma within the thruster channel is assumed to be electrically neutral. The charge neutrality condition sets the electron number densities equal to the calculated ion number densities, and the electron continuity equation is not needed.

The momentum equation is used to calculate the electric field. The steady electron momentum equation is

$$\nabla \cdot (\rho_e \overrightarrow{v_e}\,\overrightarrow{v_e}) + \nabla p_e = -en(\overrightarrow{E} + \overrightarrow{v_e} \times \overrightarrow{B}) - \frac{m_e m_h}{m_e + m_h} n \nu_e (\overrightarrow{v_e} - \overrightarrow{v_h}) \tag{3.8}$$

The source terms include the Lorentz force and a frictional force that arises from collisions with heavy particles. Subscript h represents heavy particles, both ions and neutral atoms. Due to the low mass of electrons, electron time scales are much lower than those of ions. The primary concern for solving the electric field is the ion motion. It is assumed that the electrons move fast enough so that their motion reaches an equilibrium on the ion time scale. Given sufficiently fast electrons, they can be considered inertia-less. Therefore, the first term on the left hand side of Eq. (3.8) is neglected. The velocity term in the Lorentz force on the right hand side can also be ignored under the time-averaged assumption. The electrons trapped by the magnetic field revolve around the magnetic field lines, but are free to move along

the magnetic field lines. Then, if we consider the ion time scale, the motion of the electrons around the magnetic field lines cancels out. The net motion will then be only along the magnetic field lines. This is called the guiding center motion. Since the guiding center moves in the same direction as the field lines, the cross product of the Lorentz force cancels out. Further simplification of the source terms is possible in the collision drag term, since $m_h \gg m_e$ and $v_e \gg v_h$. The electron momentum conservation equation is thus reduced to

$$\overrightarrow{E} = -\frac{1}{en}(\nabla p_e - m_e n \nu_e \overrightarrow{v_e}) \tag{3.9}$$

Using the equation of state, the definition of electron current density, and the definition of electron mobility

$$p_e = nkT_e \tag{3.10}$$

$$\overrightarrow{j_e} = -en\overrightarrow{v_e} \tag{3.11}$$

$$\mu_e = \frac{e}{m_e \nu_e}, \tag{3.12}$$

Eq. (3.9) can be rewritten

$$\overrightarrow{E} = \frac{1}{en}(\frac{\overrightarrow{j_e}}{\mu_e} - \nabla(nkT_e)) \tag{3.13}$$

The calculation methods to obtain the electron current density and the electron mobility are described in section 3.3.

The electrons are assumed to have constant temperature along the magnetic field lines. Therefore, only a one-dimensional profile of the electron temperature is needed. The electron temperature can be calculated using the electron energy equation. However, for simplicity, the energy equation is not considered in the model. Instead, a fixed electron temperature profile is used.

3.3 Plasma Properties

In order to solve the conservation equations for each species, several plasma properties need to be calculated. Therefore, this section discusses the ionization rate, the electron current density, the electron mobility, the secondary electron emission, and the plasma sheath.

3.3.1 Ionization Rate

The ionization rate β appears in the source terms of the ion and neutral atom continuity equations and the ion momentum equation. The ionization rate can be evaluated as [67]

$$\beta = \sigma_{ion} v_{th} \left(1 + 2\frac{kT_e}{eE_{ion}}\right) exp\left(-\frac{eE_{ion}}{kT_e}\right) \tag{3.14}$$

For the calculation of the ionization rate, the ionization collision cross-section σ_{ion}, the electron thermal speed v_{th}, and the ionization energy E_{ion} need to be known. The ionization collision cross-section and the ionization energy are properties of the propellant species. Typically, the ionization collision cross-section depends on the electron energy [68], but for simplicity, this model uses a constant. The ionization energy in this model is the first ionization energy, meaning the minimum energy necessary to remove an electron from the ground state of the neutral atom.

3.3.2 Current Density

The calculation of the electric field in Eq. (3.13) involves the electron current density. For Hall thrusters, the total discharge current of the device is one of the adjustable operational parameters. The total discharge current is composed of the ion and electron current contributions

$$I_d = I_i + I_e, \tag{3.15}$$

where the ion current can be found by integrating the ion current density over the cross-section area of the thruster channel A

$$I_i = \int_A env_z dA \tag{3.16}$$

The electron current density is assumed to vary only in the axial direction and is found by dividing the electron current by the cross-sectional area

$$j_e = \frac{1}{A}(I_D - \int_A env_z dA) \tag{3.17}$$

3.3.3 Electron Mobility

The electron mobility needs to be considered to calculate the electric field in Eq. (3.13). The electron mobility depends on the electron collision frequency. Classical mobility is dependent on electrons colliding with ions or neutral atoms. Electron-ion interactions are dominated by small angle Coulomb collisions. These interactions between charged particles occur with a frequency of [69]

$$\nu_{ei} = \frac{ne^4 \ln \Lambda}{2\pi\epsilon_o^2 m_e^2 v_e^3} = \frac{ne^4 \ln \Lambda}{2\pi\epsilon_o^2 m_e^2 (3kT_e/m_e)^{3/2}} \tag{3.18}$$

where the Coulomb logarithm

$$\ln \Lambda = \ln(n\lambda_D^3) \tag{3.19}$$

is dependent on the electron Debye length

$$\lambda_D = \sqrt{\frac{\epsilon_o kT_e}{ne^2}} \tag{3.20}$$

The electron-neutral atom collision frequency is modeled by

$$\nu_{ea} = \sigma_{ea} n_a v_{th}, \tag{3.21}$$

where σ_{ea} is the electron-neutral atom collision cross-section.

The electron mobility obtained by this procedure is small compared to experimen-

tal results [70]. As a consequence, additional anomalous electron transport must be provided through augmentation of the electron momentum transfer frequency. Two models for this additional term are considered: Bohm diffusion, the result of turbulence, and secondary electron emission. These models can be used stand-alone throughout the domain or concurrently in different regions of the thruster. We first consider the Bohm diffusion correction which is simply stated as

$$\nu_B = \alpha_B \omega_e \tag{3.22}$$

The classical value of the Bohm coefficient α_B is 1/16, but is often empirically adjusted to be smaller than the classical value. We next consider the secondary electron emission that is due to electrons colliding with the walls of the channel. The wall-collision correction is based on the idea that electrons collide with the sheath with a relative frequency resulting from their thermal energy and the height of the acceleration channel. A simple form for the electron-wall collision frequency can be modeled as [60]

$$\nu_{wall} = \alpha_{wall} \frac{v_{th}}{h} exp\left(-\frac{e\phi_s}{kT_e}\right), \tag{3.23}$$

where h is the channel width and ϕ_s is the sheath potential.

The total electron collision frequency is a sum of the Bohm diffusion term and the collision frequencies of electrons with ions, electrons, and the walls. In an SPT, the wall collision term is important because its walls are di-electric. However, this term is not important in a TAL because they have metallic walls. For more discussion of secondary electron emission, see Section 3.3.4. A correctional term is also applied to the electron mobility that adjusts for mobility across magnetic field lines. The final result for the cross field mobility is then

$$\mu_{e\perp} = \frac{\mu_e}{1 + (\omega_e/\nu_e)^2} = \frac{e/(m_e\nu_e)}{1 + (\omega_e/\nu_e)^2}\ , \tag{3.24}$$

where

$$\nu_e = \nu_{ei} + \nu_{ea} + \nu_{wall} + \nu_B \tag{3.25}$$

3.3.4 Secondary Electron Emission

In secondary electron emission additional electrons, called secondary electrons, are emitted from the surface of a material when an incident particle (often a charged particle such as electron or ion) impacts the material with sufficient energy. The number of secondary electrons emitted per incident particle is called the secondary emission yield.

Electrons accelerated by the E × B field frequently collide with the acceleration channel walls and deposit some of their energy into the walls. If the collision energy is high enough, secondary electrons are ejected after the high energy electrons have collided with the walls. These secondary electrons emerge at significantly lower temperatures than the primaries, which results in a lower bulk plasma temperature and a non-Maxwellian velocity distribution. The secondary electron emission coefficient describes the number of low energy electrons that results from the impact of a single high energy electron with a particular wall material. In an SPT, secondary electron emission at dielectric surfaces plays an important role in electron transport. In a TAL, where the acceleration channel is metallic, secondary emission effects are less important. The secondary electron emission yield from metals is much lower than the yield from insulators: In metals, the maximum of the yield rarely exceeds 1, while insulators may show values up to 10 or more [71]. Since this effect is thought to be small for TAL thrusters, we ignore it.

3.3.5 Plasma-Sheath

The sheath is a plasma phenomenon that occurs for plasmas bounded by wall surfaces. Since electrons have much higher thermal velocities than ions, they are more quickly depleted at a wall, resulting in a net positive charge of the plasma. This means that

the plasma has a positive potential with respect to the wall. This potential cannot be distributed over the entire plasma because Debye shielding will confine the potential variation to a layer of the order of several Debye lengths in thickness. This layer is called a "sheath". The sheath potential has a certain value, so that the net current flow (from both ions and electrons) to the walls equals zero. To calculate the resulting potential across the sheath, the following equation can be obtained from the electron continuity and momentum equations [72]

$$\phi_s = \frac{kT_e}{e} \ln \left(\frac{1-s}{v_s \sqrt{2\pi m_e/(kT_e)}} \right), \tag{3.26}$$

where v_s is the ion entrance velocity into the sheath and s is the secondary electron emission coefficient. This coefficient is set to zero for TAL thrusters.

For the calculation of the sheath, we cannot use some of the assumptions we made in the previous section (e.g., quasi-neutrality). However, we can define the potential to be zero at the sheath edges and assume that the electric field is also zero there [73]. Having boundary conditions at the sheath edges, we now have a criterion, known as the Bohm criterion, to calculate the ion velocity. The Bohm criterion assumes that the ion velocity at the sheath edge is equal to the Bohm velocity

$$v_B = \sqrt{\frac{kT_e}{m_i}} \tag{3.27}$$

Under this assumption, however, the electric field at the plasma edge approaches infinity (a singular point). Therefore, a smooth matching of the plasma and sheath solution is impossible. However, a solution is possible if we set the ion velocity to a slightly different value than the Bohm velocity. The electric field then becomes a continuous function that increases from a relatively small value (but not zero) at the plasma–sheath interface to a maximal value at the wall [60] [74] [75] [76]. The present work uses a nonzero electric field at the plasma–sheath interface and the plasma velocity at that interface to determine the entrance conditions for the sheath.

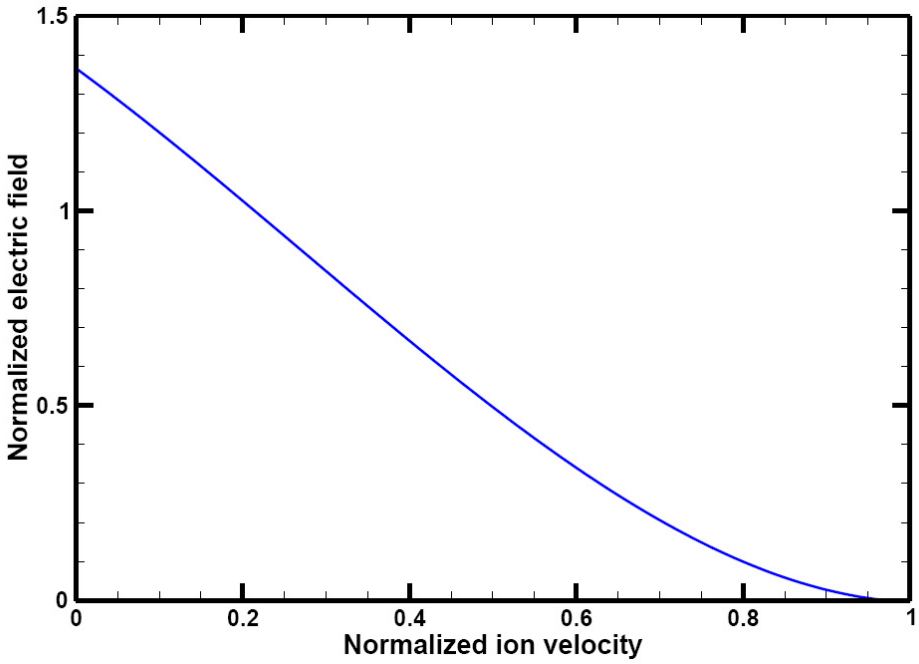

Figure 3.1: The relation between the electric field (normalized by the electron temperature over the Debye length) and the ion velocity (normalized by the Bohm velocity) at the plasma–sheath interface

Instead of the Bohm condition, a calculated relation between the electric field and the ion velocity at the sheath edge is used for the hydrodynamic model [60]. Figure 3.1 shows the relation between the ion velocity and the electric field at the plasma edge. It is obvious in Fig. 3.1 that the electric field decreases from the characteristic value of T_e/R_d (R_d is the Debye length) down to zero when the velocity approaches the Bohm velocity.

Once an electric field at the sheath edge is established, we can use it to calculate the density gradient through [77]

$$\nabla n = -\frac{kT_e}{enE} \tag{3.28}$$

3.4 Magnetic Field Considerations

The magnetic field profile plays an important role in the plasma dynamics of a Hall thruster channel. As mentioned in section 1.5, the magnetic field of Hall thrusters

is strong enough to magnetize the electrons while sufficiently weak to not magnetize the ions. Typically, the time step of a thruster plasma model is based on the ion time scale; so the electrons are assumed to move fast enough to adapt their motion. This assumption allows for simplifying the calculation of electron properties within the channel.

A one-dimensional approximation of the magnetic field makes the model quite simple. The magnetic field profile is assumed to vary only in the axial direction, such that the magnetic field lines lie along the radial direction. Consequently, all dynamics in the radial direction occur along the magnetic field lines and the cross-field dynamics occur in the axial direction. This dynamic feature provides great benefit for solving the momentum equations for the ions and the electrons.

The axial component of the electric field calculation in Eq. (3.9) is not changed, but the radial component can be simplified. Since the electrons are assumed to thermalize along magnetic field lines, the electron temperature can be considered to be constant along magnetic field lines. The radial component of the electron current density can be ignored because there is no net electron current flowing along those field lines. Then the electric field in the radial direction can be simplified as

$$enE_r = -\frac{\partial(nkT_e)}{\partial r} = -\frac{kT_e}{m_e}\frac{\partial \rho}{\partial r} \tag{3.29}$$

By introducing an effective sound speed of

$$a^* = \sqrt{a^2 + \frac{kT_e}{m_i}}\ , \tag{3.30}$$

the ion momentum equations can be rewritten as

$$\frac{\partial(\rho(v_z^2 + a^{*2}))}{\partial z} + \frac{\partial(\rho v_z v_r)}{\partial r} = \frac{j_{ez}}{\mu_e} + \beta n_a v_a \rho \tag{3.31}$$

$$\frac{\partial(\rho v_z v_r)}{\partial z} + \frac{\partial(\rho(v_r^2 + a^{*2}))}{\partial r} = \frac{\rho a^2}{r} \tag{3.32}$$

3.5 Boundary and Input Conditions

The hydrodynamic model simulates the plasma discharge within a Hall thruster acceleration channel from the anode to the exit plane. The domain is an axisymmetric slice of the channel that is bounded by the inner and outer walls. The domain is covered using a regular structured Cartesian mesh. Ghost cells are employed to set the boundary conditions around the domain. At the anode, the neutral and electron temperatures are set. Assumed conditions for the plasma density and ion velocity are also set at the anode. The inflow neutral atom velocity and number density at the anode are determined based on the neutral atom thermal velocity and the mass flow rate. At the exit plane, zero gradient Neumann outflow conditions are used for properties of the ions, neutral atoms, and electrons.

The boundaries of the simulation are set at the plasma–sheath interface instead of the actual wall. This is necessary because several assumptions made earlier–such as quasi-neutrality–break down within the sheath.

The simulation uses the following measurements as input conditions: discharge voltage, discharge current, propellant mass flow rate and magnetic field profile. The voltage difference between the anode and cathode is fixed. The discharge current is not fixed, but can be adjusted depending on the mass flow rate and magnetic field configuration. For the hydrodynamic simulations, the magnetic field profile and the thruster geometry are directly applied to the model. The propellant mass flow rate is used to set the inflow neutral atom number density. The discharge current is used to calculate the electron current density within the thruster. The discharge voltage and the plasma potential at the thruster exit are used to calculate the ion velocity within the thruster. The plasma potential at the thruster exit can be calculated from the measured ion axial velocity using

$$\Delta\phi = \frac{1}{2} m_i v_i^2 / e, \tag{3.33}$$

where e is the elementary charge. The simulation also uses the following unmeasured input parameters: the ion boundary conditions at the anode, the electron temperature at the anode, and the electron mobility terms. The values of these unknown input parameters in the simulation are calibrated to match the available measured data.

3.6 Solution Scheme

The solution scheme of the overall method centers primarily around the ion conservation equations. As source terms in the ion equations, we incorporate plasma properties which are found using the equations of neutral atoms and electrons. The model is solved using a flux-splitting finite volume scheme [64]. Each cell of the simulation domain is treated as a control volume where the conservation equations are solved. Apart from the contributions of the source terms, the fluxes between each of the cells also affect the conserved values. At each cell interface, the fluxes are calculated following the isothermal version of the Roe solver [64] [78].

The cell-centered conserved values are found by using the following process: First, the simulation is initialized with a uniform flow based on the inflow conditions throughout the domain. Second, the various plasma properties are calculated based on the electron parameters. Third, the results of these calculations are used to find the boundary conditions and source terms. Next, the flux throughout the domain is calculated. This process is iterated until a steady state is reached. We decide the steady state is reached when the potential difference at the center of the thruster exit between successive time steps is smaller than a certain tolerance.

CHAPTER 4

HYDRODYNAMIC PLASMA MODEL RESULTS

In the previous chapter, the hydrodynamic model was reviewed. In this chapter, hydrodynamic simulations are performed to model the plasma discharge within the D55 Hall thruster for xenon propellant. The discharge voltage and current relation is studied in Section 4.1. Plasma properties of the D55 Hall thruster channel are studied in Section 4.2. The nozzle exit conditions of the D55 Hall thruster are investigated in Section 4.3.

4.1 Discharge Voltage and Discharge Current Characteristics

The hydrodynamic model is applied to the D55 thruster to analyze the relation between the discharge current and discharge voltage. The one dimensional magnetic field approximation is used for this study. The nozzle-shaped exit geometry of the D55 is ignored because of a code sensitivity problem. This sensitivity problem will be discussed in Section 4.2.1.

By definition, the discharge voltage in a Hall thruster is the voltage difference between the anode and the cathode. The hydrodynamic model requires discharge current and discharge voltage as input parameters. Therefore, the model can not calculate the discharge voltage or discharge current. However, if we assume that the voltage difference between the thruster exit and the cathode is constant, then the plasma potential drop between the anode and the thruster exit can be studied as a

function of the given discharge current.

The simulation results are compared with experimental data. Experimental work has been performed on the D55 Hall thruster to evaluate the relation between the discharge current and discharge voltage [79]. The test chamber is 5 m in diameter and 20 m in length and the base pressure is $2 \times 10^{-6} torr$ during operation. The measurements were taken using isolated digital multimeters (DMM) with a nominal input impedance of 10 Megohms [79]. Anode flow rates of 2.65, 3.57, and 5.50 mg/sec were chosen to provide a discharge current range from 2 A to 6 A.

Figures 4.1, 4.2, and 4.3 show the comparison between measured data and simulation results for the voltage and current characteristics. Figure 4.1 shows the results for the anode flow rate of 2.65 mg/sec. The experimental data show that current decreased with increasing voltage below 250 V, and the current is constant at voltages over 250 V. However, the simulation results fail to show this trend. Even though a direct comparison is not possible because the simulation results do not include the voltage difference between the thruster exit and the cathode, it is clearly shown that the current increases with voltage. Because of the code sensitivity problem, the hydrodynamic model can not simulate voltages when the discharge current is higher than 3 A for the flow rate studied in Figure 4.1. Figures 4.2 and 4.3 show similar results. The experimental data show that the current is almost constant across the whole voltage range, while the simulation results show that the current increases with voltage. In Fig. 4.2, the hydrodynamic model can not simulate voltages when the discharge current is higher than 4 A because of the code sensitivity problem.

One possible reason for the disparity between experiment and simulation is the magnetic field configuration used in the simulation. We assumed a profile of the magnetic field within the D55 channel because accurate magnetic field profiles for the thruster are not available to us. It is known that the magnetic field has a gaussian profile with a maximum near the thruster exit and about a half maximum strength

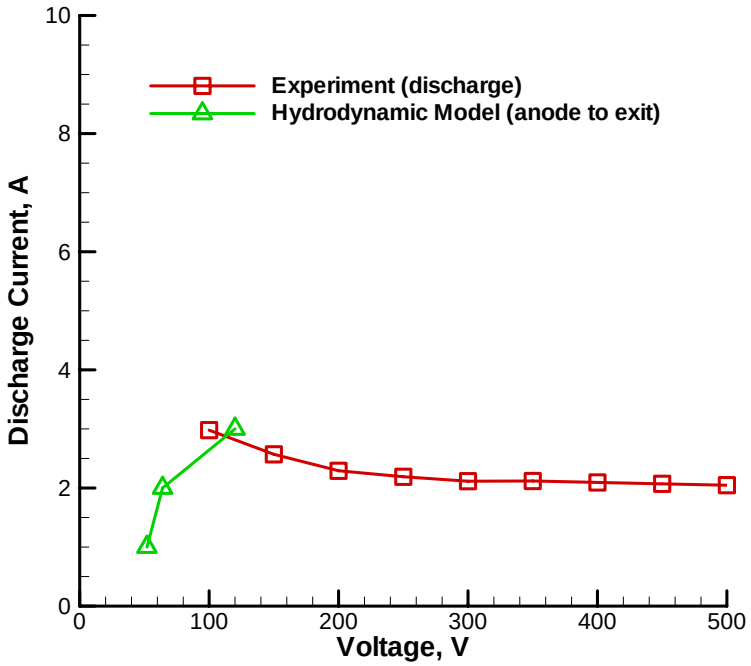

Figure 4.1: Current-Voltage characteristics, flow rate = 2.65 mg/sec

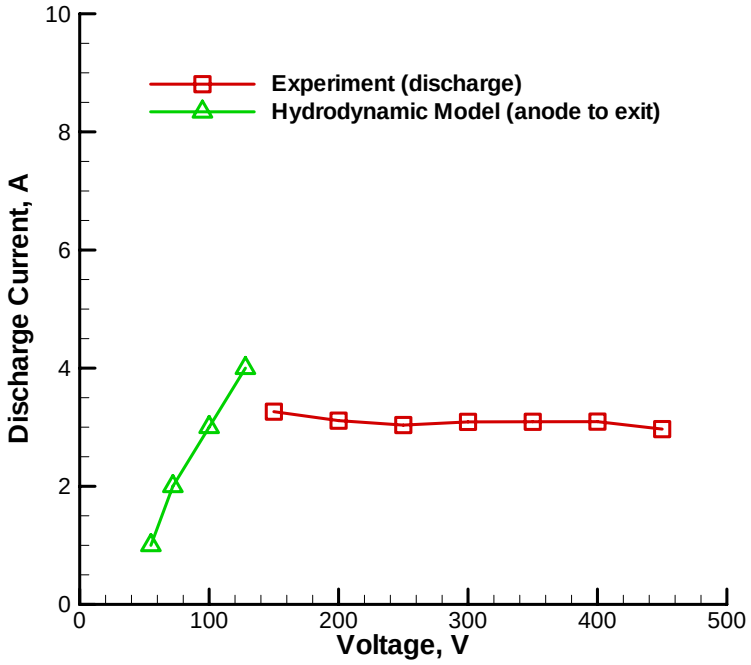

Figure 4.2: Current-Voltage characteristics, flow rate = 3.52 mg/sec

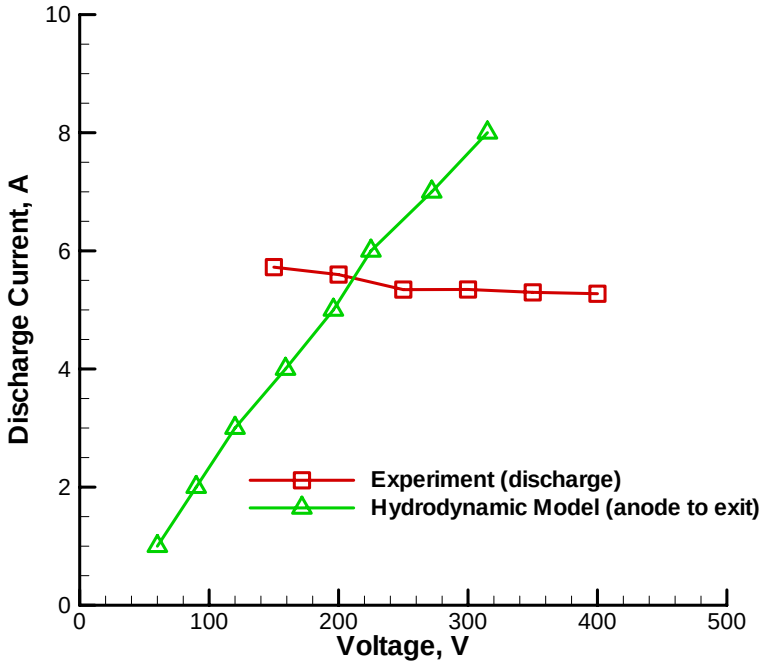

Figure 4.3: Current-Voltage characteristics, flow rate = 5.50 mg/sec

at the anode in SPT type thrusters [80]. We assume that the magnetic field profile of the D55 is also a gaussian profile with a half maximum at the anode and a maximum at the exit. Figure 4.4 shows the magnetic field profile used in the simulations. The magnetic field has an enormous effect by confining electrons within the thruster channel and ionization occurs through the electrons. Therefore, an inappropriate magnetic field configuration may result in an incorrect discharge current. To study the magnetic field effect, we tested different magnetic field profiles. Figure 4.5 shows three different magnetic field profiles. Case 1 is a constant magnetic field profile. Case 2 is a gaussian shape with a half maximum at the anode. Case 3 is a gaussian shape with a 1/4 maximum at the anode. Figure 4.6 shows the voltage-current characteristics obtained with these magnetic field profiles for the flow rate of 5.5 mg/sec. One can see that different magnetic field profiles give only slightly different voltage-current characteristics. Because of the code sensitivity problem, the hydrodynamic model

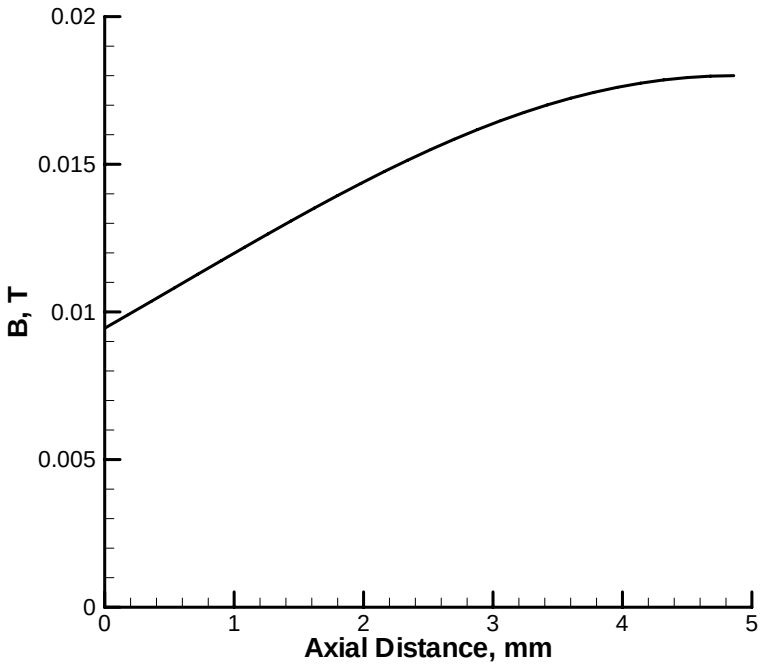

Figure 4.4: Magnetic field profile used in the simulations

can not simulate voltages when the discharge current is higher than 3 A for cases 1 and 3 in Figure 4.6.

Another possible reason for the disparity is the electron temperature profile used in the simulation. Instead of solving the electron energy balance equation, we assume a profile of the electron temperature within the D55 channel, because the balance equation makes the hydrodynamic model even more sensitive and it always crashes. Figure 4.7 shows the electron temperature profile used in the simulation. This profile has a maximum of 28.5 eV at the exit based on Szabo [17] and a half maximum at the anode. To assess any electron temperature effect, different electron temperature profiles are tested. Figure 4.8 shows three different electron temperature profiles. Case 1 is a constant electron temperature. Case 2 is a gaussian shape with a half maximum at the anode. Case 3 is a gaussian shape with a 1/4 maximum at the anode. Figure 4.9 shows the voltage-current characteristics obtained with the different

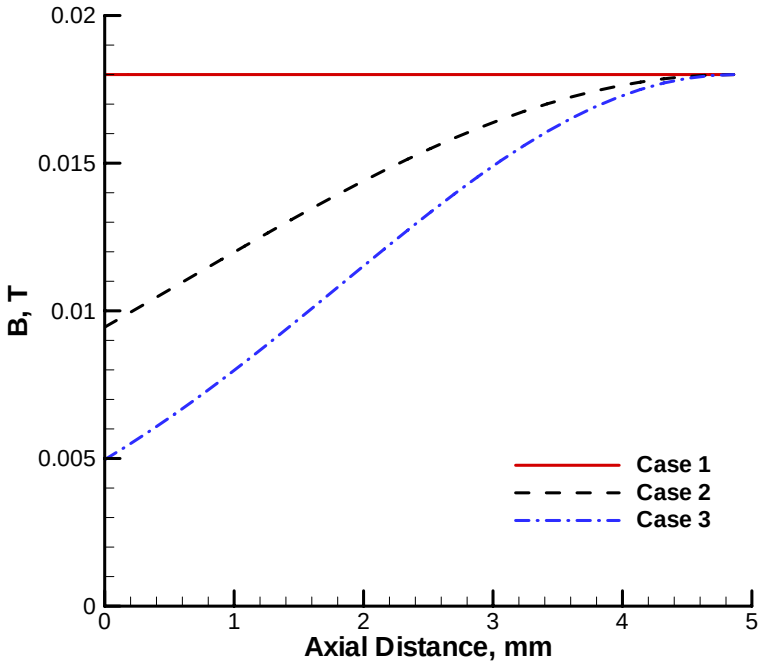

Figure 4.5: Magnetic field profile sets

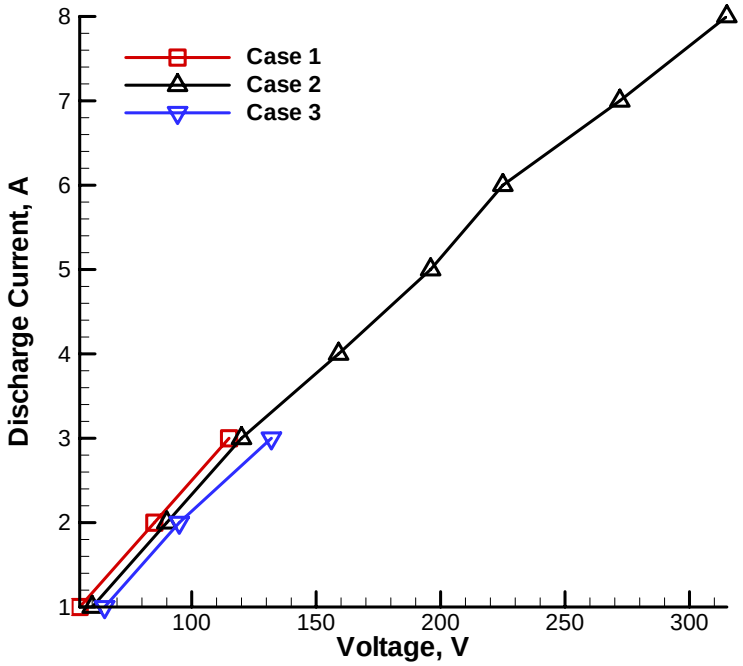

Figure 4.6: Current-voltage characteristics at various magnetic field profiles, flow rate = 5.5 mg/sec

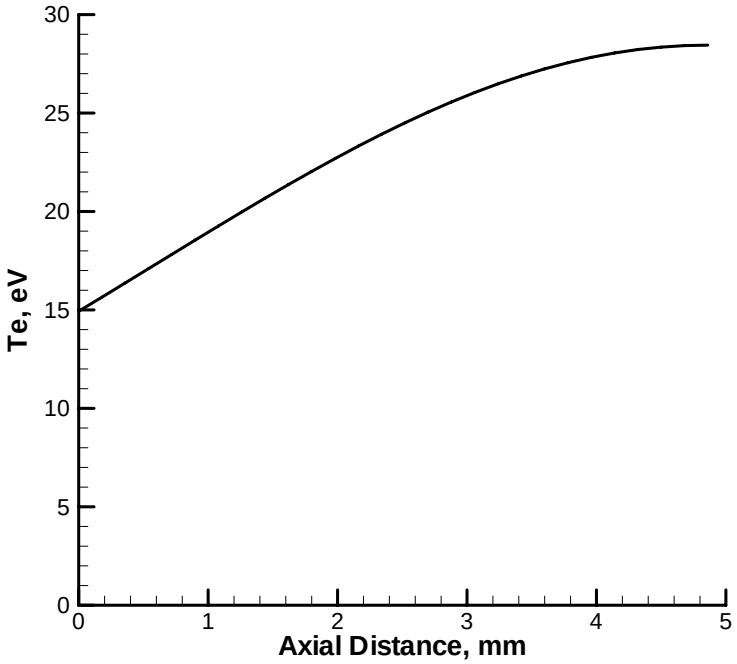

Figure 4.7: Electron temperature profile used in the simulations

electron temperature profiles for the flow rate of 5.5 mg/sec. Because of the code sensitivity problem, the hydrodynamic model can not simulate case 1 at all. For case 2, the hydrodynamic model can only simulate voltages when the discharge current is less than 2 A. However, Fig. 4.9 shows clearly that different electron temperature profiles give different voltage-current characteristics.

Another possible reason for the disparity is the Bohm coefficient. In our simulations, we assumed a coefficient of 1/100 [61] for the Bohm mobility term for all three flow rates. However, the Bohm coefficient may not be constant for different flow rates [81]. Moreover, the Bohm coefficient may vary within the channel. The electron momentum conservation equation is

$$\overrightarrow{E} = \frac{1}{en}\left(\frac{\overrightarrow{j_e}}{\mu_e} - \nabla(nkT_e)\right) \tag{4.1}$$

From Eq. (4.1), a higher Bohm coefficient decreases μ_e and gives a stronger electric

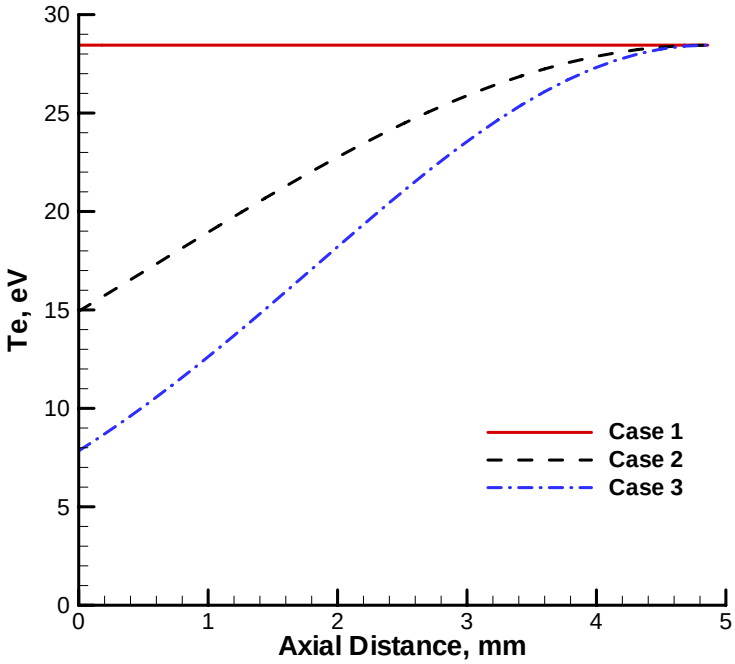

Figure 4.8: Electron temperature profile sets

field, and the potential drop becomes stronger. Therefore, using a different Bohm coefficient for a different flow rate may be a solution to obtain more accurate results. Figure 4.10 shows the voltage-current relation for various Bohm coefficients. It is clearly shown that the voltage drop increases with Bohm coefficient. For each Bohm coefficient, agreement with one experimental data point is obtained. This suggests that perfect agreement with all measured values could be obtained by more variation of the Bohm coefficient. Variable Bohm coefficient in a simulation domain would be another solution. However, the Bohm mobility is difficult to model accurately. Further research is required and the underlying physical processes should be investigated.

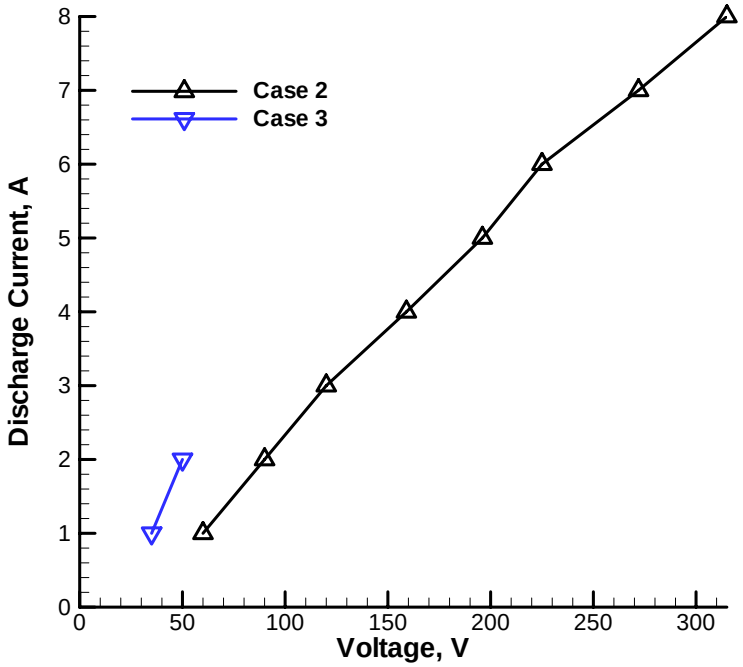

Figure 4.9: Current-voltage characteristics for various electron temperature profiles, flow rate = 5.5 mg/sec

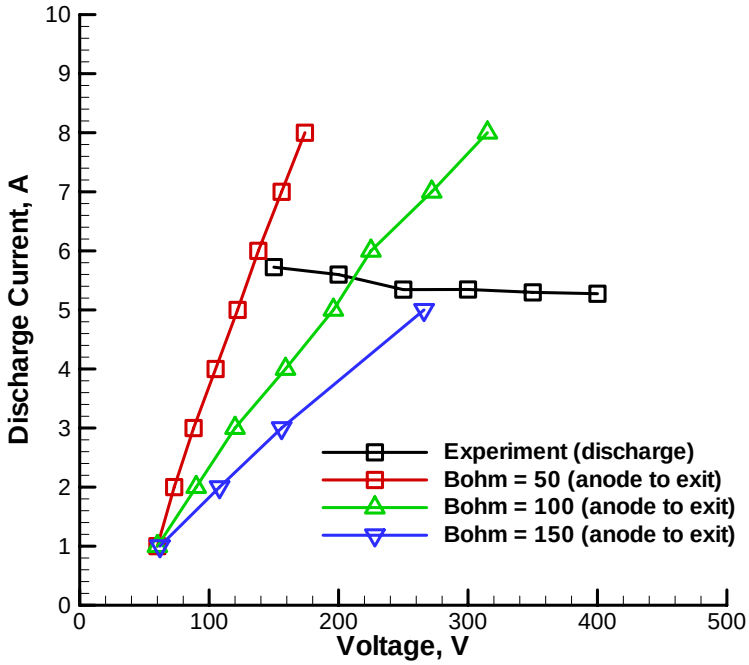

Figure 4.10: Current-voltage characteristics at various Bohm coefficient, flow rate = 5.50 mg/sec

4.2 D55 Hall Thruster Channel Simulations

The hydrodynamic simulations are performed to simulate the plasma discharge within the D55 for xenon propellant. The hydrodynamic model requires discharge voltage, discharge current, and mass flow rate as input parameters. In this research, we used experimental data measured at the University of Michigan [5]. The D55 thruster was operated at a flow rate of 4.76 mg/s of xenon, a discharge voltage of 300 V, and a current of 4.5 A. It is reported [66] that some portion of the plasma plume of a D55 thruster consists of doubly charged ions. In this research, the number fraction of double xenon ions is assumed to be 0.2 [82]. Keefer [83] obtained the Xe^+ axial velocity component using Laser Induced Fluorescence (LIF). We take 15,000 m/sec as the axial velocity of Xe^+ at the thruster exit center based on the measured data of Keefer.

From the relation of the plasma potential drop and the ion velocity at the thruster exit,

$$\Delta\phi = \frac{1}{2} m_i v_i^2 / e, \tag{4.2}$$

we calculate a plasma potential of 145 V at the thruster exit. However, this result is based on only a single charged ion. In the hydrodynamic model, we also consider double charged ions. If we use the mixed ion velocity

$$u = (n^+ u^+ + n^{2+} u^{2+})/(n^+ + n^{2+}), \tag{4.3}$$

and assuming

$$u^{2+} = \sqrt{2} u^+ \tag{4.4}$$

the mixed ion velocity is 16,200 m/sec. Then, from Eq (4.2) a plasma potential of 120 V at the thruster exit is obtained.

The one dimensional magnetic field approximation is used for this study. The running time for a simulation requires only a few minutes to reach a steady-state solution on a modern single processor desktop computer.

Our goal of this section is to obtain the plasma properties, especially the ion velocity, and ion number density profile at the channel exit with given initial conditions (mass flow rate of 4.76 mg/s, discharge voltage of 300 V, and discharge current of 4.5 A) and a thruster exit plasma potential of 120 V.

4.2.1 D55 Hall Thruster Channel Simulations with a Nozzle Exit

The geometry of the D55 thruster includes a 5 mm long channel with an inner radius of 25 mm and an outer radius of 30 mm. One of the characteristics of the D55 Hall thruster is a small nozzle-like geometry at the exit. This nozzle shape geometry is included in the simulation. For the simulations, the domain is divided into square cells with sides 0.18 mm long. This results in a mesh that contains 2187 cells. The

mesh represents an axisymmetric domain stretching from the anode to the exit plane, bounded by the inner and outer walls of the acceleration channel.

At the anode, a plasma number density of $1 \times 10^{17} m^{-3}$ and an ion velocity of 1000 m/s are assumed. It is reported that the electron temperature in the thruster channel of a TAL type thruster is relatively higher than that of a SPT type [17] [84]. In this study, an electron temperature profile is used, with a maximum of 28.5 eV at the exit and a half maximum at the anode based on Ref. [17]. A coefficient of 1/100 is used for the Bohm mobility term [61], while a coefficient of 0 is applied for the wall collision frequency because the D55 Hall thruster has conducting walls.

Contour plots of the plasma density and potential fields are shown in Figs. 4.11 and 4.12, respectively. The anode is on the left side of the figure, while the exit plane is at the right border. The white spaces above and below the channel in the figures represent the outer and inner walls, respectively, in relation to the channel domain. The plasma density field looks reasonable in Fig.4.11. However, in Fig.4.12, one can see that the plasma potential field is completely unreasonable. The plasma potential varies between -250,000 and 80,000 V. Moreover, the code crashed before it reached the steady state. Therefore, even though the plasma density looks reasonable, we can not believe this result. Unfortunately, for given measured data, the hydrodynamic model could not reach a steady state. We have tried different mesh size, initial ion velocity, initial plasma number density, Bohm coefficient, and electron temperature, but the hydrodynamic model did not reach a stable state and gave unreasonable results with every combination of these parameters. Table 4.1 shows a summary of the initial conditions we tried for the simulation (We used three profiles of the electron temperature described in Section 4.1, see Fig. 4.8. The electron temperature in Table 4.1 is the maximum temperature of each case).

This is an unexpected result, because originally the hydrodynamic code was developed to study erosion processes of Hall thrusters [63]. Therefore, the hydrodynamic

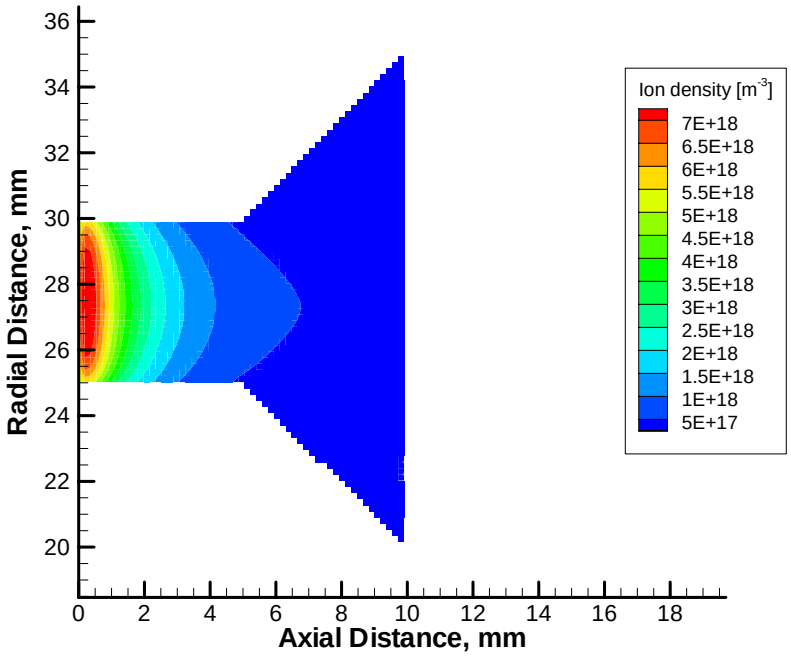

Figure 4.11: The simulated plasma density field for the D55 Hall thruster

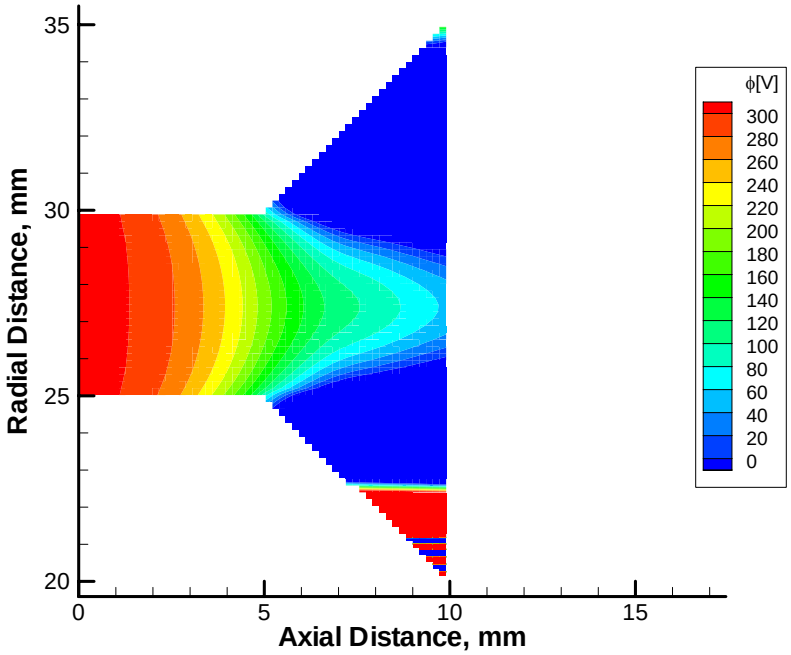

Figure 4.12: The simulated potential field for the D55 Hall thruster

number of cells	1,200	2,187	218,700	437,400			
initial ion velocity (m/sec)	0	1000	2000	3000	4000		
initial plasma density ($10^{16}m^{-3}$)	0	1	5	10	20	50	100
Bohm coefficient	16	30	60	80	100	120	
T_e (eV)	10	15	20	25	30	35	

Table 4.1: Initial condition sets.

code was expected to simulate a complicated geometry such as the D55 channel with a nozzle shape exit. However, our results show that the hydrodynamic code failed to simulate such a complex geometry. We also tried to simulate the plasma discharge with slowly increasing the nozzle angle similar to erosion processes. However, the code could not reach a steady state. One possible reason of this unexpected result is that the channel lengths and the potential gradients of the SPT and TAL thruster are different. Yim [63] investigated the 173Mv1 Hall thruster, a SPT type Hall thruster. The channel length is 38 mm and the potential drop is 150 V for the 173Mv1 Hall thruster, while the D55 has a 5 mm channel length and 180 V potential drop. Therefore, the D55 thruster has almost 1/8 times smaller channel length, and 8.5 times higher electric field. Another possible reason is the difference of the magnetic field between Yim's simulation and ours.

Since our simulation did not provide stable results, it indicates that further research is needed to improve the hydrodynamic model for modeling TAL thrusters.

4.2.2 D55 Hall Thruster Channel Simulation without the Nozzle Exit

The hydrodynamic model is now used to simulate the plasma discharge within the D55 Hall thruster where the nozzle shape domain is ignored and only the thruster channel domain is simulated. The mesh consists of 27×27 square cells 0.18 mm on a side. The geometry of the thruster includes a 5.0 mm long channel with an inner

radius of 25 mm and an outer radius of 30 mm. At the anode, a plasma number density of $1 \times 10^{17} m^{-3}$, an ion velocity of 1,000 m/s, and an electron temperature of 28.5 eV are assumed at the exit. We assume that the plasma potential at the thruster exit center is that at the nozzle exit center, 120 V. A coefficient of 1/100 is used for the Bohm mobility term, while a coefficient of 0 is applied for the wall collision frequency. These values allow for a stable solution of the hydrodynamic model, while providing reasonable values for the calculated potential drop.

Figure 4.13 shows contours of the plasma density. In Fig. 4.13, one can see that plasma density increases near the anode because of the ionization process and decreases because of the ion acceleration process through the exit.

Figure 4.14 presents contours of the plasma potential. The plasma potential is a maximum at the anode then decreases and has a minimum value at the channel exit center.

Figure 4.15 shows the axial variation of the neutral atom density along the channel center. The neutral atom density decreases as the flow convects downstream since neutrals are depleted by ionization.

Axial variation of the plasma density is shown in Fig. 4.16. It is clearly shown in Fig. 4.16 that the plasma density is increased from the anode to about 1 mm, after that the density is decreased. It means that the plasma ejection at the exit gives a dominant effect to decrease the plasma density, even though the ionization process occurs over the whole simulation domain.

Figure 4.17 presents the plasma potential variation along the channel center. One can see that the plasma potential is 300 V at the anode, and 120 V at the thruster exit.

The plasma potential along the radial direction at the thruster exit is shown in Fig. 4.18. In the D55 Hall thruster, the wall is connected to the cathode. So the potential at the walls (25 mm and 30 mm) are zero. One can see a small negative

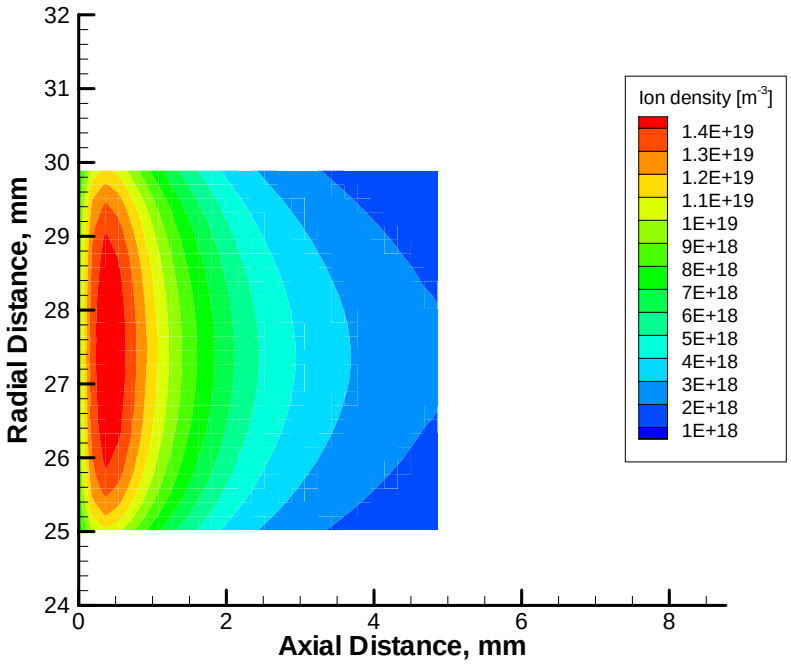

Figure 4.13: The simulated plasma density field for the D55 Hall thruster

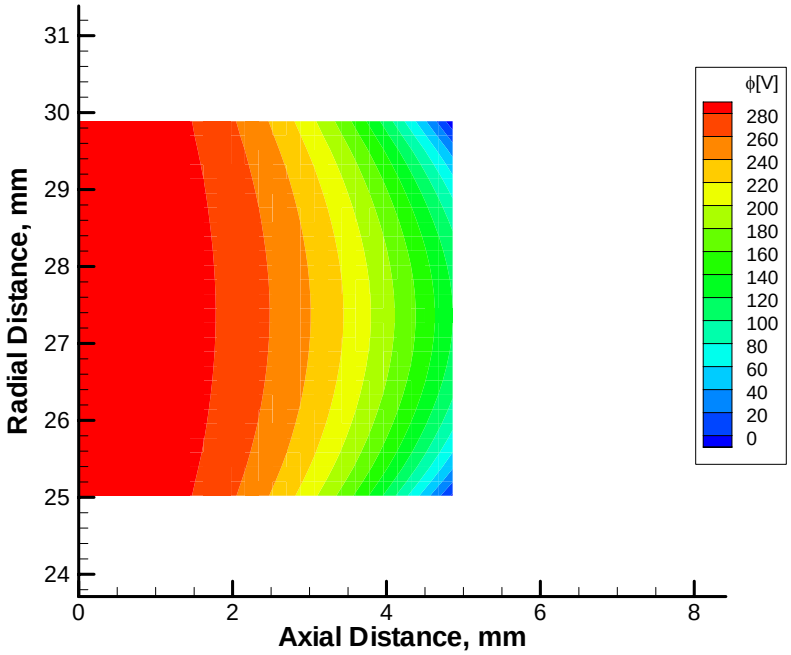

Figure 4.14: The simulated potential field for the D55 Hall thruster

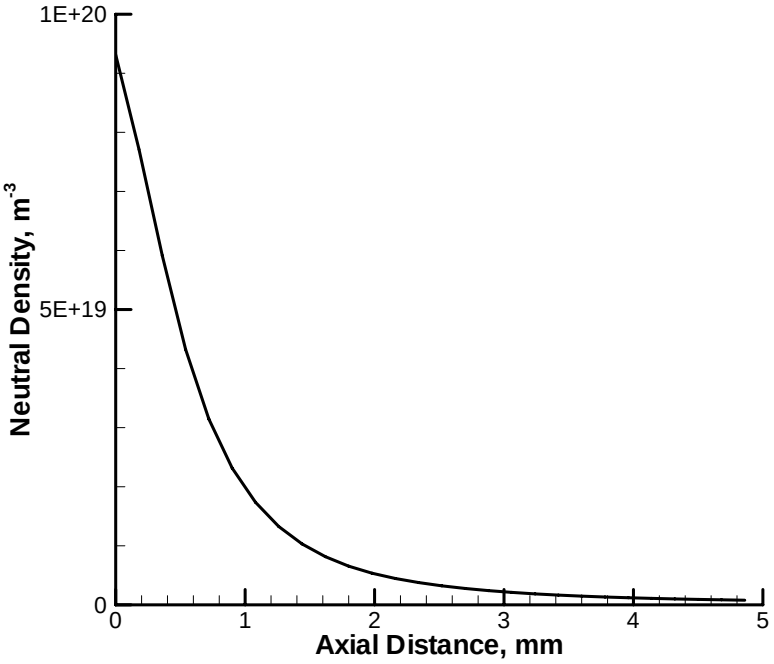

Figure 4.15: The neutral density along the channel center

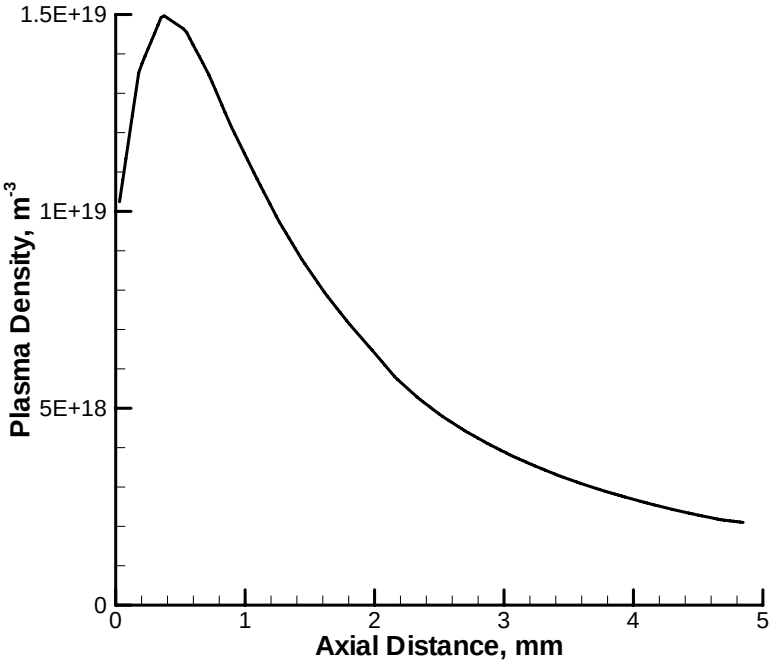

Figure 4.16: The plasma density along the channel center

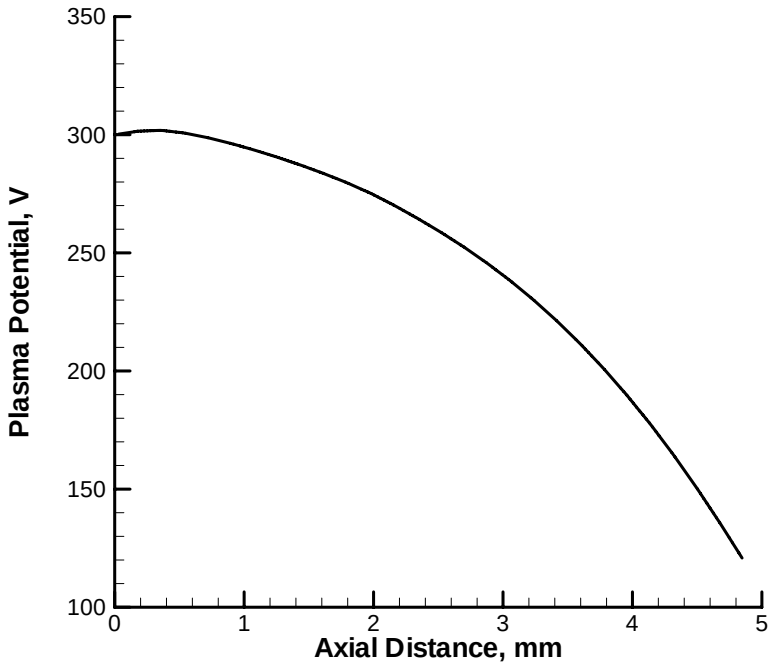

Figure 4.17: The plasma potential along the channel center

potential near both walls because of the sheath.

Figure 4.19 shows the axial velocity distribution along the radial direction at the thruster channel exit. Figure 4.19 shows that the ion axial velocity is minimum at the channel center. This feature is consistent with the potential variation shown in Fig. 4.18. In Fig. 4.18, the potential decreases from the center to the wall. The potential drop near the wall is greater than that at the channel center. Therefore, ion acceleration at the walls is greater than at the channel center. Figure 4.19 shows this potential variation effect.

Figure 4.20 shows the local flow angle variation along the radial direction at the channel exit. One can see that the angle varies almost linearly and increases from the center to the walls.

Figure 4.21 shows the plasma density variation along the radial direction at the channel exit. The plasma number density has a maximum at the channel center. This

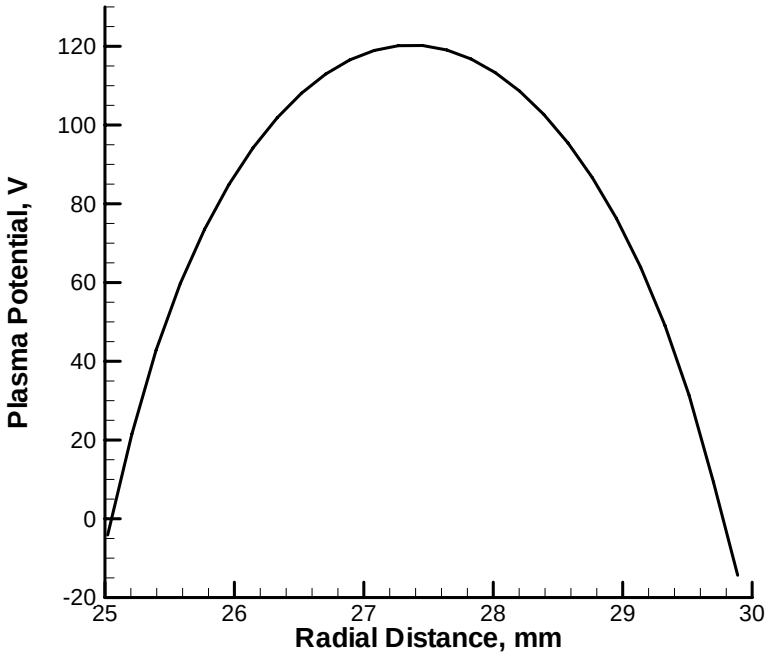

Figure 4.18: Plasma potential profile at the channel exit

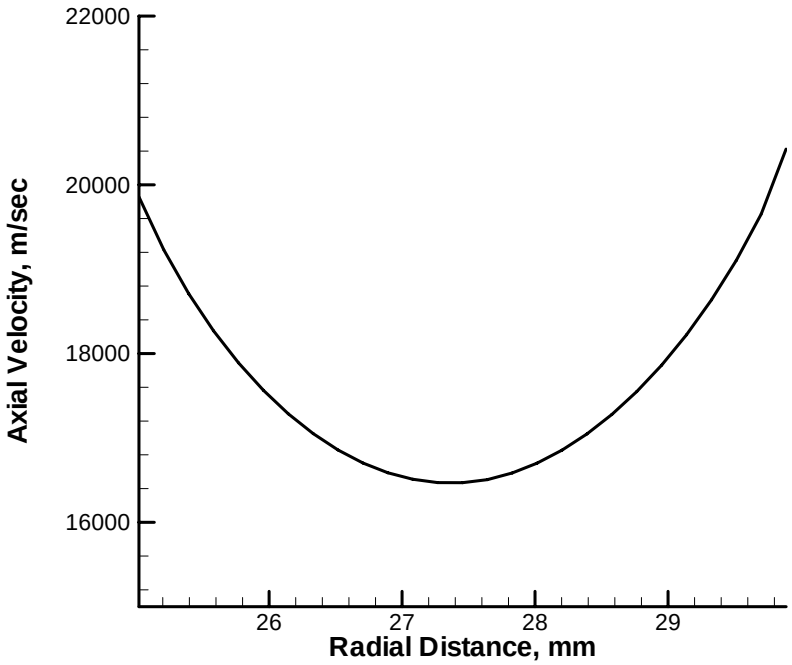

Figure 4.19: Axial velocity profile at the channel exit

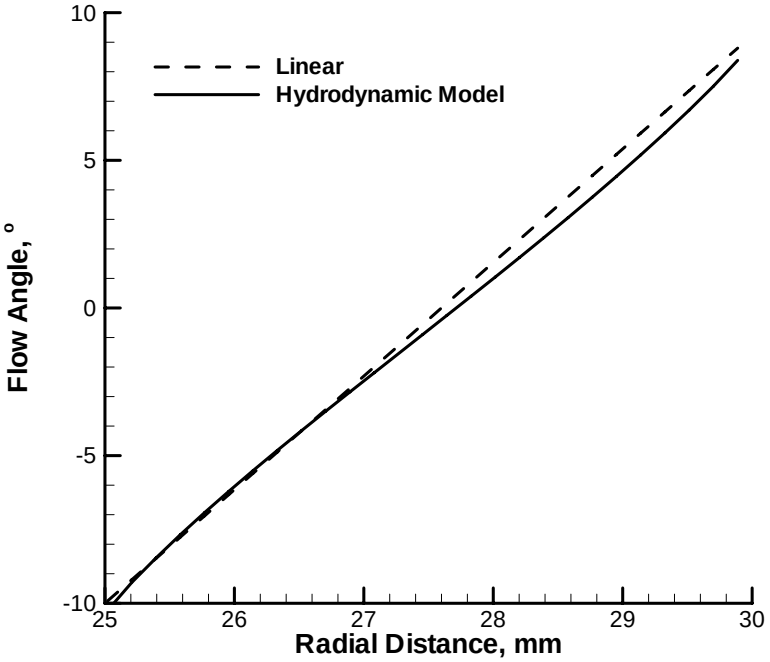

Figure 4.20: Flow angle profile at the channel exit

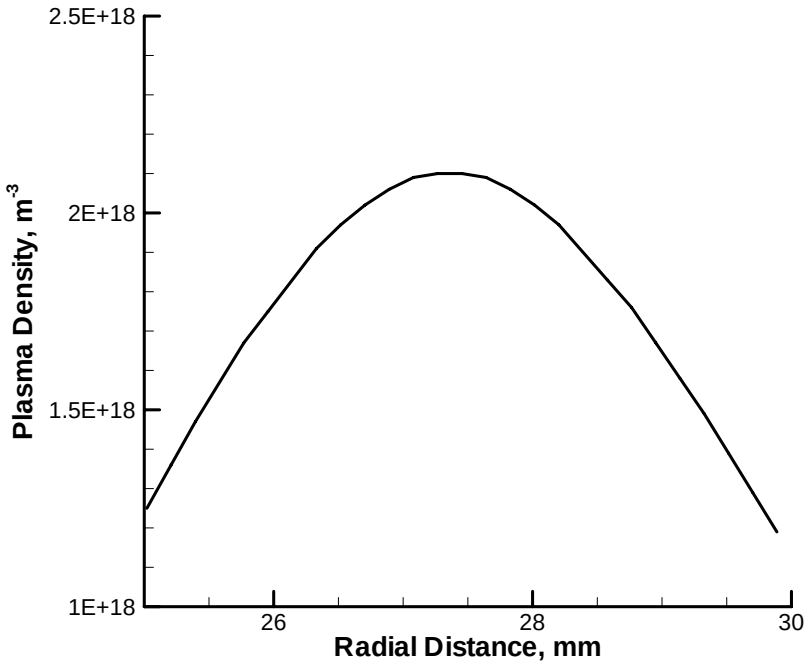

Figure 4.21: Plasma density profile at the channel exit

feature is consistent with the flow angle variation shown in Fig. 4.20. At the channel center where the flow angle is zero, flow convection in the radial direction is zero. Therefore the plasma density at the channel center is higher than at any other radial position where radial convection occurs.

4.3 D55 Hall Thruster Nozzle Exit Conditions

The ultimate goal of the hydrodynamic simulation in this study is to obtain the the plasma properties, especially the plasma potential, ion velocity, and ion number density profiles at the D55 Hall thruster nozzle exit. Unfortunately, the hydrodynamic model failed to simulate the complete domain of the D55 Hall thruster. Therefore, in this section, we estimate the nozzle exit boundary conditions using the hydrodynamic results for the channel along with measured thrust, current, mass flow rate, and ion velocity. The nozzle exit conditions are obtained by the following steps.

1. *Obtain the plasma properties at the thruster channel exit.* This step is performed by the hydrodynamic model.

2. *Estimate the ion current.* The discharge current from the thruster exit is 4.5 A [5]. However, some electrons emitted from the cathode provide charge neutrality in the plume and some flow into the thruster. Therefore, the ion current at the nozzle exit is less than 4.5 A. We assume that 0.25 A of the discharge current is due to electrons based on the measurement data in Ref. [5].

3. *Obtain the ion number density along the radial direction at the nozzle exit.* The nozzle exit area is three times larger than the channel exit. Therefore, we divide the channel exit ion number density value by three.

4. *Obtain the plasma potential at the edges of the nozzle.* In the D55 Hall thruster, the wall is connected to the cathode. Therefore, the potential at the walls (25

mm and 30 mm) are zero. We assume that the nozzle is also connected to the cathode and the potential at the nozzle edges is zero.

5. *Calculate the axial velocities and ion number densities of Xe^+ and Xe^{2+}.* Ion axial velocities and number densities are calculated based on the hydrodynamic results using the following equations

$$n^+ = 0.8 n_i \tag{4.5}$$

$$n^{2+} = 0.2 n_i \tag{4.6}$$

$$u^+ = \frac{u n_i - n^{2+} u^{2+}}{n^+} \tag{4.7}$$

$$u^{2+} = \sqrt{2} u^+ \tag{4.8}$$

where u is the mixed ion velocity, and n_i is the total ion number density.

6. *Set the plasma potential at the center of the nozzle exit.* In step 5, the ion velocity and number density of each species are calculated. Therefore, we do not have to use 120 V of potential anymore which is obtained from the mixed ion velocity. Based on the axial velocity measurement of Xe^+ in Ref. [83] which is 15,000 m/sec, the value of the plasma potential is set to 145 V by Eq.(4.2).

7. *Estimate the plasma potential along the radial direction at the nozzle exit.* We estimate the potential variation along the radial direction. There is no special rule for the estimation. However, the calculated mass flow rate, thrust, current based on the estimated potential should be the same as the measurement data. Therefore, this step is performed iteratively with the next three steps until the estimated properties and measurement data are matched well.

8. *Calculate the axial velocities of Xe^+ and Xe^{2+}.* Ion axial velocities are calcu-

lated based on the estimated plasma potential using the following equation

$$v_i = \sqrt{\frac{2e\Delta\phi}{m_i}}, \tag{4.9}$$

where $\Delta\phi$ is the potential difference between the discharge voltage (300 V in this study) and the estimated potential.

9. *Estimate the ion number density along the radial direction at the nozzle exit.* With step 7, and 8, the ion number density profile also should be adjusted to match measured flow rate, current, and thrust. As in step 7, there is no special rule for the estimation.

10. *Calculate the mass flow rate, thrust, and current based on the estimated ion axial velocities.* Steps 7 to 10 are performed iteratively until the calculated mass flow rate, thrust, and current match with the measured data.

Figure 4.22 shows the estimated plasma potential along the radial direction at the nozzle exit. One can see that the plasma potential is 145 V at the center and 0 V at the edges.

Figures 4.23 and 4.24 show the estimated Xe^+ number density and the axial velocity distribution of Xe^+ along the radial direction at the nozzle exit. Since we assumed that the number fraction of double xenon ions is 0.2, the Xe^{2+} number density is 4 times smaller than that of Xe^+. The axial velocity of Xe^{2+} is $\sqrt{2}$ times greater than that of Xe^+ from Eq.(4.9).

We also need to consider the flow divergence. As we mentioned for Fig. 4.20, the local flow angle varies almost linearly across the exit. Therefore, we assume divergence angles of $\theta_+ = 10^\circ$ for the outer edge, and $\theta_- = -10^\circ$ for the inner edge of the nozzle exit.

These estimated plasma properties, i.e., the plasma potential, ion number density, ion velocity, and flow divergence angle are used as boundary conditions for the plasma

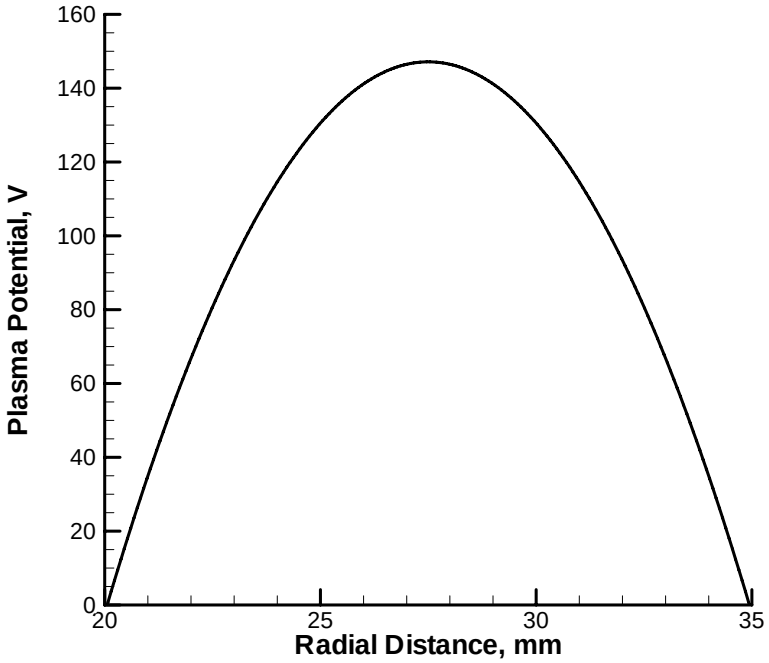

Figure 4.22: Plasma Potential profile at the nozzle exit

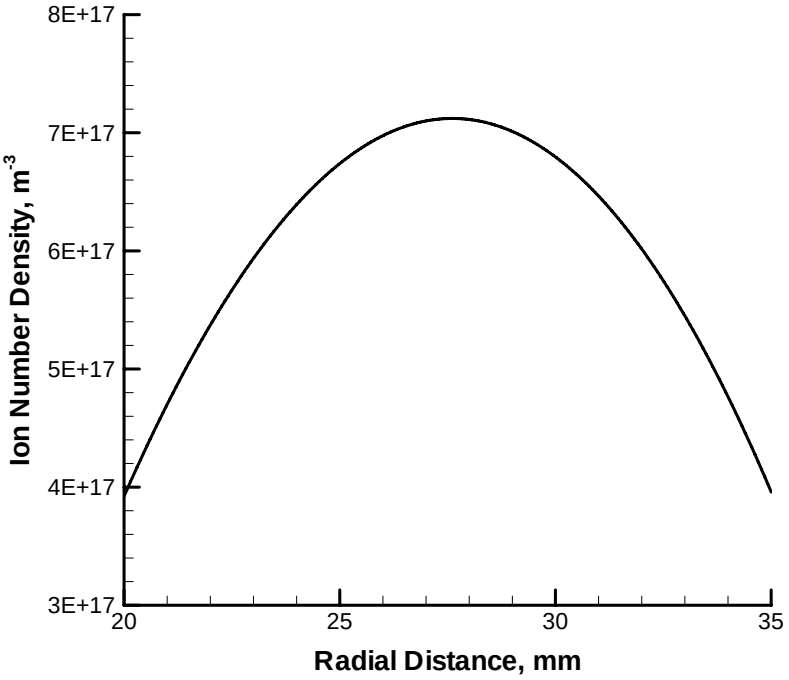

Figure 4.23: Xe^+ number density profile at the nozzle exit

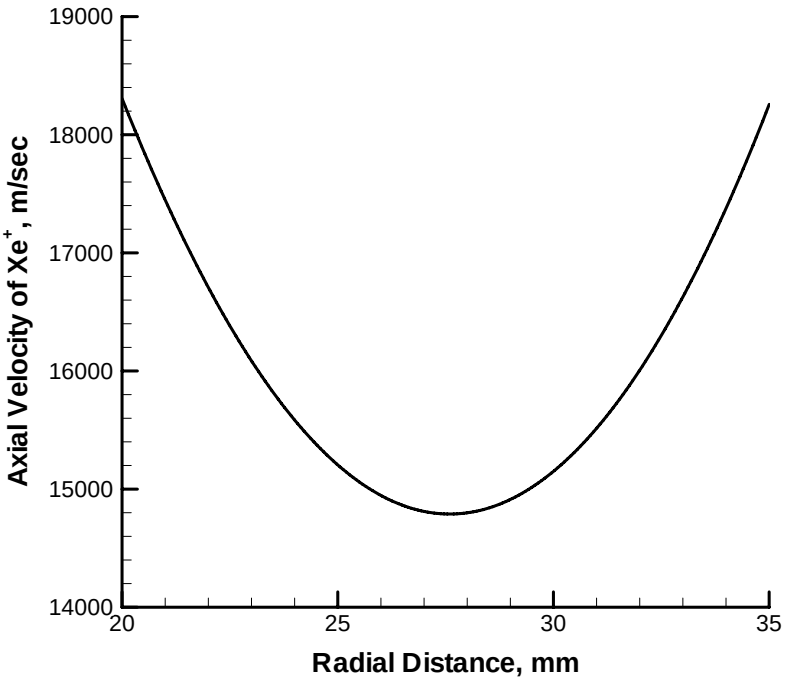

Figure 4.24: Axial velocity profile of Xe^+ at the nozzle exit

plume simulations in Chapter 5.

Recently it was shown that an important aspect of high-power TAL is the sheath formation near the channel wall [84]. Typically in a TAL, the channel walls are set equal to the cathode potential. This leads to a significant potential drop between the wall and the plasma. As a result, a high-voltage space charge sheath is formed, and the sheath thickness can be comparable to the channel width. In such a case, the charge neutrality assumption, one of the main assumptions of the hydrodynamic model, is violated. The sheath thickness can be estimated according to the Child-Langmuir law [85] [86]

$$s = \left(\frac{4}{9}\epsilon\right)\left(\frac{2e}{m_i}\right)\frac{\phi_s^{3/4}}{(eZ_iN_sV_s)^{1/2}} \tag{4.10}$$

where V_s is the ion velocity at the sheath edge, ϕ_s is the voltage across the sheath, s is the sheath thickness, ϵ is the permittivity of vacuum, N_s is the plasma density

at the sheath edge, Z_i is the ion mean charge, and m_i is the ion mass. With the plasma properties of the D55 Hall thruster, the maximum sheath thickness is only $\sim 8 \times 10^{-3}$ mm. Therefore, we expect that the sheath effect will not strongly influence the calculation of the initial conditions at the exit.

4.4 Summary

The discharge voltage (V) and current (I) characteristic of the D55 Hall thruster was studied. A special value of the Bohm coefficient gives good agreement with one experimental data point. This implies that perfect agreement with all measured valued could be obtained by more variation of the Bohm coefficient.

Also, the hydrodynamic model was used to simulate the plasma flow within the D55 Hall thruster. This analysis was performed to determine the plasma properties at the channel exit. It was found that the hydrodynamic model is very sensitive, and failed to simulate the complete domain of the D55 Hall thruster. However, the model successfully calculated the channel domain of the D55 Hall thruster. The results showed that, at the thruster exit, the plasma density has a maximum value while the ion velocity has a minimum at the channel center. Also, the results showed that the flow angle varies almost linearly across the exit and increases from the center to the walls.

Finally, the hydrodynamic model results are used to estimate the plasma properties at the thruster nozzle exit. The estimations are performed by an iterative method.

CHAPTER 5

PARTICLE SIMULATIONS OF PLASMA PLUME FLOW FROM THE D55 THRUSTER WITH ANODE LAYER

5.1 Introduction

Hall thrusters are highly efficient electric propulsion devices widely used on spacecraft for primary propulsion and on-orbit applications such as station keeping [9]. Hall thrusters are increasingly replacing chemical thrusters because they can create a higher specific impulse, obtain electricity input directly in space through solar cells, and do not require carrying oxidizers [1] [3]. Due to improvements in solar cell technology and renewed interest in nuclear power, high power electric propulsion system are being investigated. One of the most important fields of these investigations is the study of plasma plumes.

A plasma plume is a complex rarefied flow with several species: atoms, positively charged ions and negatively charged electrons. Modeling of the plume fields of Hall thrusters yields important information about the plume impingement on a spacecraft and about complex plasma processes inside the thruster. First, it provides an understanding of the plume impingement that involves fluxes of high-energy ions and charge-exchange (CEX) particles onto sensitive spacecraft devices such as solar arrays. When a fast ion collides with a slow neutral atom, one or two electrons may transfer from the neutral atom to the ion, resulting in a slow ion and a fast neutral atom. Under the influence of the electric field, this ion may drift behind the thruster.

Severe impingement of ions onto spacecraft surfaces may eventually result in the failure of devices or even the failure of an entire mission. For example, the ions emitted from Hall thrusters have 0∼400 eV of energy, while aluminum, a common material of spacecraft surfaces, has a sputter yield threshold of 68 eV [87]. If severe impingement can be predicted, however, a change of design philosophy can be considered to reduce the impingement. Second, plume modeling may also help to clarify the complex plasma processes inside the thruster. Understanding these processes can help designers to improve propulsion performance. The near field plume of a Hall thruster is a very important region. The relatively high plasma density in the near field facilitates the use of a variety of experimental diagnostic techniques from probes to nonintrusive optical methods such as laser induced fluorescence (LIF). Such techniques are much more difficult to apply either in the internal thruster flow or in the plume far field. In the internal thruster flow, a probe may disturb the flow itself, therefore the measured data may be affected. In the far field, the plasma number density is too small to use some experimental diagnostic techniques such as LIF. Therefore, modeling the behavior of the thruster plume in these fields is a critical aspect in the design of thrusters and their integration on spacecraft.

Accurate simulation of the plasma plumes from Hall thrusters requires an accurate modeling of the complex physical plume mechanism. This thesis provides the computational simulation of plasma plume flows into a vacuum using a hybrid particle-fluid approach. This approach provides accurate physical results with relatively low cost. For more discussion of computational modeling, see Section 1.7.

The direct simulation Monte Carlo (DSMC) method [26] models the collisions of the heavy particles (ions and atoms) while the Particle In Cell (PIC) method [35] models the transport of the ions in electric fields. The electrons are modeled using a fluid description because the electron collision frequency is almost one hundred times higher than the ion collision frequency.

For the fluid electron model, the Boltzmann relation, Equation (2.7), is usually adopted to compute the plasma potential. The Boltzmann relation requires that the electrons be collisionless, isothermal, and un-magnetized. A recently proposed detailed fluid electron model by Boyd and Yim [19] based on the conservation laws for electrons is capable of providing accurate and detailed distributions for electron temperature, plasma potential, and electron velocity stream functions. This model was successfully applied in a simulation of an axisymmetric plasma plume firing from a 200 W class Hall thruster [1]. We expanded this model to analyze the possible influence of the magnetic field on the plasma plume. This model was briefly discussed in Chapter 2.

In this study, axisymmetric plasma plumes from the D55 TAL Hall thruster are simulated with the DSMC-PIC method. Hall thrusters are nominally axisymmetric. Therefore, an axisymmetric numerical model should be sufficient to reproduce most features observed in the laboratory. Here, we model two dimensions in space, the R (radial) and Z (axial) directions. The axisymmetric plume flow fields from the D55 TAL Hall thruster are investigated using MONACO-PIC [1] [52], a hybrid PIC-DSMC code developed at the University of Michigan that contains both the *Boltzmann model* and the *Detailed model*. The simulations are performed on unstructured meshes with parallel processing.

It is significant to mention that in the literature there are no other studies that have reported any similar work with such a detailed treatment. Experimental measurements of the near-field plasma plume from Hall thrusters show that the magnetic field leaks into the plume and is strong enough to affect the electron motion in the near-field plume region [4] [5]. However, among the rare reports of simulations for plume flows from a TAL, very few considered magnetic field effects. In the past, Keidar et al. [18] performed quasi one dimensional fully fluid simulations of the plasma plume from the D55 TAL thruster and indicated that the plasma potential slightly

increases with axial distance from the thruster exit plane at the near-field and decreases in the far-field. Keidar et al. adopted the *Boltzmann model* as the fluid electron model. Taccogna et al. [21] performed axisymmetric hybrid simulations of the plasma plume from the SPT-100 without assuming quasi-neutrality and reported that the plasma potential increases with axial distance at the very-near-field.

Section 5.2 briefly introduces background information from experiments. Section 5.3 reviews the boundary conditions for our simulations. Finally, Section 5.4 presents general features of the numerical 2D axisymmetric simulation results and a comparison of these results with experimental data taken in the plume of the D55.

5.2 Background

The thruster considered in this research is the D55 TAL Hall thruster developed by TsNIIMASH. A schematic of the D55 TAL thruster is presented in Figure 5.1. The D55 thruster has an annular exhaust aperture with a mean diameter of 55 mm and a width of 5 mm with a small nozzle-like geometry at the exit. The D55 has nominal discharge operating conditions of 300 V and 4.5 A (1.35 kW) with xenon as its primary propellant. The '55' indicates the mean diameter of the anode in millimeters. We have chosen to study the D55 Hall thruster because of the availability of a significant amount of experimental data for this device. A more complete description of the D55 can be found in [88].

Figure 5.2 shows contours of the radial component of the magnetic field outside of the thruster which are reconstructed using experimental data [5]. Because of the proprietary nature of the magnetic field data, the values reported in this research have been normalized to the maximum value. Experimental investigation of the magnetic field distribution near a Hall thruster shows that the magnetic field has both radial and axial components of which the radial component is much larger [5]. Thus for simplicity, only the radial component of the magnetic field is considered in this study.

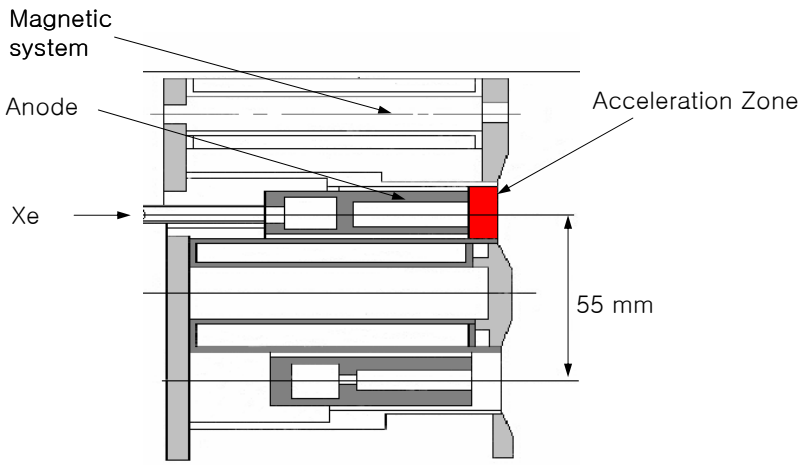

Figure 5.1: Schematic of the D55 Hall thruster

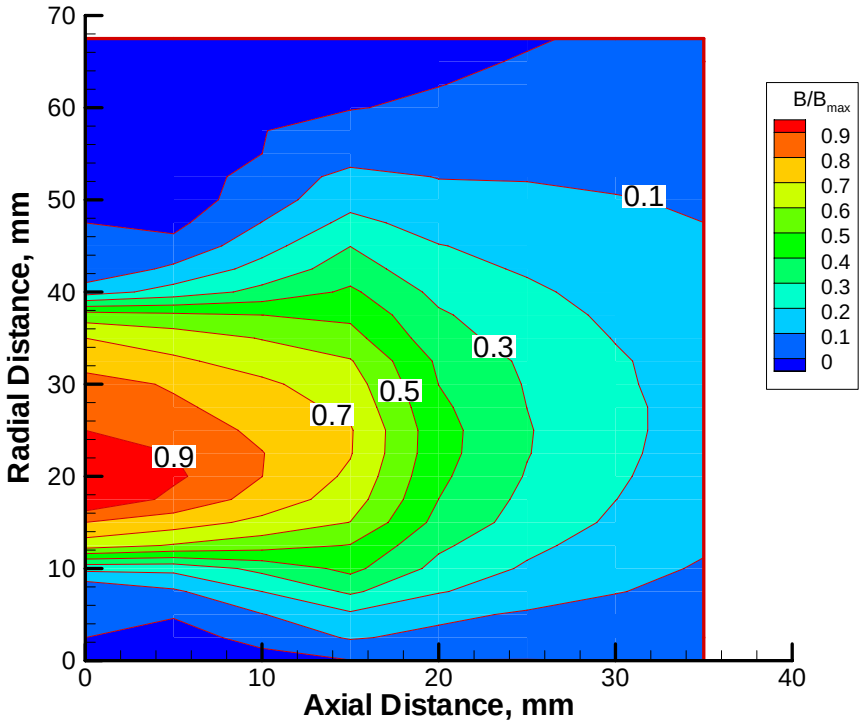

Figure 5.2: Magnetic field profiles

We also assume that the magnetic field strength is zero outside the area shown in Fig. 5.2.

We consider three thruster operating conditions corresponding to three different experiments. Most of the results presented here are for a series of experiments conducted at the University of Michigan [5] [89]. The D55 thruster was operated at a flow rate of 4.76 mg/s of xenon, a discharge voltage of 300 V, and a discharge current of 4.5 A. The specific impulse under these conditions was previously measured to be 1,810s [90]. The backpressure in the Michigan facility is reported as 8.3×10^{-3} Pa.

The second flow condition investigated corresponds to a study performed by TsNIIMASH [91]. The thruster was operated at a flow rate of 3.5 mg/s, a discharge voltage of 300 V and a discharge current of 3 A. The background pressure with the thruster running was 5.9×10^{-3} Pa.

The third flow condition corresponds to a study performed by the University of Tennessee Space Institute (UTSI) and Lockheed Martin Astronautics (LMA) [83]. The thruster was operated at a flow rate of 6 mg/s, a discharge voltage of 300 V and a discharge current of 4.5 A. The background pressure with the thruster running was 9.3×10^{-3} Pa. It is reported [66] that some portion of the plasma plume of the D55 thruster consists of doubly charged ions. In this research, the number fraction of double xenon ions is assumed to be 0.2.

In operation of the thruster, gaseous xenon effuses from the upstream end of the acceleration channel. Some of the xenon atoms are ionized and then accelerated by the imposed electric field in the rest of the acceleration channel. A current of electrons is emitted from the cathode. One fraction of these electrons is accelerated while traveling across the electric field towards the anode and is trapped in an annular Hall current by the magnetic field. The electrons' high kinetic energy ionizes a fraction of the xenon atoms, and eventually, these electrons are depleted at the thruster anode. The rest of the electrons emitted from the cathode travel downstream into the plume

to provide charge neutrality.

Xenon is usually employed as the propellant in Hall thrusters. A plume from a plasma thruster consists of light electrons with thermal speeds of 1×10^6 m/s, heavier ions or neutral atoms, such as fast single or double charged ions, Xe^+, Xe^{2+}, slow neutral xenon, fast neutral xenon, and slow ions due to CEX.

5.3 Boundary Conditions

Several macroscopic properties of the plasma must be obtained to define boundary conditions for the simulations. For the *Boltzmann model*, the plasma potential is required for all boundaries. For the *Detailed model*, the plasma potential, the electron stream function, and the electron temperature are required for all boundaries.

An essential requirement for the electron steam functions at the thruster exit and the cathode exit is the specification of two Neumann boundary conditions: $\frac{\partial \Psi}{\partial n} = \frac{J_a}{e} = 1.57 \times 10^{21}/m^2/sec$ and $\frac{\partial \Psi}{\partial n} = \frac{J_c}{e} = -2.86 \times 10^{22}/m^2/sec$. These conditions are obtained based on the discharge current, and the areas of the thruster exit and the cathode exit.

The sheath voltage is another boundary condition we need to obtain. When an ion particle hits a wall of the thruster or chamber, it loses its charge and reflects diffusely as a neutral particle with a thermal velocity that is characterized by the wall temperature. The D55 TAL thruster has metal walls. Further, the sheath voltage at the thruster walls is significant. We can estimate this voltage using a transformation of Equation (2.15):

$$\phi_w = \phi_0 + \left(\frac{\overrightarrow{j}}{\sigma} - \frac{k \bigtriangledown (n_e T_e)}{e n_e} \right) \cdot d\overrightarrow{l}, \tag{5.1}$$

where ϕ_0 is the potential at the node next to the wall. The gradient of electron temperature is set to zero at each wall.

For all heavy species, we also need to define the boundary conditions at the thruster exit. Specifically, we need to define the number density, velocity and tem-

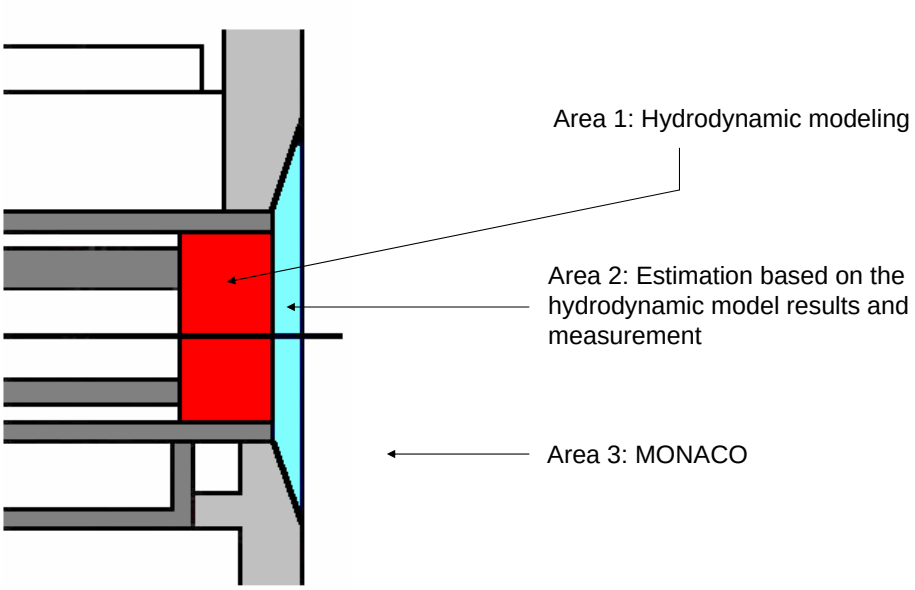

Figure 5.3: Methods for calculation of boundary conditions at the nozzle

perature. For number density and velocity, we use the hydrodynamic model results described in Section 4.3. Figure 5.3 illustrates the methods for each area:

1. Thruster channel area: Simulate the plasma with the hydrodynamic code and calculate the plasma properties at the channel exit.

2. Area from the channel exit to the nozzle exit: Estimate the plasma properties based on the hydrodynamic results and the experimental data for the mass flow rate from the anode and cathode, the thrust, and the discharge current. Calculate the plasma potential, ion number density and ion velocity, as well as the neutral atom number density and velocity.

3. Area outside of the thruster: Simulate the plasma plume with MONACO-PIC using the nozzle exit conditions as thruster exit initial conditions.

The thruster and cathode wall temperature are set to 300 K, similar to the condition in Ref. [82]. The electron temperature at the thruster exit is set to 10 eV

in the *Boltzmann model* and 20 eV in the *Detailed model* to obtain good agreement between the simulations and the data measured in the near field. In the *Boltzmann model*, the electron temperature is constant over the entire domain. Also, the electron temperature is set to 1.5 eV at the outflow boundary in the *Detailed model* to obtain good agreement between the simulations and the data measured in the far field. The electron temperature at the cathode is set to 2 eV according to the measurement [92]. At the thruster wall, the electron temperature is set to 1 eV, similar to the condition in Ref. [81]. At the thruster exit, the temperature of ions is assumed to be 4 eV, and that of the neutral atoms is assumed to be 750 K, similar to the condition in Ref. [82]. We also need to consider the flow divergence. From the hydrodynamic model simulation results in Section 4.3, it is found that the angle varies almost linearly across the thruster exit. Therefore, we assume divergence angles of $\theta_+ = 10^\circ$ for the outer edge, and $\theta_- = -10^\circ$ for the inner edges of the nozzle exit based on the hydrodynamic simulation results in Section 4.3. In the *Detailed model*, the external cathode of the Hall thruster can be modeled. While the actual cathode provides essentially a point source of electrons that therefore involves a three dimensional flow, in the present study it is modeled within the axially symmetric framework of the code. This is not a bad assumption given the high mobility of the electrons that rapidly forms a symmetric flow field. We assume that only electrons are emitted from the cathode.

The plasma potential is set to 2.0 V at the outflow boundary to obtain a good agreement between the simulations and the data measured in the far field.

Figures 5.4 and 5.5 show the boundary conditions for the *Boltzmann model* and the *Detailed model*, respectively. Tables 5.1 and 5.2 summarize the boundary conditions for the stream function, the plasma potential, and the electron temperature for both models.

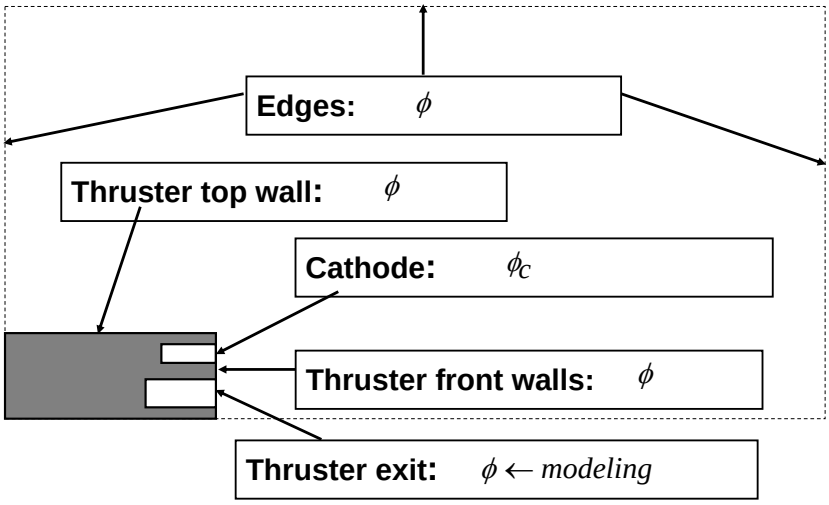

Figure 5.4: Boundary conditions of the *Boltzmann model*

Boundary	Outflow	Wall	Thruster Exit	Cathode	Symmetric Plane
$\phi(V)$	2.0	0.0	modeling	14.0	$\frac{\partial \phi}{\partial n} = 0$
$\Psi(m^{-1}s^{-1})$	N/A	N/A	N/A	N/A	N/A
Te(eV)	10	10	10	10	10

Table 5.1: Boundary Conditions for the Boltzmann Electron Fluid Model.

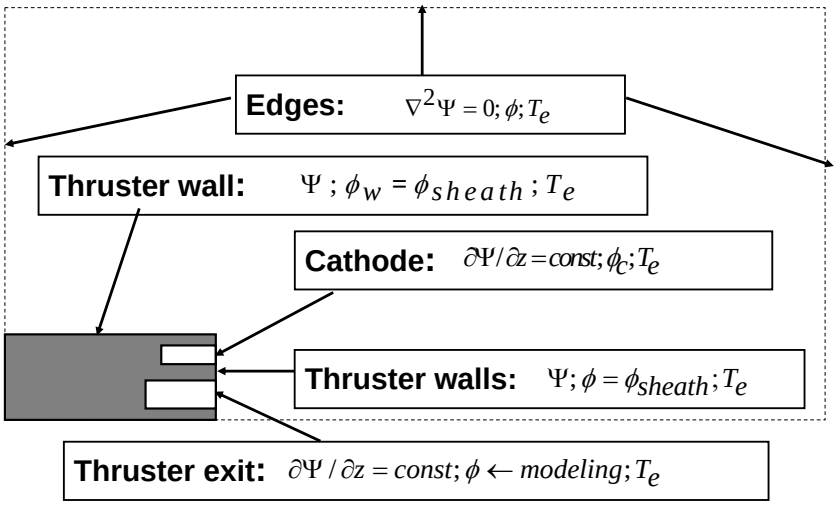

Figure 5.5: Boundary conditions of the *Detailed model*

Boundary	Outflow	Wall	Thruster Exit	Cathode	Symmetric Plane
$\phi(V)$	2.0	2.0	modeling	14	$\frac{\partial \phi}{\partial n} = 0$
$\Psi(m^{-1}s^{-1})$	$\frac{\partial^2 \Psi}{\partial n^2} = 0$	0	$\frac{\partial \Psi}{\partial n} = 1.57 \times 10^{21}$	$\frac{\partial \Psi}{\partial n} = -2.86 \times 10^{21}$	$\frac{\partial \Psi}{\partial n} = 0$
Te(eV)	1.5	1.0	modeling	2.0	$\frac{\partial Te}{\partial n} = 0$

Table 5.2: Boundary Conditions for the Detailed Electron Fluid Model.

5.4 Simulations and Results

DSMC-PIC particle simulations are performed to simulate the plume flows measurement of the University of Michigan [5] [89], TsNIIMASH [91], and UTSI & LMA [83]. The finite element solver is called every 10 time steps for Equations (2.8), (2.17), (2.18). The computational grid employed in the present study consists of triangular cells in which the number of cells is 10,621. A more detailed discussion about the unstructured mesh is in Section 5.4.1. The smallest cells are located close to the thruster exit and have a size of 2.5 mm. The largest cells are those close to the edges of the domain and have a size of 25 mm. To compare the simulations and the data measured in the far field, the domain is extended to 1.05 m axially and 0.57 m radially. The simulations take 60,000 time steps to reach a steady stage and another 20,000 time steps for sampling. The time step is set to 7.0×10^{-8} sec. With this time step, a Xe^{+} particle needs at least two time steps to cross the smallest cell. About 5 million particles are used for the simulations. The range of particles per cell is 90$\sim$1400. The simulations are performed with 8 processors on NYX, the computing system of the Center for Advanced Computing of the University of Michigan. The total running time is about 12 and 20 hours of CPU time for the *Boltzmann* and the *Detailed models*, respectively.

5.4.1 Structured mesh vs. Unstructured mesh

The near field plume is a very active and complicated area. Therefore, a fine resolution mesh is needed to investigate the near field plume. However, if we use a structured mesh, the mesh size in the far-field is too small to have enough particles per cell to obtain the correct plasma potential. Figure 5.6 shows a structured mesh in which the total number of cells is 12,248. The mesh is generated with the software Hypermesh [93]. The smallest cells are located close to the thruster exit and have a size of 2.5 mm. The largest cells are those close to the edges of the domain and

have a size of 10 mm. Figure 5.7 shows the plasma potential results of the *Boltzmann model* calculated with the structured mesh. About 0.5 million particles are used for the simulation. One can see that there are long tails at 90 V and 100 V near the symmetric line. The reason of these long tails is that the grid size is so small that the number of particles is not enough to calculate the correct potential. To solve this problem, the grid size should be larger. However, we also need a fine grid near the thruster exit. There is no way to satisfy both conditions using a structured mesh.

The solution is an unstructured mesh. Figures 5.8 shows the unstructured mesh which is used in this study. The mesh is also generated with the software Hypermesh [93]. This unstructured mesh has a smaller number of cells, and even coarser cells than those of the structured mesh for cells close to the edges of the domain. However, Figure 5.9 shows that the incorrect tails near the axis have disappeared in the solution obtained with the unstructured mesh. About 0.5 million particles are used for the simulation. There is still some fluctuation at the 90V line near the z axis, but this small fluctuation can be removed by increasing the number of particles. Therefore, we use an unstructured mesh in this study.

5.4.2 Parallel Benchmarks

In this research, parallelized implementation of MONACO-PIC code is achieved through domain decomposition for axially symmetric flows. Each parallel task is assigned a number of cells and performs all operations on every particle residing in these cells. Communication between tasks occurs when particles cross boundaries between domains and are thus transferred between tasks. The parallel decomposition is specified by using the Metis package [94]. Metis uses multilevel partitioning algorithms. These algorithms reduce the size of the graph by collapsing vertices and edges, partition the smaller graph, and then uncoarsen it to construct a partition for the original graph. To confirm the validity of the parallel implementation, an axisymmetric

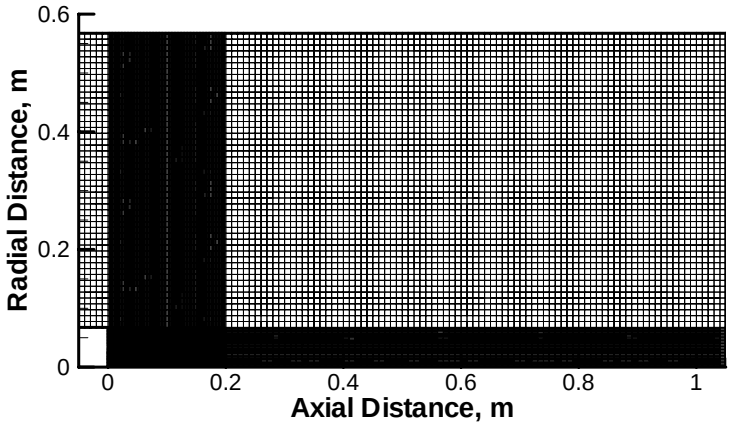

Figure 5.6: A structured mesh domain

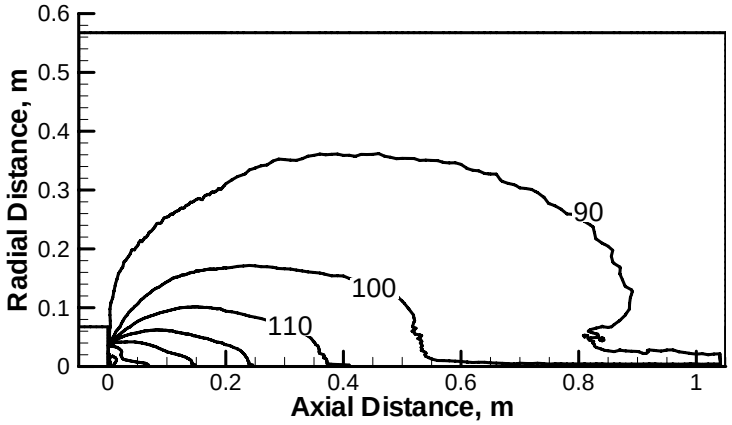

Figure 5.7: Contours of plasma potential (in V), structured mesh results

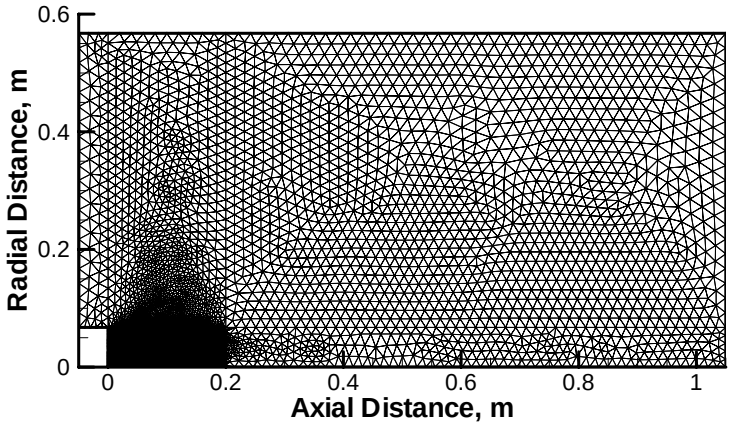

Figure 5.8: An unstructured mesh domain

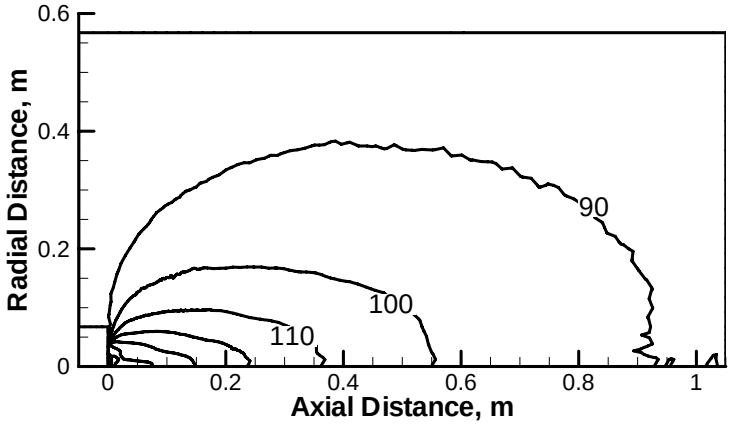

Figure 5.9: Contours of plasma potential (in V), unstructured mesh results

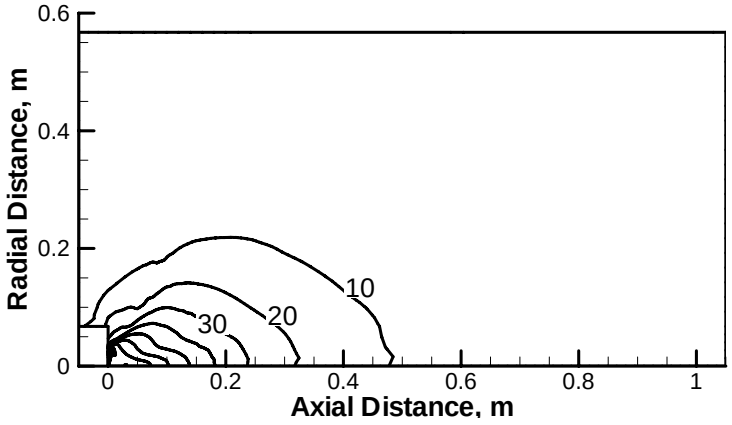

Figure 5.10: Contours of plasma potential (in V), serial simulation

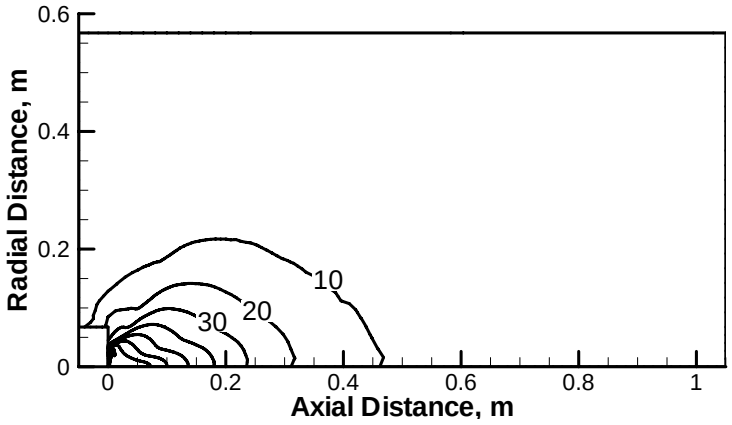

Figure 5.11: Contours of plasma potential (in V), parallel simulation

parallel simulation of the plasma plume flow from the D55 Hall thruster is performed and the results are compared with serial simulation results. Figures 5.10, 5.11, 5.12, 5.13, and 5.14 are comparisons of the plasma potential, ion current density, and the ion axial velocity of the *Detailed model*. All of the results show almost identical behavior from the serial and parallel simulations.

To acess the parallel efficiency of MONACO-PIC, two types of speedup test are performed. In case 1, about 5 million particles are used for the simulations regardless of the number of processors. In case 2, about 1 million particles per processor are used for the simulations. Each simulation covers 1,000 timesteps. The parallel efficiency

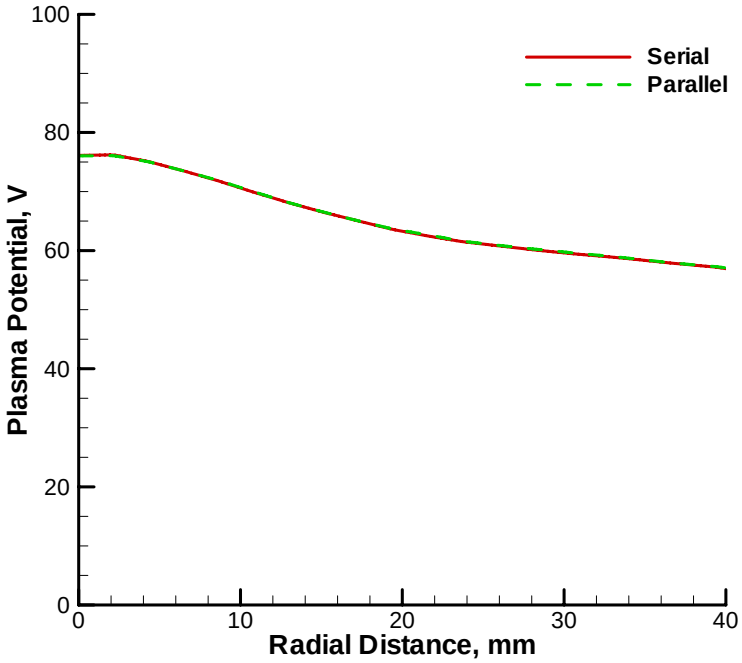

Figure 5.12: Comparison of plasma potential, 50 mm from the thruster exit plane

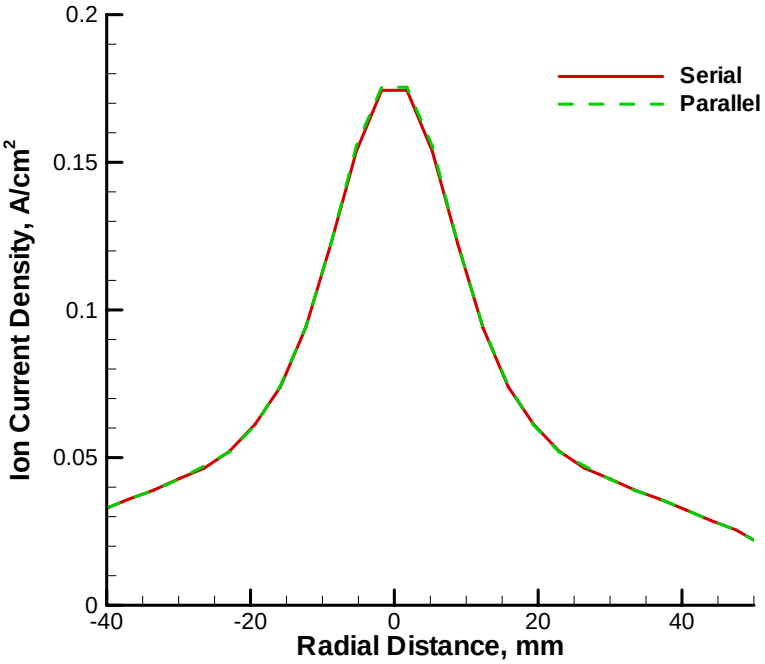

Figure 5.13: Comparison of ion current density, 40 mm from the thruster exit plane

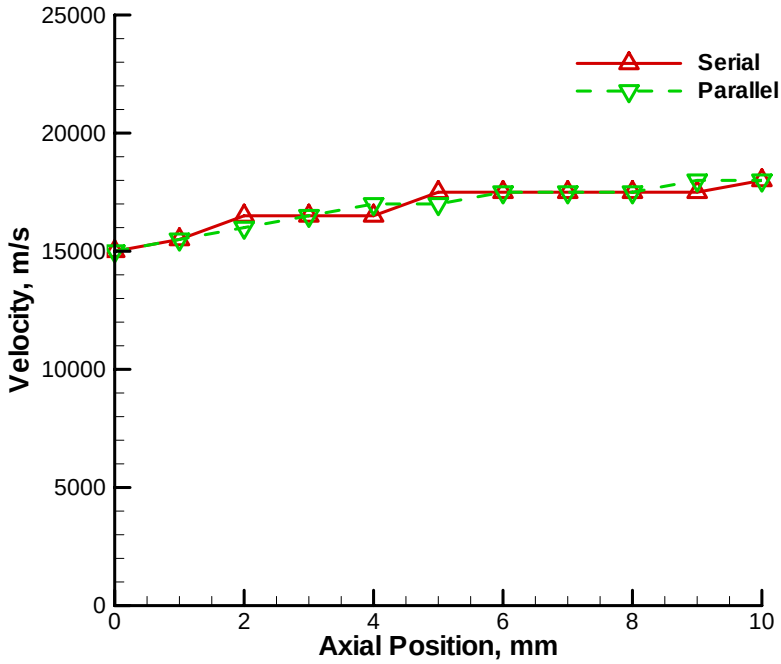

Figure 5.14: Comparison of ion axial velocity at a radial position of 27.5 mm

of MONACO-PIC is shown in Figure 5.15. One can see that case 2 shows better efficiency than case 1 when the number of processors is greater than 8. The reason of inefficiency in parallel computing results from message passing. When the number of particles per processor is small, the message passing process takes more time than the calculation process, and results in the low efficiency. If the number of particles per processor is large enough, then the message passing process takes relatively less time than the calculation process, and the efficiency increases. However, the parallel efficiency is still rather low for both cases. Seeking a more effective solution to reduce the message passing will improve the parallel performance of the code.

5.4.3 Plasma Potential

Overall plasma potential fields obtained with the *Boltzmann model* and the *Detailed model* are presented in Figs. 5.16, 5.17, and 5.18. Figure 5.16 shows the *Boltzmann model* results. Figures 5.17 and 5.18 show the *Detailed model* results obtained without

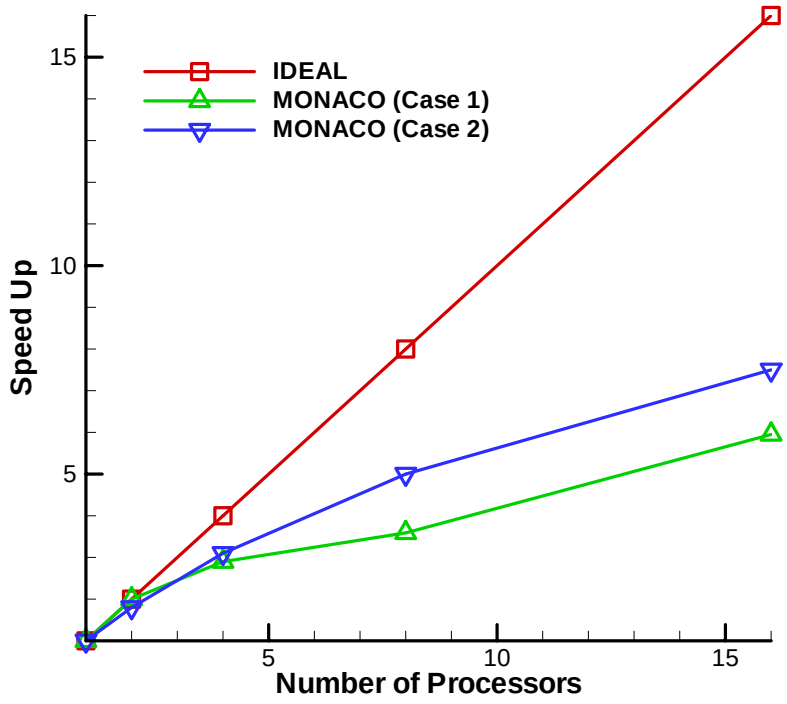

Figure 5.15: Parallel efficiency of MONACO-PIC

and with the magnetic field, respectively. It was reported for the BHT-200 that the plasma potential gradient of the *Boltzmann model* and the *Detailed model* are very different [19]. From Figs. 5.16 and 5.17, we can see this feature. The *Boltzmann* relation is

$$\phi = \phi_{ref} + \frac{kT_{ref}}{e} \log\left(\frac{n_e}{n_{ref}}\right) \tag{5.2}$$

From Eq. (5.2), the plasma potential in the *Boltzmann model* is calculated according to the logarithmic difference of the electron number densities. Therefore, even if the gradient of the electron number density is strong, this gradient does not give much effect on the plasma potential. The *Detailed model* includes a more accurate fluid description of the electrons based on their continuity, momentum and energy equations. Therefore, we expect that the plasma potential prediction of the *Detailed model* is more correct. From Figs. 5.17 and 5.18, one can see that when the magnetic field is considered, the plasma potential gradients become stronger. It is expected that

only electrons are magnetized while ions do not feel any significant effects from the magnetic field. However, plasma flow across the magnetic field under this condition generates additional electric fields which act to increase the total fields. One possible explanation for the trends observed is the confinement of the electron motion by the magnetic field. If the magnetic field is ignored, a generalized Ohm's law is

$$\overrightarrow{j} = \sigma[-\nabla\phi + \frac{1}{en_e}\nabla(n_e k T_e)] \tag{5.3}$$

However, if the magnetic field is considered, then an additional term $\overrightarrow{V_e} \times \overrightarrow{B}$ appears on the right hand side of Eq. (5.3), and a generalized Ohm's law is

$$\overrightarrow{j} = \sigma[-\nabla\phi + \overrightarrow{V_e} \times \overrightarrow{B} + \frac{1}{en_e}\nabla(n_e k T_e)] \tag{5.4}$$

Therefore, for a given current density, if the magnetic field is considered the electrical conductivity σ should be reduced in Eq. (5.4). A generalized Ohm's law also can be expressed as

$$\overrightarrow{j} = \sigma \overrightarrow{E} \tag{5.5}$$

If the magnetic field exists, the electron motions are confined by the magnetic field. Therefore, the electrical conductivity is reduced. Then, from Eq.(5.5), the electric field strength is increased for a given current.

A series of probe experiments was performed by Domonkos et al. [5] in the near field of the D55 plume. The local plasma potential was obtained using an emissive probe and a Langmuir probe. Figures 5.19 and 5.20 show radial profiles of plasma potential at axial distances of 10 mm and 50 mm from the thruster exit plane, respectively. Experimental data were measured with respected to the cathode potential of 14V [5], so here we add 14V to the measured data for consistency with the simulation. Close to the thruster, the *Boltzmann model* overpredicts the potential. The *Detailed model* captures the shape quite well although it overpredicts the potential too. However, the result is better than the *Boltzmann model* and if the magnetic field

is considered the comparison is even better. At 50 mm from the thruster, the *Boltzmann model* still greatly overpredicts the potential. The *Detailed model* without the magnetic field provides improved agreement with the measured data and the magnetic field case again gives even better results. However, even with the consideration of the magnetic field, the difference between the measured data and the simulation results is significant. This difference suggests the axial component of the magnetic field may not be small enough to ignore. We assume that the axial component of the magnetic field is much smaller than the radial component based on the SPT-100 thruster report [18]. However, there is no direct evidence that it is true in the D55 thruster. If the axial magnetic component is strong enough, then the confinement of the electron motion would be stronger with the consideration of the axial component of the magnetic field. Therefore, the potential gradient would be increased. Also, this feature is consistent with the comparison of ion current in Section 5.4.4 and the comparison of electron number density in Section 5.4.5. This feature is discussed later. Another possible reason of the difference is the plasma potential at the thruster exit used in the simulation. In this study, we assume a plasma potential of 145 V at the thruster exit center for the three different D55 Hall thruster operating conditions based on the measured data of Keefer [83]. However, there is the possibility that three different D55 Hall thruster operating conditions produce slightly different thruster exit and plume properties. The Xe^+ exit velocity measured by Keefer [83] may not correspond to the thruster exit potential in the University of Michigan operating condition.

Comparisons between measured data and simulation results for the potential in the far-field plume are shown in Fig. 5.21. The measured data were obtained by Zakharenkov et al. [91]. At a distance of 500 mm from the thruster, the *Boltzmann model* again greatly overpredicts the potential whereas the *Detailed model* reproduces fairly well the measured profiles. One can see that the potential of the *Detailed model* with the magnetic field is slightly larger than that of the *Detailed model* without the

magnetic field case in the far-field. The reason is that the potential gradient of the *Detailed model* with the magnetic field is stronger than without the magnetic field model in the near-field, and the outflow boundary potential is the same for both models. Therefore, from a certain point, the potential gradient of the *Detailed model* without the magnetic field should be stronger than that with the magnetic field model.

5.4.4 Ion Current Density

Accurate ion current density prediction is one of the most important goals of plasma plume simulation because it has a direct relation to the plume impingement. Ion current density profiles predicted by the simulation are compared with the experimental data [5] in Figs. 5.22 and 5.23 along radial lines located at axial distances of 10 and 40 mm from the thruster exit plane, respectively. Both the *Boltzmann model* and the *Detailed model* give good predictions at 10 mm. At 40 mm, the *Detailed model* is still in good agreement, but the *Boltzmann model* clearly underpredicts the measured results. This underprediction of the current density in the *Boltzmann model* implies a possibility that the simulation overaccelerates ionized particles in the radial direction between 10 and 40 mm from the thruster exit plane.

Figure 5.24 shows further comparisons between measured data [91] and simulation results for ion current density in the far-field plume. The *Detailed model* shows better agreement with measurements though both models underpredict the measured values. This underprediction of ion current density over the entire domain suggests that the simulation may overaccelerate ionized particles in the radial direction. This feature is consistent with the comparisons of electron number density shown in Figs. 5.26, 5.27, 5.28 and 5.29. This feature is discussed later. One can see that the prediction is better when the magnetic field is considered. This feature implies that the *Detailed model* with the magnetic field generates less acceleration in the radial direction than the model with the magnetic field.

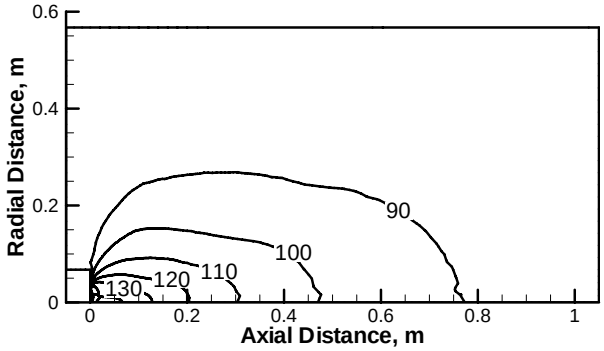

Figure 5.16: Contours of plasma potential (in V), the *Boltzmann model*

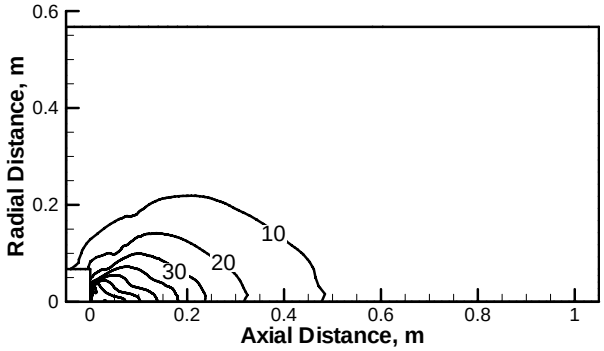

Figure 5.17: Contours of plasma potential (in V), the *Detailed model*, without magnetic field

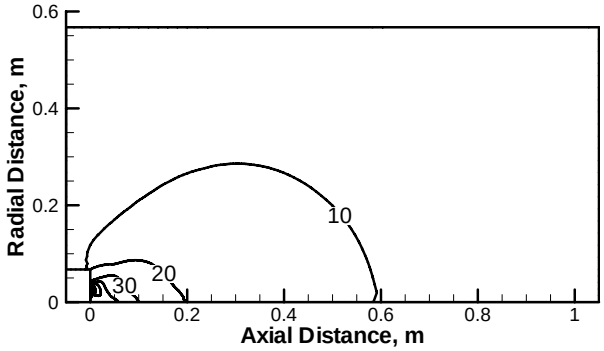

Figure 5.18: Contours of plasma potential (in V), the *Detailed model*, with magnetic field

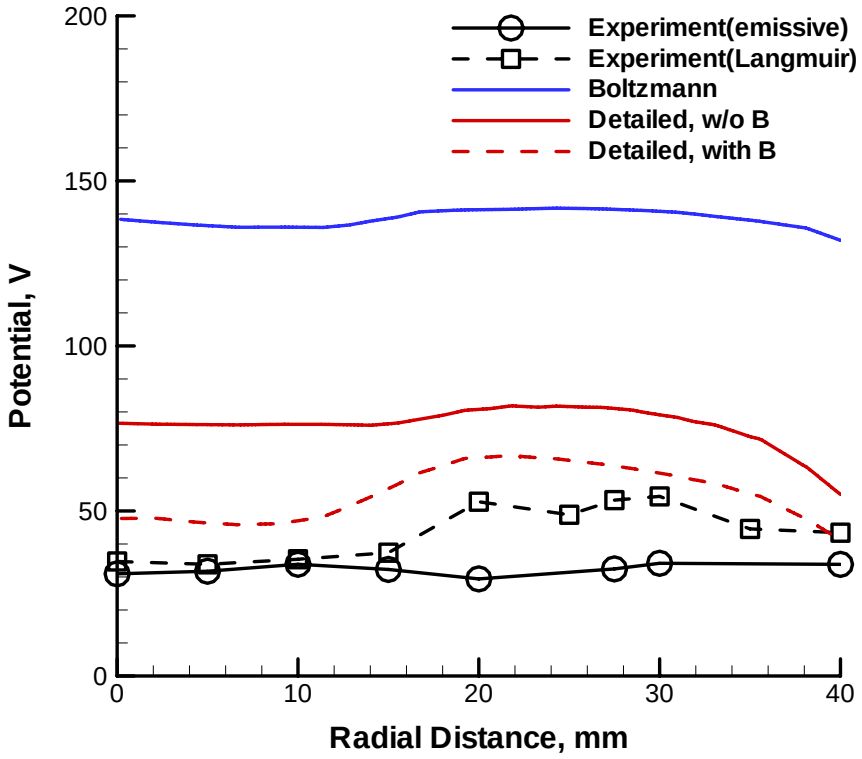

Figure 5.19: Radial profiles of plasma potential, 10 mm from the thruster exit plane

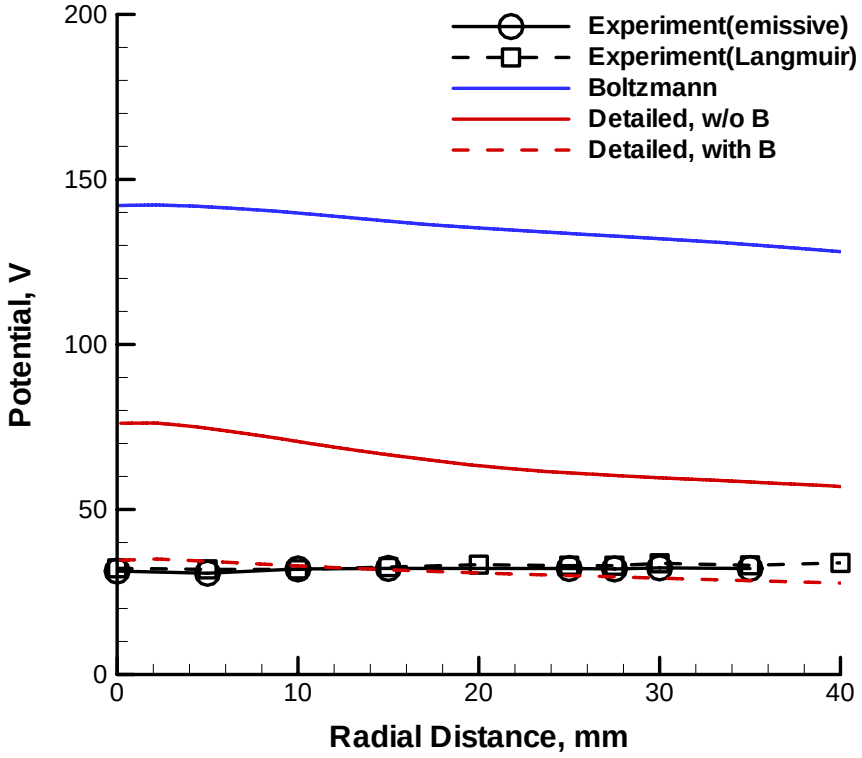

Figure 5.20: Radial profiles of plasma potential, 50 mm from the thruster exit plane

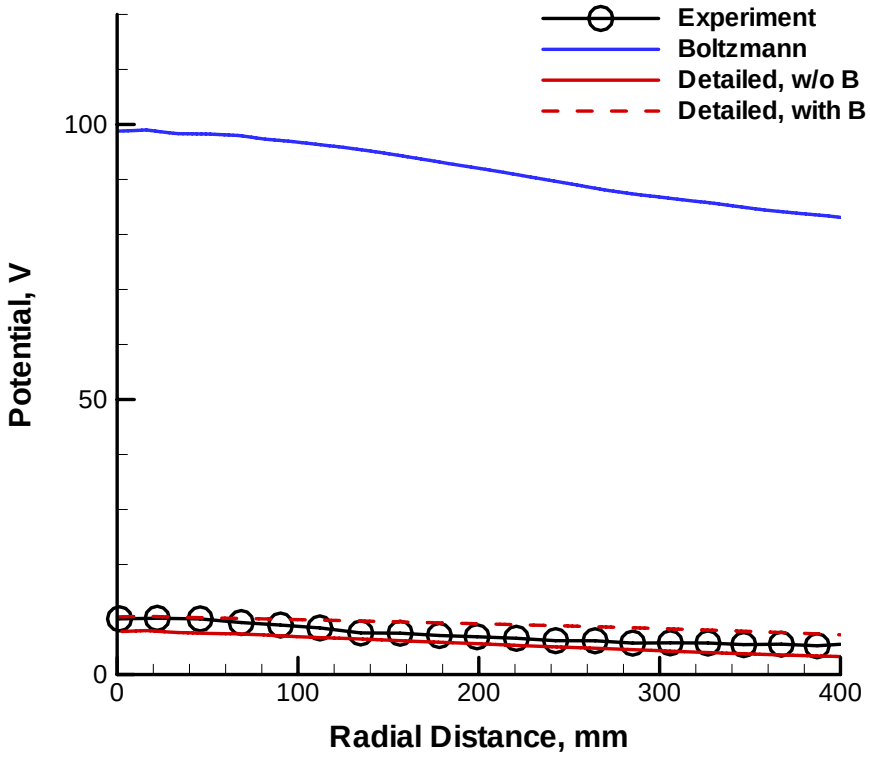

Figure 5.21: Radial profiles of plasma potential, 500 mm from the thruster exit plane

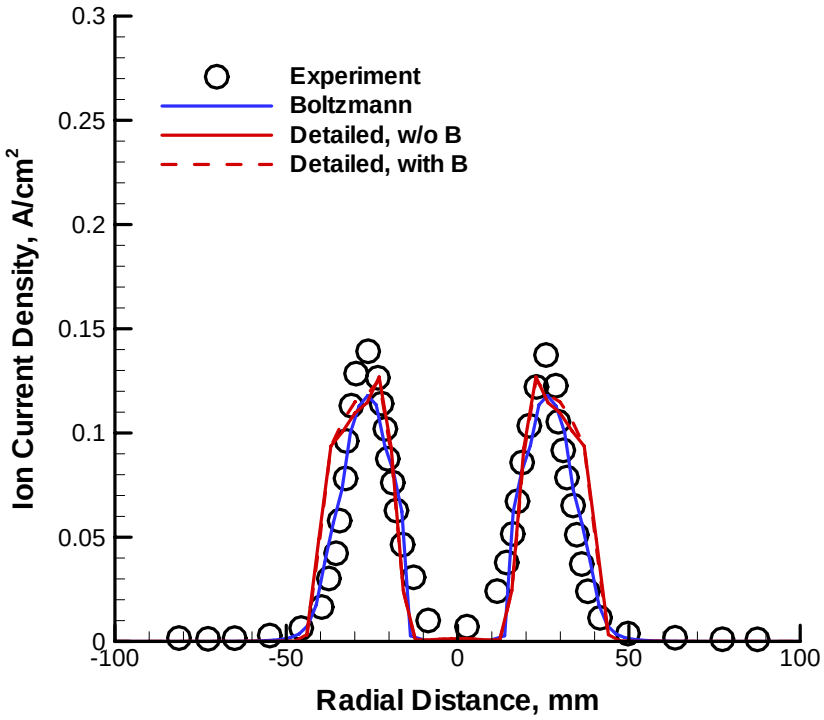

Figure 5.22: Radial profiles of ion current density, 10 mm from the thruster exit plane

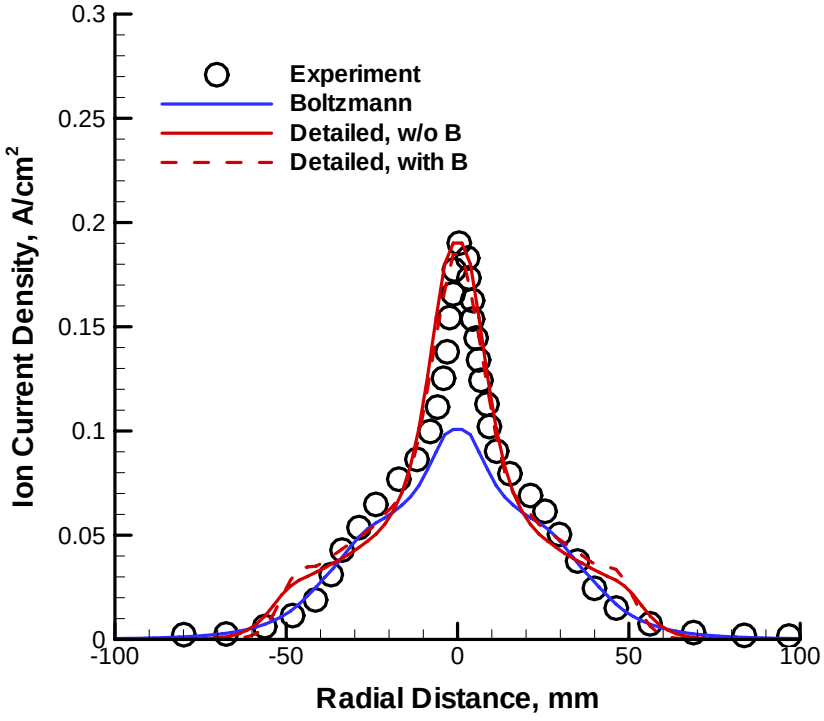

Figure 5.23: Radial profiles of ion current density, 50 mm from the thruster exit plane

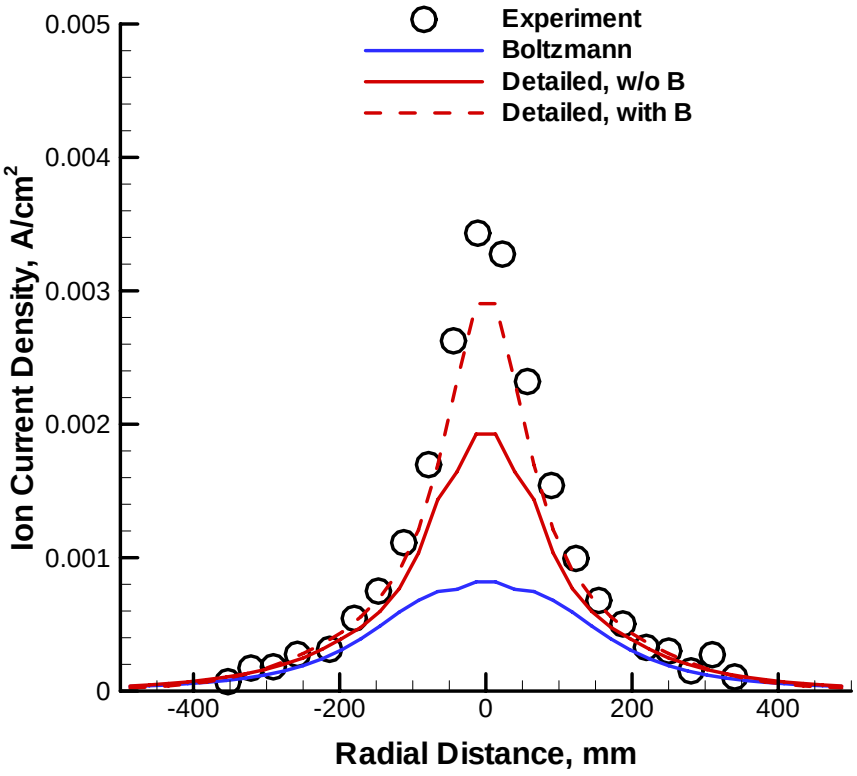

Figure 5.24: Radial profiles of ion current density, 500 mm from the thruster exit plane

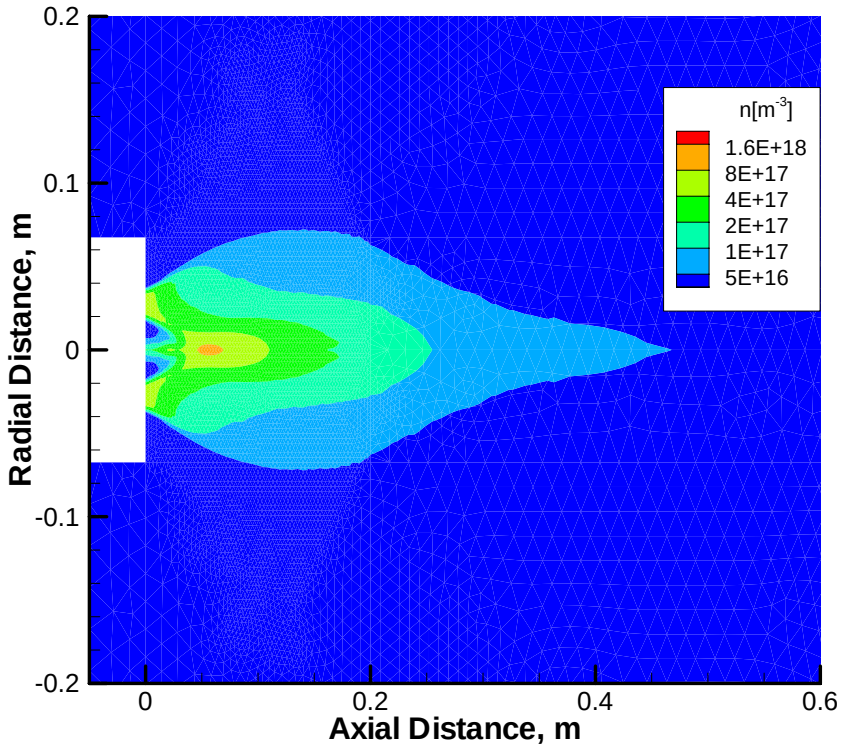

Figure 5.25: Contours of ion number density distribution

The variation of the ion current density with axial distance from the thruster indicates that the ion flow begins as an annulus and then merges into a cylinder-shaped beam. Figure 5.25 shows this merging feature. This feature occurs because the annular ion flow diverges with an angle of 10 degrees which overlaps at the centerline of the thruster as the flow convects downstream.

5.4.5 Electron Number Density

Measurements of electron number density [5] are compared with the simulations for radial profiles at 10 and 50 mm in Figs. 5.26 and 5.27, respectively. The simulation values represent the total charge density obtained from the number densities of the Xe^{+} and Xe^{2+} ions. The measured data have an accuracy of 50 percent at 10 and 50 mm. Therefore, in the near field, most of the simulation data underpredict the measured values. The peak electron number density measured at both stations is al-

most double the total charge density assumed in the simulations at the thruster exit plane. One possible interpretation of these comparisons is that the axial component of electric fields in the simulation is so strong that the acceleration of ions is overestimated in the axial direction. One possible way to address such differences between the model and the measured data would be to include modeling of axial confinement of electrons caused by the magnetic field.

Further comparisons between measured data and simulation results for electron number density in the far-field plume are shown in Figs. 5.28 and 5.29. The measured data were obtained by Gulczinski et al. [89] using microwave interferometry. The uncertainty for the measured data is 10%. The *Detailed model* shows better agreement with the measurements though both models still underpredict the measured values over the entire radial profile. One possible reason for these differences between the *Detailed model* results and the experiment is that the electric fields in the simulation accelerate the ions too much in both the axial and radial directions. This feature also suggests axial confinement of the electrons caused by the magnetic field. It was shown that the axial component of the magnetic field is much smaller than the radial component in an SPT-100 thruster [18], although there is no direct evidence that it is true in the D55 thruster. Measurements of the axial component of the magnetic field are required to help resolve this issue, and no such data exist as of now.

5.4.6 Electron Temperature

Figures 5.30 and 5.31 show radial profiles of electron temperature at distances of 10 and 50 mm from the thruster, respectively. The experimental uncertainty is reported to be 10% [5]. Electron temperature is constant in the *Boltzmann model* and here we show the value of 10 eV which is assumed in the simulation. At 10 mm, it is clear from the measurement that there is significant spatial variation in the electron temperature caused by the dynamics of the plasma at the exit of the acceleration

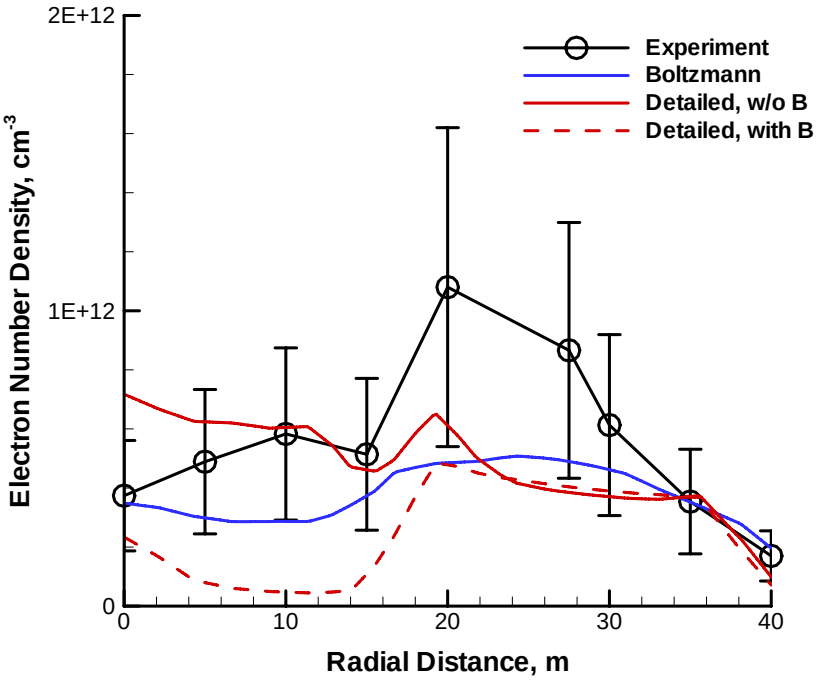

Figure 5.26: Radial profiles of electron number density, 10 mm from the thruster exit plane

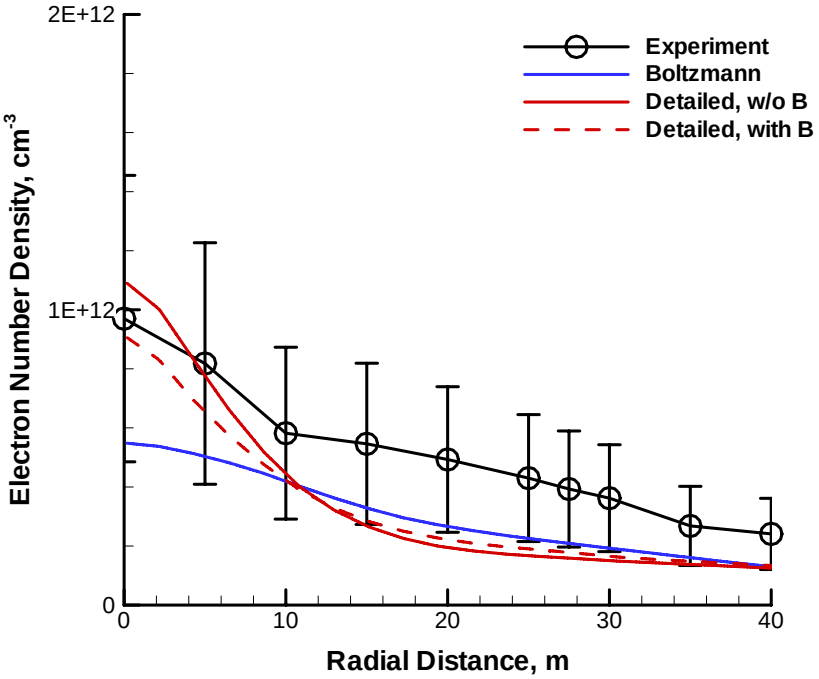

Figure 5.27: Radial profiles of electron number density, 50 mm from the thruster exit plane

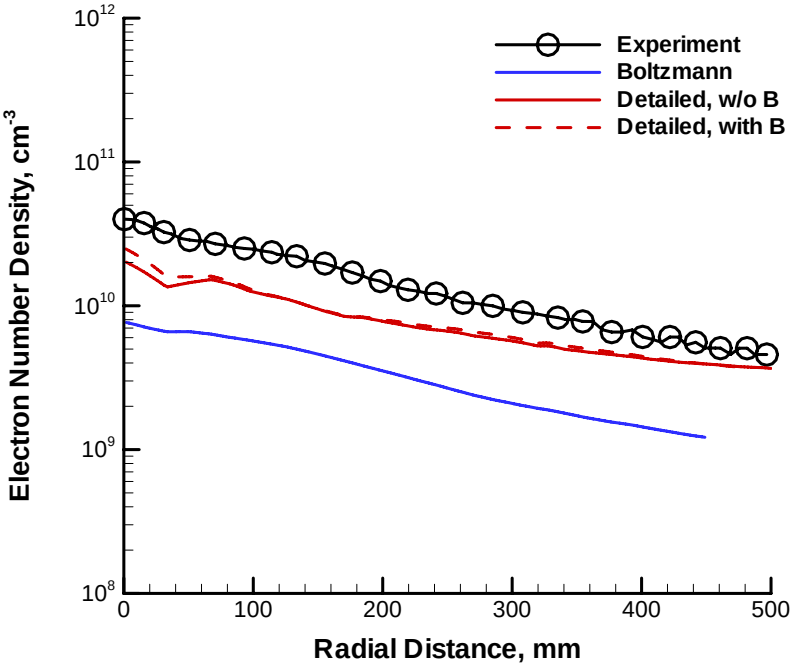

Figure 5.28: Radial profiles of electron number density, 500 mm from the thruster exit plane

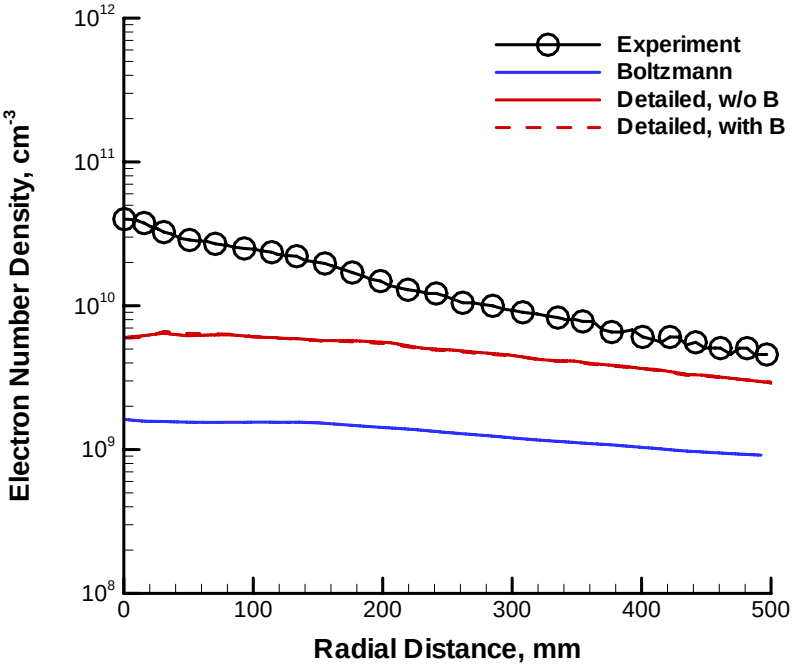

Figure 5.29: Radial profiles of electron number density, 1000 mm from the thruster exit plane

channel. In general, although the *Detailed model* provides reasonable agreement with the measurements, the radial gradients predicted by the model are smaller than the measured data indicate. These disparities between the models and the measurement indicate that more elaborate thruster exit boundary conditions are needed. In fact, it is known that the Detailed model is relatively more sensitive to boundary conditions than the *Boltzmann model*.

If the magnetic field is considered, the thermal conductivity is

$$\kappa_e = \frac{2.4}{1 + \frac{\nu_{ei}}{\sqrt{2}\nu_e}} \frac{k^2 n_e T_e}{m_e \nu_e} \left(\frac{1}{\omega_c^2/\nu_e^2 + 1} \right) \tag{5.6}$$

Equation (5.6) shows that in the region of finite magnetic field in which $\omega_c \gg \nu$, the resulting thermal conductivity coefficient is very small. Therefore, the electron motion is confined and the electron temperature decreases. In Fig. 5.30, one can see that the electron temperature decreases if the magnetic field is considered. However, Fig. 5.30 also shows that the *Detailed model* with a magnetic field underpredicts the electron temperature. This suggests that we need more accurate physical model for the electron motion.

Far-field prediction of the electron temperature profiles are presented in Fig. 5.32. The measured data were obtained by Zakharenkov et al. [91]. It is clearly shown that the *Detailed model* gives good agreement with the measured data in the far field. However, the main reason of the agreement in Fig. 5.32 is not the physical model accuracy but rather the 1.5 eV electron temperature boundary condition.

5.4.7 Velocity Distribution Function

Figures 5.33 and 5.34 show the distributions of ion axial velocity obtained from the simulations at 1 mm and 10 mm from the thruster exit, respectively. In Fig. 5.33, all models show distinct three populations. The lowest velocity population indicates the slow ions created by the charge exchange collisions. The middle and high velocity

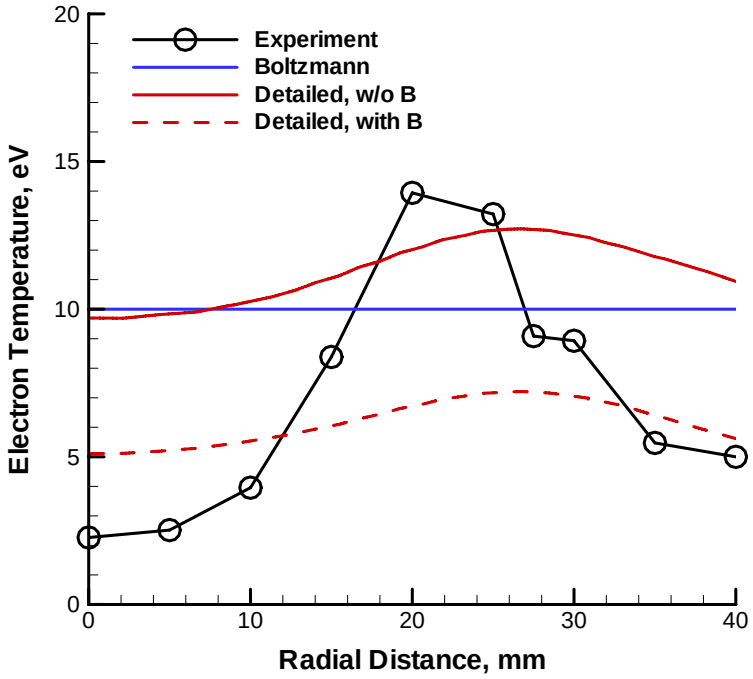

Figure 5.30: Radial profiles of electron temperature, 10 mm from the thruster exit plane

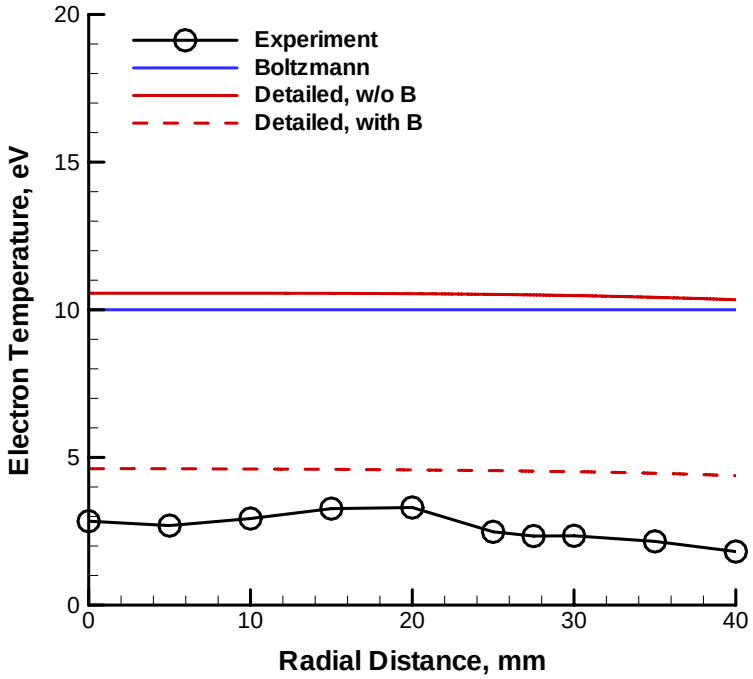

Figure 5.31: Radial profiles of electron temperature, 50 mm from the thruster exit plane

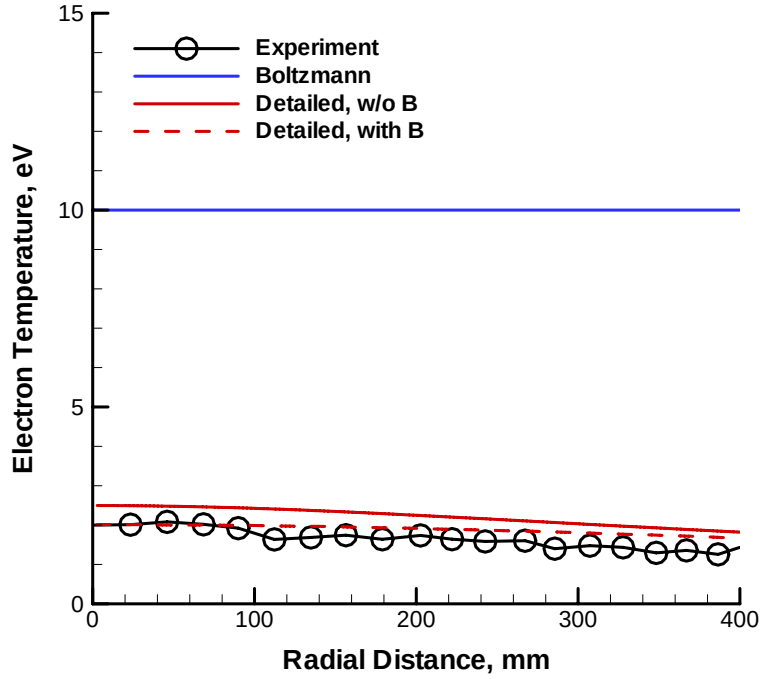

Figure 5.32: Radial profiles of electron temperature, 500 mm from the thruster exit plane

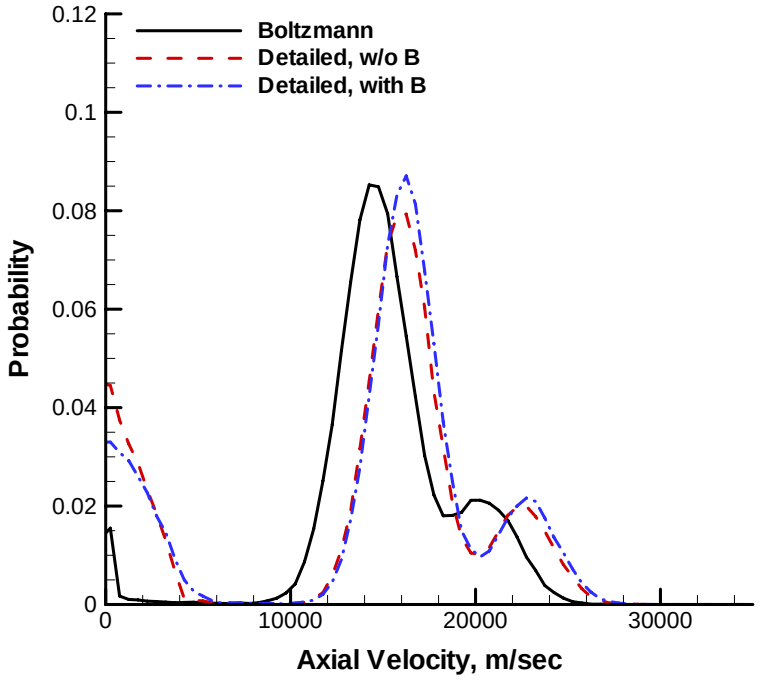

Figure 5.33: Distribution function of ion axial velocity component at 1 mm axially from the thruster and 28 mm radially from the plume centerline

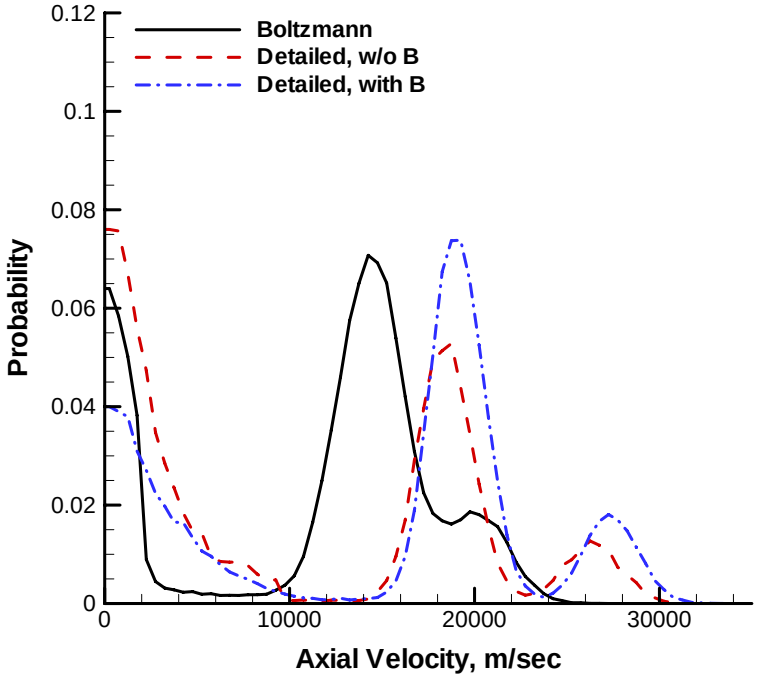

Figure 5.34: Distribution function of ion axial velocity component at 10 mm axially from the thruster and 28 mm radially from the plume centerline

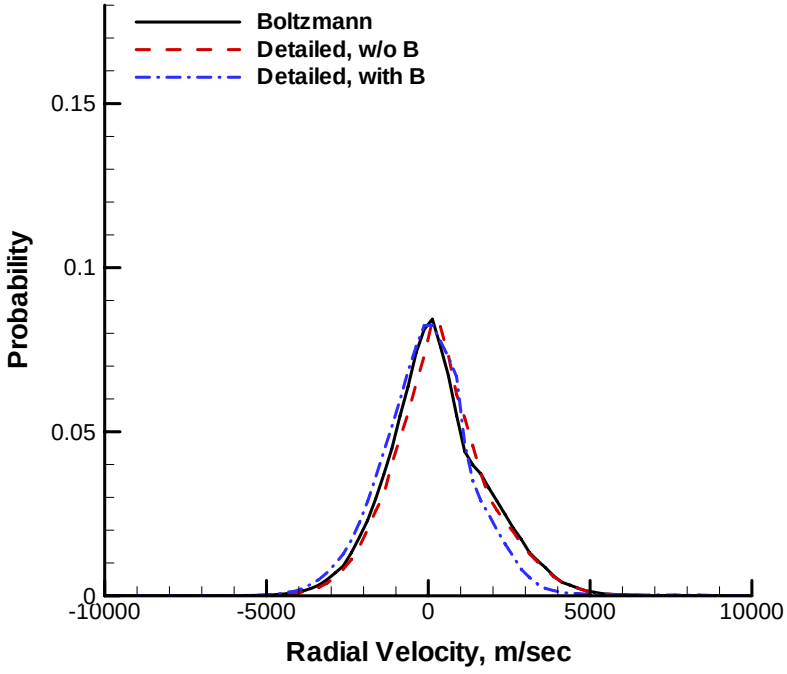

Figure 5.35: Distribution function of ion radial velocity component at 1 mm axially from the thruster and 28 mm radially from the plume centerline

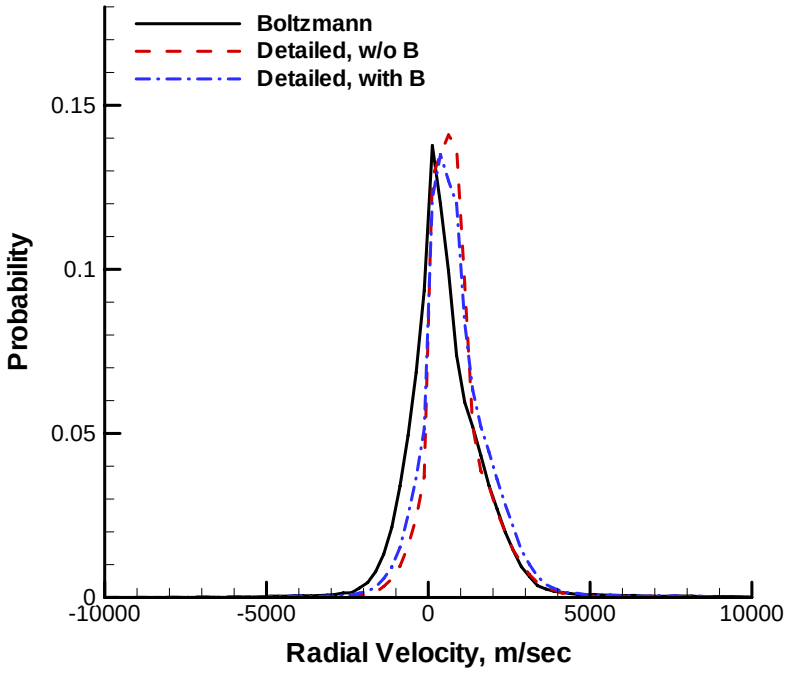

Figure 5.36: Distribution function of ion radial velocity component at 10 mm axially from the thruster and 28 mm radially from the plume centerline

populations show the Xe^{+} and Xe^{2+} components, respectively. As we mentioned in Section 5.4.3, the potential gradient in the *Detailed model* is greater than that in the *Boltzmann model*. Therefore, ions experience more acceleration and the velocity distributions of the *Detailed model* are shifted to the right compared with the *Boltzmann model*. Also, the velocity distribution of the *Detailed model* with the magnetic field is shifted slightly further to the right compared with the case without the magnetic field. This shift is more clearly shown in Fig. 5.34 because the ions accelerate from z = 1 mm to z = 10 mm. Also, one can see in Figs. 5.33, and 5.34 that a lot of charge exchange processes occur. These charge exchange events will be discussed later.

Figures 5.35 and 5.36 show the distributions of radial ion velocity obtained from the simulations at 1 mm and 10 mm from the thruster exit, respectively. All models show almost the same radial velocity profile. In Fig. 5.36, the distribution is not symmetric since the plasma potential profiles are not symmetric across the channel

exit. Also note that the simulation data are collected in a volume just above the channel center line. The simulation results of ion axial velocity are compared with Laser Induced Fluorescence (LIF) measurements of the Xe^+ axial velocity component obtained by Keefer et al. [83] in Fig. 5.37. In Ref. [83], it is explained that the reported velocity data represent the central value of the Xe^+ velocity distribution functions detected by the LIF diagnostic. Therefore, for consistency with the experiment, the simulation velocity in Fig. 5.37 is the most probable value of the computed Xe^+ velocity distributions. Figure 5.37 shows the axial velocity profiles at a radial position of 27.5 mm which is along the thruster channel center. It is clear that the *Boltzmann model* fails to produce sufficient ion acceleration in the near field of the plume. This is an expected result because the plasma potential gradient shown in Fig. 5.16 is not enough to give ions significant acceleration. As discussed with reference to Fig. 5.17, the *Detailed model* predicts strong ion acceleration in the near field region and rapidly accelerates the ions from the thruster exit velocity of 15 km/s to a value of about 18 km/s that corresponds to the measured data and the results become slightly better when the magnetic field is considered. The simulation result, however, overestimates the axial velocity at z=1 mm. One possible explanation is that there may be a lot of CEX collisions in front of the thruster. As mentioned in Fig. 5.33, a lot of CEX collisions occur in the near field plume. Because of CEX collisions, some slow neutral atoms become slow ions. These slow ions may lower the central value of the ion velocity distribution function. This discrepancy also suggests that improved thruster exit flow conditions may be needed.

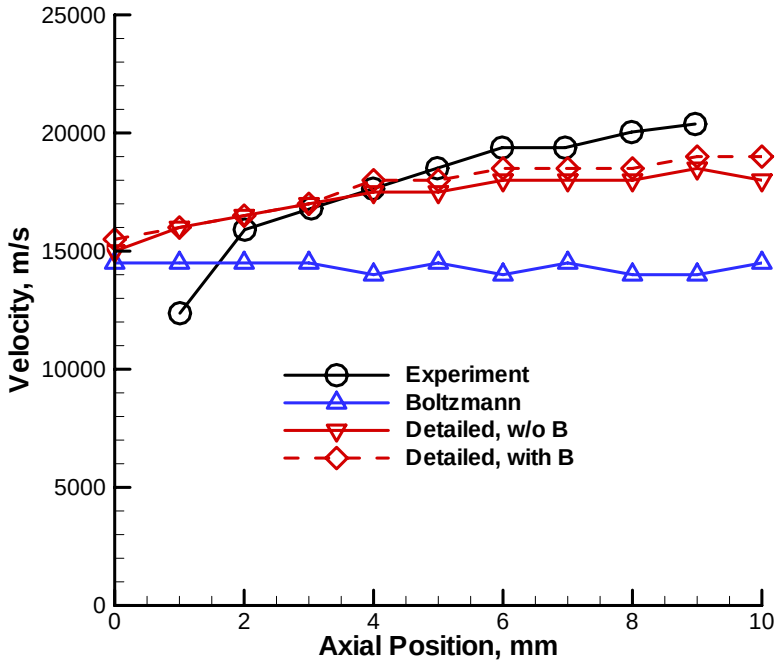

Figure 5.37: Axial components of ion velocity at a radial position of 27.5 mm

5.5 Conclusions

A hybrid particle-fluid PIC-DSMC model using both the *Detailed model* and the *Boltzmann model* for the fluid electrons is applied to simulate the plume flow from the D55 anode layer Hall thruster. The present model includes the near-field plasma plume region where the magnetic field leaked from the acceleration channel may have a substantial effect on the plasma potential distribution. Analysis of the plasma potential distribution including the magnetic field shows that the field does indeed significantly affect the profile of the plasma in the *Detailed model*. For instance, in the case of zero magnetic field, the plasma has a potential of about 80V at 10 mm from the thruster exit, while in the case of a finite magnetic field, the plasma potential is about 60V. Results predicted by the *Detailed model* with the magnetic field are found to be in better agreement with several different sets of experimental data. Generally, the *Detailed model* provides better results than the *Boltzmann model*. The inclusion

of the magnetic field in the *Detailed model* gives closer agreement for prediction of the plasma potential distribution to the measured one. The *Detailed model* with the magnetic field consideration more accurately predicts the extended ion acceleration region outside the thruster. By comparison, the *Boltzmann model* indicates almost no ion acceleration outside the thruster. The simulation results of the *Detailed model* and the *Boltzmann model* consistently underpredict the electron number density. This disparity may be caused by the simulated electric fields being too strong and leading to overacceleration of the ions in the axial and radial directions.

CHAPTER 6

SUMMARY AND FUTURE WORK

This thesis presents two main topics: Performing axisymmetric hydrodynamic simulations of plasma flow within a D55 TAL thruster and axisymmetric particle simulations of plasma plume flows from a D55 TAL thruster. The simulations of plasma flow within the D55 were performed using the various D55 operational conditions. The simulation results were subsequently used to determine the initial conditions for the plasma plume simulations. The simulations of the plasma plume flow from the D55 TAL thruster were investigated using MONACO-PIC [1] [52], a hybrid PIC-DSMC code developed at the University of Michigan that contains both the *Boltzmann model* and the *Detailed model*.

In this study, we considered three operational conditions corresponding to three different experiments. These experiments were conducted at the University of Michigan [5] [89], TsNIIMASH [91], and the University of Tennessee Space Institute (UTSI) and Lockheed Martin Astronautics (LMA) [83].

The following includes a brief summary of the most important lessons learned from this research and presents a number of possible directions for future research on this topic.

6.1 Hydrodynamic Plasma Simulation of the D55 Hall Thruster Channel

6.1.1 Summary and conclusions

The hydrodynamic model [63] is used to describe the plasma flow within a D55 TAL thruster. In particular, Hall thruster device modeling efforts were focused on calculating the thruster exit conditions. The hydrodynamic approach is chosen because it offers a relatively quick turnaround on simulation results –only a few minutes are required for a single run– while maintaining a physics-based foundation.

One important finding of our study was the discovery of the variation of the ion velocity and the ion number density profile along the radial direction. At the center of the thruster channel exit, the ion velocity has a minimum and the ion number density has a maximum.

6.1.2 Future Work

Several aspects of the hydrodynamic model must be improved to obtain more accurate results in the future.

6.1.2.1 Treatment of the Electron Temperature

In this investigation, the electron temperature is assumed to be constant. However, to improve the hydrodynamic model, the electron energy balance equations should also be considered. Further, the model should consider thermal conductivity.

6.1.2.2 Proper Magnetic Field Information

In this research, we assumed a profile of the magnetic field within the D55 channel because an accurate magnetic field profile for the thruster was not available to us. The model would provide more accurate results if proper, fine-grained magnetic field data were provided.

6.1.2.3 Stability of the Model

The model is very sensitive to the initial and the boundary conditions. The sensitivity problem is intensified when the electron temperature is high, e.g., in the D55 thruster channel. If the source terms are zero, the solution method provides stable solutions, as long as the CFL condition is met. However, the nature of the source terms of the governing equations are the origins of this problem. Due to ionization and electric field considerations, the source terms lead towards possible instability of the code. Using an implicit scheme instead of an explicit scheme would be a possible way to solve the instability problem. The other reason of the instability is the ion density undershooting by the Roe solver. The hydrodynamic model uses the isothermal version of the Roe solver [64] [78] to calculate fluxes. However, the Roe solver undershoots the ion density, and gives negative density when the density is close to zero. One possible solution is using a different solver such as a HLLC Rieman solver [95] [96] which does not undershoot the ion density.

6.1.2.4 Electron Mobility Treatment

Modeling of electron mobility is an area currently under active research. Much is still unknown about the mechanisms that transport electrons across magnetic field lines. However, experimental measurement of electron mobility is difficult. Moreover, standard classical electron mobility, due to collisions with the heavy particles, is not sufficient to provide the necessary mobility for Hall thruster operation. There are two other additional transport mechanisms considered. Bohm mobility due to plasma turbulence, and mobility due to wall collisions. However, these forms of electron mobility are complex and difficult to model accurately. Further research is required for these two types of mobility. Also the underlying physical processes should be investigated which are still not fully understood. Once mobility mechanisms are known and can be implemented into simulation models, the hydrodynamic model

results and those of the Hall thruster plasma plume simulations will be more accurate.

6.1.2.5 Geometry Treatment

A more complete treatment of the geometry of the thruster would improve the accuracy of the hydrodynamic model. The simulation domain should include the D55 nozzle geometry. Also the geometry model should extend the domain past the exit plane and incorporate the near-field plume. The near-field plume region includes important dynamics that may affect the calculation of the plasma flow within the channel [19]. This would allow a more complete approach for a better assessment of thruster properties such as the thrust and characterization of ion acceleration outside the thruster.

6.1.2.6 The Incorporation of Doubly Charged Ions

Doubly charged ions can represent a significant fraction of the ion current and will affect the calculated plasma properties that may alter the structure of the flow. We considered the double charged ion by introducing mixed charge ions and a mixed ion velocity. However, including a more rigorous physical model for the double charged ion as a separate species would improve the accuracy of the hydrodynamic model.

6.2 Particle Simulations of Plasma Plume Flows from the D55 Hall Thruster

6.2.1 Summary and Conclusions

This thesis focused on performing and evaluating several DSMC-PIC particle simulations that were performed for the plume flows from the D55 Hall thruster under different operation conditions. These simulations employed the *Boltzmann model* and the *Detailed model*.

The *Boltzmann model*, a standard, and the simplest fluid electron model, describes electron properties using several strong assumptions, such as the fluid electron flow

is isothermal, collisionless, the electron pressure obeys the ideal gas law and the magnetic field is neglected.

The *Detailed model*, a more detailed fluid electron model, describes electron properties, such as the electron velocity stream function, the plasma potential, and the electron temperature. The magnetic field is also considered in this model. A general purpose finite element solver is used in this model for computing electron properties. Several implementation issues were reviewed.

Our study compared simulation results with available experimental data. This comparison included the near-field plasma plume region where the magnetic field that leaked from the acceleration channel may have a substantial effect on the plasma potential distribution.

Analysis of the plasma potential distribution across the magnetic field showed that the field significantly affects the profile of the plasma potential in the *Detailed model*. The *Boltzmann model* fails to accurately predict the plasma potential. Simulation results predicted by the *Detailed model* were found to be in better agreement with several different sets of experimental data. When the magnetic field was considered in the *Detailed model*, the prediction of plasma potential improved.

Further, the *Detailed model* with the magnetic field consideration also predicted the extended ion acceleration region outside the thruster with more accuracy. By comparison, the *Boltzmann model* indicated almost no ion acceleration outside the thruster.

The simulation results of the *Detailed model* and the *Boltzmann model* consistently underpredicted the electron number density. The cause of this disparity may lie in possibly calculating too strong electric fields in the simulation, which would lead to an overacceleration of the ions in the axial and radial directions.

The *Detailed model* was superior to the *Boltzmann model* in predicting the electron temperature, but more accurate physics are needed to describe the motion of the

electrons.

Another important result of this study was that ions are affected by the magnetic field leakage. We expected that electrons are magnetized while ions would not be magnetized. Our investigation showed that, however, plasma flow across the magnetic field generates additional electric fields which act to increase the strength of the electric fields. One possible physical explanation is that the confinement of the electron motion by the magnetic field reduces the electric conductivity. This reduction results in increased strength in the electric fields.

6.2.2 Future Work

While significant progress has been made in this study for the numerical simulation of Hall thruster plumes, this research also revealed the need for further study in several areas.

6.2.2.1 Need for a Higher Order Finite Element Solver

As pointed out in Chapter 5, Equations (2.8), (2.17), and (2.18) have several second order derivatives in the source terms. However, the current finite element solver adopted a linear element. This problem was alleviated by two facts: first these source terms were usually weak; second, the least-squares derivative calculation method on an unstructured mesh partially took into consideration these second derivatives. However, implementation of a higher order finite element solver would provide more accurate results.

6.2.2.2 Two Dimensional Magnetic Field

In this research, only the radial component of the magnetic field was considered. However, the simulation results suggested that the axial component of the magnetic field should also be considered. Even though there is no measurement data of the axial component of the magnetic field for the D55 TAL thruster as of now, the axial

component can be calculated with the aid of the zero divergence condition required by Maxwell's laws of electromagnetism. A two-dimensional magnetic field profile would provide more accurate results for the ion accelerations and the ion current density profiles.

6.2.2.3 Further Improvements in Parallel Efficiency

MONACO-PIC parallelizes the hybrid DSMC-PIC algorithm through domain decomposition. However, the parallel efficiency of MONACO-PIC is rather low. The reason of inefficiency on the parallel computing results from message passing. Seeking a more effective solution to reduce the message passing may improve the parallel performance of the code.

6.2.2.4 Full Scale Three-dimensional Simulation of Plasma Flows

Because of the characteristics of the axisymmetric simulations, we calculated the azimuthal velocities of the electrons by a combination of two limiting cases, i.e., the MHD case and the drift case. Full three-dimensional simulations of plasma flows would provide a way to check the accuracy of our method. Also, full three-dimensional simulations would assess the accuracy of the axisymmetric model by comparing the results. However, a three-dimensional simulation of plasma plume flow inside a large vacuum chamber requires a very large number of time steps, particles, and cells. This problem represents a great challenge for particle simulations.

6.2.2.5 Further Assessments of the Model Using Other Types of Hall Thrusters

Hybrid DSMC-PIC simulations are generally complex and not standardized. In this thesis, our research focused on the D55 TAL thruster. Further assessments of the model using other Hall thrusters (e.g., SPT 100) would consolidate our model.

Studies of these problems will provide complete and concrete numerical solutions at the kinetic level, to analyze plasma plume flows in space.

APPENDICES

APPENDICES A

CONTROL CARDS

There is a specific file "**Pic.cfg**" needed to run MONACO-PIC. It forms an input deck of control cards. MONACO-PIC will scan this file periodically to check whether there are some specific new requests from the user. Cards are not required to follow a specific order, and most cards are optional. A control card is composed of "$" + keywords, and then a special block of data. To disable a control card, the user can simply remove the "$" in front of the keyword but leave the keyword inside the file. The format and meaning of control cards are listed below.

1. **$PLASMABCS NUM**

   Specifies NUM of boundary conditions for plasma potentials (V), electron velocity stream function ($m^{-1}s^{-1}$), electron temperatures T_e (eV). There must be NUM lines of data following this line with format:

   type subtype subtype subtype T_e

   type = -1 (wall), -2 (inlet), -4 (outlet), -8 (symmetric), positive number (node id);

1 (Dirichlet BC),

subtype = 2 (Neumann BC),

0 (undefined, will skip)

The first 3 parameters are critical for both the *Boltzman model* and the *Detailed model*, while the last 4 parameters are used for the *Detailed model*.

(e.g.) -2 1 145.0 2 4822.5e+19 1 20

defines an inflow B.C. with plasma potential $\phi = 145\ V$, stream function gradient $d\psi/dn = 4822.5e+19\ m^2/sec$, electron temperature $T_e = 20\ eV$.

(e.g.) 13813 1 14 0 4822.5e+19 1 5

defines at the node point with id 13813, the plasma potential $\phi = 14\ V$, stream function gradient undefined, electron temperature $T_e = 5\ eV$.

2. **$PIC**

   temperature, ion density, potential

   Defines the 3 reference parameters for the Boltzmann relation, usually the reference point is at the thruster exit.

$$\phi = \phi_{ref} + \frac{kT_{ref}}{e} log\left(\frac{n_e}{n_{ref}}\right) \tag{A.1}$$

   (e.g.) $PIC 10.0 1.0e+18 145.0

   defines the electron temperature $T_{ref} = 10.0\ eV$, ion number density $n_{ref} = 1.0e+18\ m^{-3}$, reference plasma potential $\phi_{ref} = 145.0\ V$ in the reference cell.

3. **$PLASMA_POT_METHOD**

   integer

   Defines the electron fluid model.

   0 : the *Boltzmann model*

2 : the *Detailed model*

(e.g.) $PLASMA_POT_METHOD

2

Select the *Detailed model* for a simulation.

4. **$BEGIN_APPLY_E**

   integer

   Define the number of steps after which the electric field will be calculated and applied.

   (e.g.) $BEGIN_APPLY_E

   200

   Apply the electric field after 200 timesteps.

5. **$BCK_PRESSURE**

   Species, pressure, temperature, weight

   Define the neutral background pressure.

   e.g. 8.13e-4 300 10

   Define a neutral background pressure which is formed by the 3^{rd} species, pressure 8.13×10^{-4} Pa, temperature 300 K, and each cell has 10 background neutral particles.

   Background species particles are very special. They are not movable during the "move" process, and in the collision process, they participate in the CEX or momentum exchange collisions but their properties are not updated.

6. **$THRUSTER_EXIT_PROFILE**

   downward angle, upward angle, constant (x or y), center position, semi height

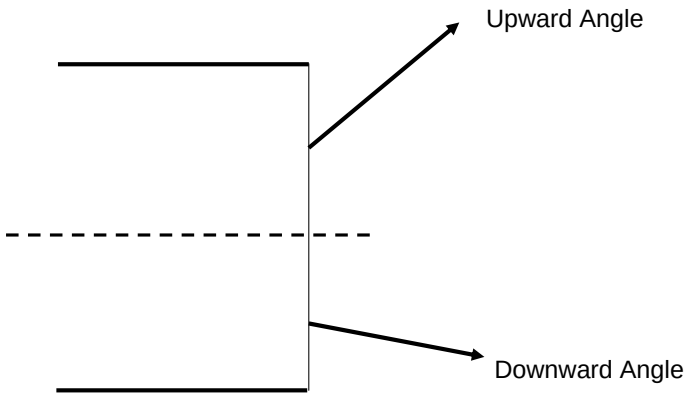

Figure A.1: A diagram for THRUSTER_EXIT_PROFILE

This card specifies the newly generated particles' velocities according to the position where they are created to achieve a velocity profile at the thruster exit. Usually, at the exit, the flow is divided into a lower part and an upper part, and the thruster centerline is along constant x (=1) or constant y (=2). Velocity is also affected by centerline position, and semi height of the thruster exit.

(e.g.) -10.0 20.0 2 0.0675 7.5e-3

define an exit flow profile with downward angle -10.0 deg., upwards angle 20.0 deg., the exit is along constant y, the centerline position is y=0.0675 m, and the height of the thruster = $2 \times 7.5 \times 10^{-3}$ m.

7. **$MERGE_SMALL_NEUTRAL value**

This card will enable the merging process of neutrals. MONACO-PIC will reduce the number of neutral particles by randomly discarding particles with lower weight and generating particles with higher weight.

8. **species_energy_onwall NUM**

Threshold value, wall$_1$,.....wall$_{NUM}$, x or y

Sample the energy spectrum of particles hitting a wall, for sputtering estimation.

e.g. $SPECIES_ENERGY_ONWALL 3

100 1 2 3 -1

Sample those edges which are 1^{st}, 2^{nd}, and 3^{rd} kind of wall boundary, and sort result by x (==-1) or y(==-2). Because of the CEX process near the wall, there will be some ions with very low energy near the walls, so it is desirable for the user to be capable of specifying a cutoff threshold value for final normalization. In the above example, the energy spectrum within [100 eV, 1000 eV] will be reported. If the user wants a spectrum from 0ev to 1000ev, just change the first parameter from 100.0 to 0.0.

9. **$FLEX_WALL_TMP NUM**

Step_begin, steps_intv, wall$_1$...wall$_{NUM}$ sortxy, ϵ_{al}**,** α_{ss}**,** ϵ_{ss}**,** T_c

Calculate the wall temperature when it is not fixed, like the baffles. This control card activates the fully radiation wall model:

$$Q + \sigma A(\alpha_{ss}T_c^4 - \epsilon_{ss}T_w^4 - \epsilon_{al}T_w^4) = 0 \tag{A.2}$$

The wall temperature T_w is decided iteratively.

e.g.: $FLEX_WALL_TMP 3

20000 1000 5 6 7 -1 0.6 0.2 0.54 77.0

Sample wall temperature after 20000 steps. Each evaluation cycle has 1000 steps, for wall type 1^{st}, 2^{nd}, and 3^{rd}, report their temperature. The output results will be sorted by x (=-1) or y (=-2), $\epsilon_{al} = 0.6$, $\alpha_{ss} = 0.2$, $\epsilon_{ss} = 0.54$, and $T_c = 77.0K$.

All heat flux on the front and backside of each baffle will be collected and a temperature T_{new} will be calculated, and a new temperature $T = (T_{new} + T_{old})/2$

will be used to update the old wall temperature. This temperature will be recorded inside a file named "adjustable_walltemp.dat".

10. **$FLUX_ACROSS_CONST_RAD NUM**

    NBEGIN x_o y_o R_1 R_{num}

    Sample the ion flux (single charged and double charged) across "NUM" of constant radii when the MONACO-PIC steps exceed "NBEGIN". A special file named "**ionflux_across_const_radi.dat**" will be created, which contains "NUM" blocks of data, the i^{th} block will represent the flux across the i^{th} radius, and each line will have information of :

    Angle total flux flux from single charged ion flux from double charged ion.

11. **$ENGY_ACROSS_CONST_RAD NUM**

    NCYCLE x_o y_o $R_1 ... R_{NUM}$

    Sample energy spectrum of ion flux across some constant radii and specific angle. Also record the Probability Distribution Function (PDF). A specific file named "**ionenergy_across_const_radi.dat**" will be created, and will have "NUM *180" blocks of data. Inside each block, the first line records the radius and angle, and the rest of this block is composed of 500 lines of data representing:

    Energy Level (eV), PDF of single charged ions, PDF of double charged ions, total PDF of all ions

12. **$CONSTANTZ_FLUX NUM SPAN**

    x_o y_o $x_1 ... x_{NUM}$

    Sample the ion number density along "NUM" of constant z. x_o and y_o are the position of the thruster center, usually (0, 0). Sampling span δx = SPAN. A specific file named "**ionflux_across_const_z.dat**" will be created, which

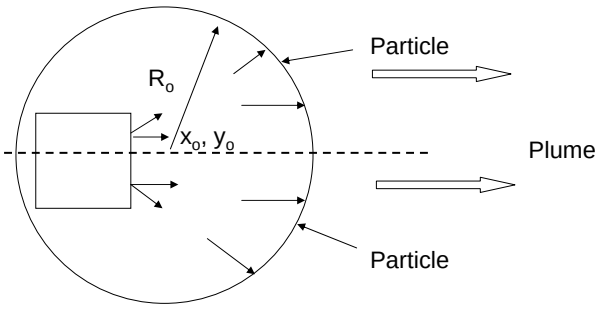

Figure A.2: Schematic of radial sampling

contains "NUM" blocks of data, the i^{th} block will represent the flux across the i^{th} station, and each line will have information of:

Radial distance ion current density from single charged ion ion current density from double charged ion total ion current density.

13. **VDF**

    x y

    Sample Velocity Distribution Function (VDF). x and y are position of the thruster center, usually (0, 0). A specific file name "**vdf.dat**" will be created, which contains

    x_o y_o **velocity flag VDF**

    if (flag==0) then velocity is axial velocity, and if (flag==1) then velocity is radial velocity.

14. **$ENABLE_WALL_SHEATH**

    Calculate the wall sheath potential using Eq. (2.15)

15. **$APPLY_CONST_MAGNETIC_FIELD**

Nx **Ny** x_{min} x_{max} y_{min} y_{max} B_{max} n_{max}

If this card is defined, MONACO-PIC reads the magnetic field data from "**B0_grid.dat**" which is a block of data with **Nx** rows and **Ny** columns of the magnetic field data. x_{min}, x_{max}, y_{min}, and y_{max} are minimum and maximum x and y positions where the magnetic fields are defined. B_{max} is the maximum value of the magnetic field. n_{max} is a local maximum which is chosen as the neutral particle density at the thruster exit.

B0_grid.dat consists of

x y B/B_{max}

APPENDICES B

THE DERIVATION OF THE POISSON EQUATION OF THE PLASMA POTENTIAL

The electron momentum equation is given by

$$\frac{\partial}{\partial t}(m_e n_e \overrightarrow{V_e}) + m_e n_e (\overrightarrow{V_e} \cdot \nabla)\overrightarrow{V_e} = -e n_e (\overrightarrow{E} + \overrightarrow{V_e} \times \overrightarrow{B}) - \nabla p_e + R, \tag{B.1}$$

where m_e is the mass of an electron, n_e is the electron number density, $\overrightarrow{V_e}$ is electron velocity, e is the electron charge, $\overrightarrow{E}$ is the electric field, $\overrightarrow{B}$ is the magnetic field, p_e is the electron pressure, and R is the friction term. It is further assumed that the electrons behave as a perfect gas ($p_e = n_e kT$), and that the friction term is given by

$$R = \frac{e n_e \overrightarrow{j}}{\sigma}, \tag{B.2}$$

where $\overrightarrow{j}$ is the current density, and σ is the electrical conductivity.

Assuming, a steady state, neglecting the inertial term on the left hand side of Eq B.1, and introducing the plasma potential $\nabla\phi = -\overrightarrow{E}$, a generalized Ohm's law is obtained.

$$\overrightarrow{j} = \sigma[-\nabla\phi + \overrightarrow{V_e} \times \overrightarrow{B} + \frac{1}{e n_e}\nabla(n_e k T_e)] \tag{B.3}$$

From the charge continuity condition, we can write

$$\nabla \cdot \overrightarrow{j} = 0, \tag{B.4}$$

or

$$\nabla \cdot \overrightarrow{j} = \nabla \cdot \sigma[-\nabla\phi + \overrightarrow{V_e} \times \overrightarrow{B} + \frac{1}{en_e}\nabla(n_e k T_e)] = 0 \tag{B.5}$$

From Eq. B.5, a generalized Poisson's equation is obtained

$$-\nabla \cdot [\sigma\nabla\phi] = -\nabla \cdot \sigma[\overrightarrow{V_e} \times \overrightarrow{B} + \frac{1}{en_e}\nabla(n_e k T_e)] \tag{B.6}$$

With an assumption of $\overrightarrow{B} = (B_r, 0, 0)$, the first term on the right hand side can be expressed

$$\begin{aligned}
\nabla \cdot \sigma[\overrightarrow{V_e} \times \overrightarrow{B}] &= \nabla\sigma \cdot [\overrightarrow{V_e} \times \overrightarrow{B}] + \sigma\nabla \cdot [\overrightarrow{V_e} \times \overrightarrow{B}] \\
&= \tfrac{\partial\sigma}{\partial r}(V_\phi B_z - V_z B_\phi) + \tfrac{\partial\sigma}{\partial z}(V_r B_\phi - V_\phi B_r) + \\
&\quad \sigma\left[\tfrac{1}{r}\tfrac{\partial}{\partial r}[r(V_\phi B_z - V_z B_\phi)] + \tfrac{\partial}{\partial z}(V_r B_\phi - V_\phi B_r)\right] \\
&= -\tfrac{\partial\sigma}{\partial z} V_\phi B_r - \sigma\tfrac{\partial}{\partial z}(V_\phi B_r) \\
&= -\tfrac{\partial\sigma}{\partial z} V_\phi B_r - \sigma\left[V_\phi \tfrac{\partial B_r}{\partial z} + B_r \tfrac{\partial V_\phi}{\partial z}\right]
\end{aligned} \tag{B.7}$$

The second term on the right hand side can be expressed as

$$\begin{aligned}
\nabla \cdot \sigma[\tfrac{1}{en_e}\nabla(n_e k T_e)] &= \nabla\left[\tfrac{k\sigma}{en_e\nabla(n_e T_e)}\right] \\
&= \nabla \cdot \left[\tfrac{k\sigma T_e}{e}\nabla(\ln n_e) + \tfrac{k\sigma}{e}\nabla T_e\right] \\
&= \tfrac{k}{e}[(\sigma\nabla T_e \cdot \nabla(\ln n_e) + T_e\nabla\sigma \cdot \nabla(\ln n_e) + \\
&\quad \sigma T_e\nabla^2(\ln n_e) + \nabla\sigma \cdot \nabla T_e + \sigma\nabla^2 T_e]
\end{aligned} \tag{B.8}$$

From the results (B.7) and (B.8), we can obtain a generalized Poisson's equation of the electric potential as follows

$$\begin{aligned}
\nabla \cdot (\sigma\nabla\phi) = \; & \tfrac{k}{e}[\sigma\nabla^2 T_e + \sigma T_e\nabla^2(\ln n_e) + \sigma\nabla(\ln n_e) \cdot \nabla T_e \\
& + T_e\nabla\sigma \cdot \nabla(\ln n_e) + \nabla\sigma \cdot \nabla T_e] \\
& - \tfrac{\partial\sigma}{\partial z} V_\phi B_r - \sigma(V_\phi \tfrac{\partial B_r}{\partial z} + B_r \tfrac{\partial V_\phi}{\partial z})
\end{aligned} \tag{B.9}$$

BIBLIOGRAPHY

[1] Cai, C., *Theoretical And Numerical Studies of Plume Flows in Vacuum Chambers*, Ph.D. Thesis, Dept. of Aerospace Engineering, University of Michigan, Ann Arbor, 2005.

[2] Kim, V., Kozubsky, K. N., and Murashko, V. M., "History of the Hall Thrusters Development in USSR," IEPC Paper 2007-142, Sep. 2007.

[3] Koo, J. W., *Hybrid PIC-MCC Computational Modeling of Hall Thrusters*, Ph.D. Thesis, Dept. of Aerospace Engineering, University of Michigan, Ann Arbor, 2005.

[4] Oh, D. Y., Hastings, D. E., Marrese, C. M., Haas, J. M., and Gallimore, A. D., "Modeling of Stationary Plasma Thruster-100 Thruster Plumes and Implications for Satellite Design," *Journal of Propulsion and Power*, Vol. 15, No. 2, 1999, pp. 345–357.

[5] Domonkos, M. T., Marrese, C. M., Haas, J. M., and Gallimore, A. D., "Very Near-Field Plume Investigations of the D55," AIAA Paper 1997-3062, July 1997.

[6] Choueiri, E. Y., "A Critical Histroy of Electric Propulsion: Teh First 50 Years(1906-1956)," *Journal of Propulsion and Power*, Vol. 20, No. 2, 2004, pp. 193–203.

[7] Dyson, F., "Disturbing the Universe," *Proceedings of the Royal Society*, Vol. 250, 1976, pp. 411–425.

[8] Tsien, H., S., "Takeoff from Satellite Orbit," *Journal of the American Rocket Society*, Vol. 23, 1953, pp. 233–236.

[9] Myers, R., "Overview of Electric Propulsion Acitivities in Industry," AIAA Paper 2000-3147, July 1994.

[10] Jahn, R. G., *Physics of Electric Propulsion*, McGraw-Hill, New York, 1968.

[11] Zhurin, V. V., Kaufman, H. R., and Robinson, R. S., "Physics of Closed Drift Thrusters," *Plasma Sources Science and Technology*, Vol. 8, No. 1, 1999, pp. R1–R20.

[12] Choueiri, E. Y., "Fundamental Difference Between the Two Hall Thruster Variants," *Physics of Plasma*, Vol. 8, No. 11, 2001, pp. 5025–5033.

[13] Fruchtman, A., Fisch, N. J., and Raitses, Y., "Hall thruster with absorbing electrodes," AIAA paper 2000-3659, July 2000.

[14] Ahedo, E., Martínez-Cerezo, P., and Martínez-Sánchez, M., "One-dimensional Model of the Plasma Flow in a Hall Thruster," *Physics of Plasmas*, Vol. 8, No. 6, 2001, pp. 3058–3068.

[15] Keidar, M. and Beilis, I. I., "Electron Transport Phenomena in Plasma Devices With ExB Drift," *IEEE Transaction on Plasma Science*, Vol. 34, No. 3, 2006, pp. 804–814.

[16] Fife, J. M., , and Martínez-Sánchez, M., "Two-dimensional hybrid particle in cell modeling of Hall thrusters," IEPC paper 1995-240, 1995.

[17] Szabo Jr., J. J., *Fully Kinetic Modeling of a Hall Thruster*, Ph.D. Thesis, Department of Aeronautics and Astronautics, Massachusetts Institute of Technology, Cambridge, MA, 2001.

[18] Keidar, M. and Boyd, I. D., "Effect of a Magnetic Field on the Plasma Plume from Hall Thrusters," *Journal of Applied Physics*, Vol. 86, No. 9, 1999, pp. 4786–4791.

[19] Boyd, I. D. and Yim, J. T., "Modeling of the Near Field Plume of a Hall Thruster," *Journal of Applied Physics*, Vol. 95, No. 9, 2004, pp. 4575–4584.

[20] Roy, R. S., *Numerical Simulation of Ion Thruster Plume Backflow for Spacecraft Contamination Assessment*, Ph.D. Thesis, Massachusetts Institute of Technology, 1995.

[21] Taccogna, F., Longo, S., and Capitelli, M., "Very-Near-Field Plume Simulation of a Stationary Plasma Thruster," *The European Physical Journal Applied Physics*, Vol. 28, No. 1, 2004, pp. 113–122.

[22] Cheng, S., Santi, M., Celik, M., Martínez-Sánchez, M., and Peraire, J., "Hybrid PIC-DSMC simulation of a Hall thruster plume on unstructured grids," *Computer Physics Communications*, Vol. 164, 2004, pp. 73–79.

[23] Alder, B. J. and Wainwright, T. E., "Phase Transition for a Hard Sphere System," *Jorunal of Chemical Physics*, Vol. 27, 1957, pp. 1208–1209.

[24] Alder, B. J. and Wainwright, T. E., "Studies in Molecular Dynamics. I. General Method," *Jorunal of Chemical Physics*, Vol. 31, 1959, pp. 459–466.

[25] Halie, J. M., *Molecular Dynamics Simulation: Elementary Methods*, Wiley Interscience, New York, 1993.

[26] Bird, G. A., *Molecular Gas Dynamics and the Direct Simulation of Gas Flows*, Oxford University Press, New York, 1994.

[27] Bird, G. A., "Approach to translational equilbrium in a rigid sphere gas," *Physics of Fluids*, Vol. 6, No. 10, 1963, pp. 1518–1519.

[28] Bird, G. A., "Monte Carlo Simulation in an Engineering Context," *Progress in Astronautics and Aeronautics*, 1998, pp. 239–255.

[29] Bird, G. A., "Fourty Years of DSMC," *Rarefied Gas Dynamics: 22nd International Symposium*, edited by T. J. Bartel and M. A. Gallis, 2001, pp. 372–380.

[30] Muntz, E. P., "Rarefied Gas Dynamics," *Annual Review of Fluid Mechanics*, Vol. 21, 1989, pp. 387–417.

[31] Oran, E. S., Oh, C. K., and Cybyk, B. Z., "Direct Simulation Monte Carlo: Recent Advances and Applications," *Annual Review of Fluid Mechanics*, Vol. 30, 1998, pp. 403–441.

[32] Ivanov, M. S. and Gimelshein, S. F., "Computational Hypersonic Rarefied Flows," *Annual Review of Fluid Mechanics*, Vol. 30, 1998, pp. 469–505.

[33] Bird, G. A., "Direct Simulation and the Boltzmann Equation," *Physics of Fluids*, Vol. 13, No. 11, 1970, pp. 2676–2681.

[34] Bird, G. A., "Monte-Carlo Simulation in an Engineering Context," *Proceedings of the 12th International Symposium on Rarefied Gas Dynamics, Charlottesville, Virginia*, edited by S. S. Fisher, 1981, pp. 239–255.

[35] Birdsall, C. K. and Langdon, A. B., *Plasma Physics Via Computer Simulation*, Adam Hilger, 1991.

[36] Roy, R. S., Hastings, D. E., and Taylor, S., "Three-Dimensional Plasma Particle-In-Cell Calculations of Ion Thruster Backflow Contamination," *Jorunal of Computational Physics*, Vol. 128, No. 1, 1996, pp. 6–18.

[37] VanGilder, D. B., *Numerical Simulation of The Plume of Electric Propulsion Thrusters*, Ph.D. Thesis, Cornell University, 2000.

[38] Braginsky, S. I., *Reviews of the Plasma Physics Vol. 1*, edited by Leontovich, M. A.,, Consultants Bureau, New York, 1965.

[39] Mitcher, M. and Kruger, C. H., *Partially Ionized Gases*, Wiley, 1973.

[40] Cohen-Zur, A. and Fruchtman, A., "Plume Divergence in the Hall Thruster Due to Pressure," IEPC Paper 2007-234, Sep. 2007.

[41] Vichnevetsky, R., *Computer Methods for Partial Differenctial Equations*, Prentice-Hall, 1981.

[42] Press, W. H., Vetterling, S. A., Flannery, W. T., and Flannery, B. P., *Numerical Recipes in C*, Cambridge University Press, New York, 1994.

[43] Price, H. S., Varga, R. S., and Fitzgerald, R. M., "Recent numerical experiments comparing successive overrelaxation iterative methods with implicit alternative direction iterative methods," 1961.

[44] Peaceman, D. W. and Rachford Jr., H. H., "The numerical solution of parabolic and elliptic differential equations," *Journal of the Society for Industrial and Applied Mathematics*, Vol. 3, No. 1, 1955, pp. 28–41.

[45] Chen, J., Wang, Z., and Chen, Y., "Higher-order alternative direction implicit FDTD method," *Electronics Letters*, Vol. 38, No. 22, 2002, pp. 1321–1322.

[46] Hammel, J. R., *Development of An Unstructured 3-D Direct Simulation Monte Carlo/Particle-In-Cell Code and the Simulation of Microthruster Flows*, M. S. Dissertation, Mechanical Engineering Department, Worcester Polytechnic Institute, Worcester, MA, 2002.

[47] Ruyten, W. M., "Density-Conserving Shape Factors for Particle Simulations in Cylindrical and Spherical Coordinates," *Journal of Computational Physics*, Vol. 105, No. 2, 1993, pp. 224–232.

[48] Dalgarno, A., McDowell, M. R. C., and Williams, A., "The Mobilities of Ions in Unlike Gases," *Philosophical Transactions of the Royal Society of London. Series A, Mathematical and Physical Sciences*, Vol. 250, No. 982, 1958, pp. 411–425.

[49] Pullins, S. H., Chiu, Y., Levandier, D. J., and Dresseler, R. A., "Ion dynamics in Hall effect and ion thrusters - Xe(+) + Xe symmetric charge transfer," AIAA Paper 2000-0636, Jan. 2000.

[50] Miller, S., Levandier, D. J., and Chiu, Y. Dresseler, R. A., "Xenon Charge Exchange Cross Sections for Electrostatic Thruster Models," *Journal of Applied Physics*, Vol. 19, No. 3, 2002, pp. 984–991.

[51] Boyd, I. D., "Conservative Species Weighting Scheme for the Direct Simulation Monte Calo Method," *Journal of Thermophysics and Heat Transfer*, Vol. 10, No. 4, 1996, pp. 579–585.

[52] Dietrich, S. and Boyd, I. D., "Scalar and Parallel Optimized Implementation of the Direct Simulation Monte Carlo Method," *Journal of Computational Physics*, Vol. 126, 1996, pp. 328–342.

[53] Choi, Y., Keidar, M., and Boyd, I., "Particle Simulation of Plume Flows From an Anode Layer Hall Thruster," AIAA Paper 2006-5026, July 2006.

[54] Koura, K. and Matsumoto, H., "Variable Soft Sphere Molecular Model for Air Species," *Physics of Fluids A*, Vol. 4, No. 5, May 1992, pp. 1083–1085.

[55] Boyd, I. D., "Rotational-Translational Energy Transfer in Rarefied Nonequilibrium Flows," *Physics of Fluids A*, Vol. 2, No. 3, 1990, pp. 447–452.

[56] Boyd, I. D., "Analysis of Rotational Nonequilibrium in Standing Shock Waves of Nitrogen," *AIAA Journal*, Vol. 28, No. 11, 1990, pp. 1997–1999.

[57] Vijayakumar, P., Sun, Q., and Boyd, I. D., "Detailed Models of Vibrational-Translational Energy Exchange for the Direct Simulation Monte Carlo Method," *Physics of Fluids*, Vol. 11, No. 8, 1999, pp. 2117–2126.

[58] Ahedo, E., Gallardo, J. M., and Martínez-Sánchez, M., "Model of the Radial Plasma-Wall Interaction on the Hall Thruster Discharge," *Physics of Plasmas*, Vol. 10, No. 8, 2003, pp. 3397–3409.

[59] Barral, S., Makowski, K., Peradzynski, Z., Gascon, N., and Dudeck, M., "Wall Material Effects in Stationary Plasma Thrusters. II. Near-Wall and In-Wall Conductivity," *Physics of Plasmas*, Vol. 10, No. 10, 2003, pp. 4137–4152.

[60] Keidar, M., Boyd, I. D., and Beilis, I. I., "Plasma Flow and Plasma-Wall Transition in Hall Thruster Channel," *Physics of Plasmas*, Vol. 8, No. 12, 2001, pp. 5315–5322.

[61] Keidar, M., Gallimore, A. D., Raitses, Y., and Boyd, I. D., "On the Potential Distribution in Hall Thrusters," *Applied Physics Letters*, Vol. 85, No. 13, 2004, pp. 2481–2483.

[62] Roy, S. and Pandey, B. P., "Development of a Finite Element-Based Hall-Thruster Model," *Journal of Propulsion and Power*, Vol. 19, No. 5, 2003, pp. 964–971.

[63] Yim, J. T., *Computational Modeling of Hall Thruster Channel Wall Erosion*, Ph.D. Thesis, Dept. of Aerospace Engineering, University of Michigan, Ann Arbor, 2008.

[64] LeVeque, R. J., "Wave Propagation Algorithms for Hyperbolic Systems," *Journal of Computational Physics*, Vol. 131, No. 2, 1997, pp. 327–353.

[65] Ahedo, E., Gallardo, J. M., and Martínez-Sánchez, M., "Model of the Plasma Discharge in a Hall Thruster with Heat Conduction," *Physics of Plasmas*, Vol. 9, No. 9, 2002, pp. 4061–4070.

[66] Manzella, D. H., "Hall Thruster Ion Beam Characterization," AIAA paper 1995-2927, July 1995.

[67] Ahedo, E. and Martínez-Sánchez, M., "Steady and Linearly Unstaedy Analysis of a Hall Thruster with an Internal Sonic Point," AIAA paper 2000-3655, July 2000.

[68] Sorokin, A. A., Shmaenok, L. A., Bobachev, S. V., Möbus, B., Richter, M., and Ulm, G., "Measurements of Electron-Impact Ionization Cross Sections of Argon, Krypton, and Xenon by Comparison with Photoionization," *Physical Review A*, Vol. 61, No. 2, 2000, pp. 022723.

[69] Nicholson, D. R., *Introduction to Plasma Theory*, John Wiley & Sons, Inc., 1983.

[70] Boeuf, J. P. and Garrigues, L., "Low Frequency Oscillations In a Stationary Plasma Thruster," *Journal of Applied Physics*, Vol. 84, No. 7, 1998, pp. 3541–3544.

[71] Seiler, H., "Secondary Electron Emission in the Scanning Electron Microscope," *Journal of Applied Physics*, Vol. 54, No. 11, 1983, pp. R1–R18.

[72] Hobbs, G. D. and Wesson, J. A., "Heat Flow Through a Langmuir Sheath in the Presence of Electron Emission," *Plasma Physics*, Vol. 9, 1967, pp. 85–87.

[73] Bohm, D., *The Characteristics of Electical Discharges in Magnetic Field*, edited by Guthry, A. and Wakerling, R. K., McGraw-Hill, New York, 1983.

[74] Beilis, I. I. and Keidar, M., "Sheath and presheath structure in the plasma-wall transition layer in an oblique magnetic field," *Physics of Plasmas*, Vol. 5, No. 5, 1998, pp. 1545–1553.

[75] Riemann, K. U., "The Bohm Criterion and Sheath Formation," *Journal of Physics D: Applied Physics*, Vol. 24, No. 4, 1991, pp. 493–518.

[76] Godyak, V. A. and Sternberg, N., "Smooth Plasma-Sheath Transition in a Hydrodynamic Model," *IEEE Transsactions on Plasma Science*, Vol. 18, No. 1, 1990, pp. 159–168.

[77] Godyak, V. A., "Modified Bohm Criterion for a Collisional Plasma," *Physics Letters*, Vol. 89, No. 2, 1982, pp. 80–81.

[78] Roe, P. L., "Approximate Riemann Solvers, Parameter Vectors, and Difference Schemes," *Journal of Computational Physics*, Vol. 135, No. 2, 1997, pp. 250–258.

[79] Sankovic, J. M., Haag, T. W., and Manzella, D. H., "Operating Characteristics of the Russian D-55 Thruster with Anode Layer," AIAA paper 1994-3011, June 1994.

[80] Yim, J., T., Private communication.

[81] Keidar, M., Choi, Y., and Boyd, I. D., "Modeling a Two-Stage High-Power Anode Layer Thruster and its Plume," *Journal of Propulsion and Power*, Vol. 23, No. 2, 2007, pp. 502–506.

[82] Boyd, I. D., "Computation of the Plume of an Anode-Layer Hall Thruster," *Journal of Propulsion and Power*, Vol. 16, No. 5, 2000, pp. 902–909.

[83] Keefer, D., Wright, N., Hornkohl, J. O., and Bangasser, J., "Multiplexed LIF and Langmuir Probe Diagnostic Measurements in the TAL D-55 Thruster," AIAA paper 1999-2425, July 1999.

[84] Keidar, M., Boyd, I. D., and Beilis, I. I., "Modeling of a High-Power Thruster with Anode Layer," *Physics of Plasmas*, Vol. 11, No. 4, 2004, pp. 1715–1722.

[85] Child, C., D., "Discharge From Hot Cao," *Physical Review*, Vol. 32, No. 5, 1911, pp. 492–511.

[86] Langmuir, I., "The Effect of Space Charge and Residual Gases on Thermionic Currents in High Vacuum," *Physical Review*, Vol. 2, No. 6, 1913, pp. 450–486.

[87] Tajmar, M., Gonźalez, J., Saccoccia, G., Noci, G., and Laakso, H., "Plasma Diagnostics and Simulation for the SMART-1 Mission," *Planetary and Space Science*, Vol. 50, 2002, pp. 1355–1360.

[88] Garner, C. E., Brophy, J. R., Polk, J. E., Semenkin, S., Garkusha, V., Tverdokhlebov, S., and Marrese, C., "Experimental Evaluation of the Russian Anode Layer Thruster," 3rd russian-german conference of electric propulsion engines and their techniacal applications, July 1994.

[89] Gulczinski, F. S., Gallimore, A. D., Carlson, D. O., and Gilchrist, B. E., "Impact of Anode Layer Thruster Plumes on Satellite Communications," AIAA paper 1997-3067, 1997.

[90] Semenkin, A., Kochergin, A., Garkusha, V., Chislov, G., Rusakov, A., Tverdoklebov, S., and Sota, C., "RHETT/EPDM Flight Anode Layer Thruster Development," IEPC Paper 1997-106, Aug. 1997.

[91] Zakharenkov, L., Semenkin, A., V., and Lebedev, Y., V., "Measurement Features and Results of TAL D55 Plume," IEPC paper 2005-184, Oct. 2005.

[92] Domonkos, M., T., Gallimore, A., D., and Williams Jr., G., J., "Low-Current Hollow Cathode Evaluation," AIAA paper 1999-2575, July 1999.

[93] *HyperMesh ver. 6.0*, Altair Engineering Inc, 2003.

[94] Karypis, G. and Kumar, V., *METIS: A Software Package for Partitioning Unstructured Graphs, Partitioning Meshes, and Computing Fill-Reducing Orderings of Sparse Matrices, version 4.0*.

[95] Li, S., "An HLLC Riemann Solver for Magneto-hydrodynamics," *Journal of Comutaitional Physics*, Vol. 203, No. 1, 2005, pp. 344–357.

[96] Collella, P., Dorr, M. R., and Wake, D. D., "A conservative Finite Difference Method for the Numerical Solution of Plasma Fluid Equations," *Journal of Comutaitional Physics*, Vol. 149, No. 1, 1999, pp. 168–193.